Magnetic resonance imaging of the liver. T1 dynamics: confounders and modelling



Ferenc Emil Mózes

St. Cross College

University of Oxford

A thesis submitted for the degree of

Doctor of Philosophy

Trinity 2018

"Every biopsy is a failed imaging experiment"

Vikas Gulani

Magnetic resonance imaging of the liver. T_1 dynamics: confounders and modelling

Ferenc Emil Mózes, St. Cross College, Trinity Term 2018

A thesis submitted for the degree of Doctor of Philosophy

Abstract

Non-alcoholic fatty liver disease (NAFLD) is becoming increasingly prevalent in the world population. The current gold standard for diagnosing NAFLD, however, is still the liver needle biopsy, the evaluation of which can be subjective, lacks good reproducibility, and suffers from sampling bias. Multiparametric MRI exams comprising measurements of proton density fat fraction, hepatic iron concentration and liver T_1 values, with iron-corrected T_1 measurements correlating well with liver fibrosis and inflammation, have been suggested as a good non-invasive candidate to diagnose NAFLD. However, T_1 values and T_1 measurement methods are affected by more than just iron. The work presented in this thesis focussed on characterising the complex dependence of T_1 values on hepatic lipid concentration when using the MOLLI methods. Dependent on field strength, magnetic field inhomogeneities, and sequence parameters (such as echo time and repetition time), the deleterious effects of fat can result in an artificial increase or decrease of measured liver T_1s. An algorithm capable of reversing the effects of fat and frequency offsets was developed and tested in phantoms and in prospectively recruited participants by comparing the outcome of the algorithm to liver water T_1 values measured using MR spectroscopy.

Finally, two other influencing factors of liver T_1 were also studied: liver glycogen concentration and body hydration status, both of which are subject to significant diurnal variation and their T_1 effect has been shown earlier. A small study involving healthy volunteers undergoing metabolic interventions was conducted to determine the dependence of liver T_1 values on liver glycogen concentration and hydration status.

Acknowledgements

This thesis would have never been born without the generous support of my supervisors, Prof Matthew Robson and Dr Elizabeth Tunnicliffe. I thank Matt for never turning me away when I knocked on his door (even on the direst days of grant writing) and Liz for always finding the time for a quick (but mostly not so quick) chat despite her very tight schedule.

Dr Ladislav Valkovič and Dr Aaron Hess were of great help whenever I needed practical advice on spectroscopy or imaging sequence minutiae.

I would like to express my gratitude to Hunor, Miklós, Zsófia, Belinda, Edit and Arjan for being supportive whenever I felt overwhelmed by work. Their words of encouragement renewed my faith in my project on numerous occasions.

Special thanks go for Prof Piroska Haller for encouraging me to apply for a DPhil project and for being a model of a humble and rigorous scientist.

Last but not least, I am grateful for the endless support of my ever-loving Mother and late Father.

Publications

JOURNAL ARTICLES

[1] **Mozes, Ferenc E**, Elizabeth M Tunnicliffe, Ahmad Moolla, Thomas Marjot, Christina K Levick, Michael Pavlides, and Matthew D Robson. Mapping tissue water T_1 in the liver using the MOLLI T_1 method in the presence of fat, iron and B_0 inhomogeneity. *NMR in Biomedicine*, 32(2):e4030, Feb 2019.

[2] **Mozes, Ferenc E**, Elizabeth M. Tunnicliffe, Michael Pavlides, and Matthew D. Robson. Influence of fat on liver T_1 measurements using modified Look-Locker inversion recovery (MOLLI) methods at 3 T. *Journal of Magnetic Resonance Imaging*, 44(1):105–111, Jul 2016.

CONFERENCE ABSTRACTS

[1] Garrison, Liam D and Levick, Christina and Pavlides, Michael and Marjot, Tom and **Mozes, Ferenc** and Hodson, Leanne and Neubauer, Stefan and Robson, Matthew and Rodgers, Christopher T. Water-Only Look-Locker Inversion recovery (WOLLI) T_1 mapping. In *Proc. Intl. Soc. Mag. Reson. Med. 25*, page 0435, 2017.

[2] **Mozes, Ferenc E** and Tunnicliffe, Elizabeth M and Marjot, Thomas and Levick, Christina K and Pavlides, Michael and Robson, Matthew D. Determining the T_1 of the water in the liver by modelling the effects of fat, iron and off-resonance frequencies on MOLLI T_1 measurements. In *Proc. Intl. Soc. Mag. Reson. Med. 25*, page 367, 2017.

[3] **Mozes, Ferenc E** and Tunnicliffe, Elizabeth M and Pavlides, Michael and Robson, Matthew D. Is Fat a Confounding Factor for MOLLI T_1 Measurements in the Liver at 3 Tesla? In *Proc. Intl. Soc. Mag. Reson. Med. 24*, page 3839, 2016.

[4] **Mozes, Ferenc E** and Tunnicliffe, Elizabeth M and Pavlides, Michael and Robson, Matthew D. The influence of glycogen on shortened modified Look-Locker inversion recovery (shMOLLI) T_1 maps of the liver. In *Proc. Intl. Soc. Mag. Reson. Med. 26*, page 2613, 2018.

[5] **Mozes, Ferenc E** and Tunnicliffe, Elizabeth M and Robson, Matthew D. Correction of the effects of asymmetric bSSFP echo on (sh)MOLLI T_1 maps of water-fat mixtures at 3 T an its implication on fatty liver imaging. In *Proceedings of the ISMRM Workshop on Quantitative Body Imaging*, 2018.

[6] **Mozes, Ferenc E** and Tunnicliffe, Elizabeth M and Valkovič, Ladislav and Pavlides, Michael and Robson, Matthew D. Glycogen and body hydration status are confounders of liver shMOLLI T_1 measurements. In *Proc. British Chapter Intl. Soc. Mag. Reson. Med.*, 2018.

PATENT APPLICATION

[1] Matthew D Robson and **Mozes, Ferenc E**. Correction method for magnetic resonance T_1-mapping of visceral organs in the presence of elevated iron and elevated fat levels, and in the presence of off-resonance frequencies, Patent application, WO2018083504A1, 2018.

Contents

Contents vi

List of Figures xi

List of Tables xiv

List of Abbreviations xv

1 Introduction 1

1.1 Motivation 1

1.2 Objectives 2

1.3 Outline of chapters 3

2 Magnetic resonance physics 5

2.1 Nuclear spins and magnetic moments 5

2.1.1 The classical mechanics model 6

2.1.2 Excitation and relaxation 7

2.1.2.1 T_1 relaxation 10

2.1.2.2 T_2 and T_2^* relaxation 12

2.2 Image formation 14

2.2.1 Slice selection 15

2.2.2 Frequency encoding 16

2.2.3 Phase encoding 18

2.2.4 k-space and image reconstruction 19

2.3 Pulse sequences 21

2.3.1 Spin echoes . . . 22

2.3.2 Stimulated echoes . . . 23

2.3.3 Fast imaging with balanced steady-state free precession . . . 24

2.3.4 MR spectroscopy using stimulated echoes . . . 27

2.4 Applications 29

2.4.1 Shortened modified Look-Locker inversion recovery T_1 mapping . . . 30

2.4.2 Fat-water separation, T_2^*, and B_0 mapping using gradient echoes . . . 32

2.5 Summary 34

3 Imaging the liver 35

3.1 Anatomy, physiology and pathology of the liver 35

3.1.1 Anatomy . . . 35

3.1.2 Physiology . . . 37

3.1.3 Diseases of the liver . . . 40

3.2 Imaging the liver 41

3.2.1 Ultrasound . . . 42

3.2.2 Transient elastography . . . 42

3.2.3 Computed tomography . . . 43

3.3 Quantitative characterisation of the liver using MR techniques 44

3.3.1 Magnetic resonance elastography . . . 44

3.3.2 Fat fraction measurements . . . 45

3.3.2.1 MRS PDFF . . . 45

3.3.2.2 MRI PDFF . . . 46

3.3.3 T_2 and T_2^* mapping . . . 47

3.3.4 T_1 mapping . . . 49

3.4 Summary 51

4 The influence of fat on liver MOLLI T_1 measurements 52

4.1 Introduction 52

4.2 Theory 53

4.3 Materials and Methods 56

4.3.1 Simulations 56

4.3.2 Phantom Scans 60

4.3.3 Patient Studies 61

4.4 Results 62

4.4.1 Simulation 62

4.4.2 Phantom Scans 65

4.4.3 Patient Studies 67

4.5 Discussion 69

4.6 Conclusions 70

5 Determining water shMOLLI T_1 in fatty livers 72

5.1 Introduction 72

5.2 Methods 73

5.2.1 Phantom experiments 74

5.2.1.1 Construction 74

5.2.1.2 Imaging 74

5.2.1.3 Spectroscopy 76

5.2.1.4 Simulation 77

5.2.1.5 Determining the water shMOLLI T_1 78

5.2.2 Patient study 79

5.2.2.1 Patient population 79

5.2.2.2 Imaging 79

5.2.2.3 The MOLLI water T_1 determination algorithm 81

5.2.3 Statistical analysis 86

5.3 Results 87

5.3.1 Phantom experiments 87

5.3.2 Patient studies 89

5.4 Discussion 96

5.5 Conclusion 100

6 Water-only shMOLLI T_1 is associated with fibrosis stage 101

6.1 Introduction 101

6.2 Methods 102

6.2.1 Participants . . . 102

6.2.2 MRI data acquisition . . . 102

6.2.3 Data analysis . . . 103

6.2.4 Statistical analysis . . . 103

6.3 Results 104

6.4 Discussion 106

6.5 Conclusions 109

7 The influence of liver glycogen concentration and body hydration status on liver T_1 measurements 111

7.1 Introduction 111

7.2 Methods 113

7.2.1 Phantom experiments . . . 113

7.2.2 Pilot human experiments . . . 114

7.2.3 Multi-participant study . . . 116

7.2.3.1 Protocol . . . 116

7.2.3.2 Data acquisition and analysis . . . 117

7.2.4 Statistical analysis . . . 119

7.3 Results 121

7.3.1 Phantom experiments . . . 121

7.3.2 Human experiments . . . 122

7.3.2.1 Pilot studies . . . 122

7.3.2.2 Multi-participant study . . . 123

7.4 Discussion 127

7.5 Conclusion 130

8 Summary and outlook 131

8.1 Conclusions 131

8.2 Outlook 134

Bibliography 138

List of Figures

2.1 Precessional motion of a spin 7

2.2 The effect of B_1 excitation in the laboratory frame of reference 9

2.3 The effect of B_1 excitation in the rotating frame of reference 10

2.4 A typical FID signal 11

2.5 Dependence of relaxation times on correlation time 12

2.6 Spectral density functions of different water pools 13

2.7 The principle of slice selection 16

2.8 Simple sequence diagram illustrating slice selection 16

2.9 The principle of frequency encoding 17

2.10 An example of phase encoding 18

2.11 An image space - k-space pair 21

2.12 k-space traversal trajectories 21

2.13 One TR interval of the spin echo pulse sequence 22

2.14 The stimulated echo pulse sequence 24

2.15 The bSSFP sequence 26

2.16 Frequency dependence of the bSSFP signal 27

2.17 The STEAM spectroscopic pulse sequence 29

2.18 Typical proton spectrum of a fatty liver 30

2.19 The shMOLLI pulse sequence diagram 31

3.1 Couinaud segments of the liver 36

3.2 The hepatic lobule 37

3.3 Structural and functional organisational units of the liver parenchyma 38

4.1 Frequency dependence of the bSSFP signal 54
4.2 Phase relationship between fat and water 55
4.3 (sh)MOLLI T_1 dependence on fat fraction 57
4.4 An abdominal off-resonance frequency map 59
4.5 Dependence of (sh)MOLLI T_1 on fat fraction and echo time 64
4.6 Examples of the fat fraction dependence of (sh)MOLLI T_1 at different echo times 64
4.7 Fat fraction dependence of (sh)MOLLI T_1 with variable frequency offsets 65
4.8 Frequency dependence of (sh)MOLLI T_1 66
4.9 Inversion recovery signal from a margarine phantom 66
4.10 TR-dependence of (sh)MOLLI T_1 67
4.11 Patient (sh)MOLLI T_1 values 68

5.1 Schematic of the liver model 82
5.2 Block diagram of the water determination algorithm 86
5.3 Phantom forward simulation 88
5.4 Modified Bland-Altman plot of phantom results 88
5.5 Patient forward simulation and correction 92
5.6 Modified Bland-Altman plots of patient results 92
5.7 Patient correction with MT 93
5.8 Modified Bland-Altman plots of patient results considering MT 93
5.9 Liver water T_1 map determination results and variants 95

6.1 Box plots of measured and corrected T_1 values 105
6.2 Relationship of T_1 and PDFF 108
6.3 Distribution of inflammation scores within Ishak stage groups 108

7.1 Glyocgen metabolism 112
7.2 Timing of study procedures 117

7.3 Typical placement of ROIs 120

7.4 Glycogen phantom relaxation rates 121

7.5 Glycogen pilot study results 122

7.6 Hydration pilot study results 123

7.7 Comparison of different metabolic states 125

7.8 Lagged plots of residuals 126

8.1 T_1 influencing factors 135

List of Tables

4.1 T_1 measured with 5-point MOLLI and SE-IR 65

5.1 Simulation parameters for the liver model at 3 Tesla 83

5.2 Additional simulation parameters for the liver model at 3 Tesla when considering exchange effects 84

5.3 Fat peak parameters used in the Bloch simulation of the shMOLLI sequence 89

5.4 Baseline parameter values for fat-water phantoms 90

5.5 Linear regression results 94

6.1 Participants' baseline characteristics 106

6.2 Correlations between T_1 and Ishak fibrosis stages 107

7.1 Inclusion and exclusion criteria for the glycogen-hydration study 118

7.2 Glycogen relaxivities in phantoms 121

7.3 Linear regression outcomes 127

List of Abbreviations

ALD	alcohol-related liver disease
Ao	aorta
AUROC	area under the receiver operator curve
bSSFP	balanced steady-state free precession
BMI	body-mass index
CM	classical mechanics
CT	computed tomography
TE	echo time
ECG	electrocardiogram
v_E	extracellular fluid volume fraction
FOV	field of view
FA	flip angle
FID	free induction decay
GRAPPA	generalised autocalibrating partial parallel acquisition
GRE	gradient-recalled echo
HIC	hepatic iron concentration

HLC	hepatic lipid concentration
HVPG	hepatic venous pressure gradient
HCC	hepatocellular carcinoma
IVC	inferior vena cava
TI	inversion time
IDEAL	iterative decomposition of water and fat with asymmetric echo times and least-squares estimation
LMM	linear mixed model
LISA	linearly increasing start-up angle
LS	liver stiffness
MRE	magnetic resonance elastography
MRI	magnetic resonance imaging
MRS	magnetic resonance spectroscopy
MT	magnetisation transfer
MOLLI	modified Look-Locker inversion recovery
MCSE	multiple contrast spin echo
NASH CRN	NASH Clinical Research Network
NAFLD	non-alcoholic fatty liver disease
NASH	non-alcoholic steatohepatitis
NMR	nuclear magnetic resonance
PRESS	point-resolved spectroscopy

PBC	primary biliary cholangitis
PDFF	proton density fat fraction
RF	radiofrequency
TR	repetition time
SASHA	saturation recovery single shot acquisition
shMOLLI	shortened modified Look-Locker inversion recovery
SNR	signal-to-noise ratio
SVS	single-voxel spectroscopy
SE-IR	spin echo inversion recovery
SE	spin echo
SPGR	spoiled gradient echo
SSFP	steady-state free precession
SAF	steatosis, activity and fibrosis score
STEAM	stimulated echo acquisition mode
TSE-IR	turbo spin echo inversion recovery
2DFT	two-dimensional Fourier-transform
US	ultrasound
VIBE	volumetric interpolated breath-hold examination

1

Introduction

1.1 MOTIVATION

Advances in the understanding of liver physiology as well as changing diets and lifestyle in the past 40 years have allowed the recognition of liver diseases of the non-alcoholic type (non-alcoholic steatohepatitis (NASH) and non-alcoholic fatty liver disease (NAFLD)) [1, 2]. NAFLD can be asymptomatic for long periods of time and many cases are diagnosed incidentally by abnormal liver function test results or confirmation of steatosis during a routine abdominal ultrasound examination [3]. Hepatic steatosis can evolve into NASH, associated with fibrosis and cirrhosis. In some cases cirrhosis may further develop into hepatocellular carcinoma (HCC) [4]. There are studies suggesting that regression of fibrosis is also possible [5, 6], but sampling error associated with the gold standard biopsy makes it difficult to accurately characterise fibrosis progression and regression [3]. Some of the risk factors of developing NAFLD include obesity, diabetes and cardiovascular disease, therefore NAFLD is strongly linked to metabolic syndrome [3].

The prevalence of NAFLD has increased in recent years [7–9], and not every case of NAFLD can be diagnosed with needle biopsy or it is not feasible to perform needle biopsies during treatment and follow-up. It is, therefore, crucial to find other, non-invasive ways of diagnosing NAFLD, and, perhaps more importantly, to differentiate between NAFLD and NASH. While a number of blood tests and imaging-based methods have been developed recently, none have replaced liver needle biopsy either due to limited availability of resources (e.g. lack of equipment) or low diagnostic performance. As shortened modified Look-Locker inversion recovery (shMOLLI) T_1 measurements have gained popularity in the cardiac MRI community [10, 11] and were shown to correlate well with liver fibrosis and inflammation [12, 13], it is a promising new quantitative MRI biomarker-candidate.

1.2 OBJECTIVES

The purpose of the work undertaken for this thesis was to facilitate the wider acceptance and understanding of (sh)MOLLI T_1 measurements in the liver. For this, the specific objectives were:

- To explore and characterise the effects of hepatic lipid concentration and off-resonance frequency on (sh)MOLLI T_1 measurements using simulation, phantoms and existing patient data.
- To describe and validate a post-processing method for reversing the deleterious effects of hepatic lipid concentration and frequency offsets in both phantoms and humans by extending an already existing biophysical model of the liver [14].
- To retrospectively apply the water shMOLLI T_1 determination algorithm on a sub-cohort of a clinical study, aimed to assess the correlation of water shMOLLI T_1 values

with Ishak fibrosis stage.

- To characterise the effect of liver glycogen concentration and body hydration status on liver shMOLLI T_1 values. The motivation for this is to understand the relatively large variability of liver shMOLLI T_1 values in healthy volunteers, and, by extension, in patients too with the aim of reducing the large normal range, ultimately improving the diagnostic performance of shMOLLI T_1.

1.3 OUTLINE OF CHAPTERS

The remainder of the thesis is organised as follows:

Chapter 2 presents the fundamental notions of magnetic resonance physics, from the early work of Felix Bloch and Erwin Hahn through intrinsic MR properties of tissues and MRI contrast mechanisms to more advanced pulse sequences, both imaging and spectroscopic.

Chapter 3 contains a brief description of liver physiology and imaging techniques used to evaluate liver pathology. The advantages and disadvantages of ultrasound, computed tomography, and transient elastography are discussed along with existing magnetic resonance imaging- and spectroscopy-related quantitative techniques, including magnetic resonance elastography (MRE).

The aim of the study presented in chapter 4 is to characterise the effect of fat and off-resonance frequencies on MOLLI T_1 mapping sequences. While it is known that T_1 in the liver is influenced by a number of factors (e.g. hepatic iron concentration (HIC) [15, 16], inflammation and fibrosis [12, 13]), the effect of hepatic lipid concentration (HLC) is under-reported, although steatosis is a hallmark of liver disease. Due to the growing popularity of modified Look-Locker T_1 mapping methods, it is important to explore the behaviour of

the sequence in cases of imaging fatty livers. The results of this chapter were published as a paper [17].

A method for removing the effects of fat and off-resonance frequency from T_1 measurements performed with MOLLI T_1 mapping methods is presented in chapter 5. As chapter 4 describes the behaviour of the MOLLI sequence in cases when the imaged tissue contains both water and fat at the subvoxel level, it is necessary to reverse the deleterious effects of fat and the dependence on frequency offsets to be able to explore disease-related changes in liver T_1 values. This work has been accepted for publication in NMR in Biomedicine.

Chapter 6 presents an application of the water-only (sh)MOLLI T_1 determination algorithm in a cohort of patients with biopsy-confirmed fibrosis and proton density fat fraction (PDFF) larger than 5%. A modest increase in correlation between T_1 values and fibrosis scores was observed after the correction.

In contrast with the previous chapters exploring factors influencing the MOLLI sequence that are due to the properties of the balanced steady-state free precession (bSSFP) sequence, chapter 7 explores the influence of glycogen on liver T_1 values as a relaxation agent. Additionally, the variation of liver T_1 with changes in body hydration status was also assessed in this chapter through a study involving exercise and dietary interventions on a small cohort of 8 healthy volunteers.

Chapter 8 concludes the thesis and summarises already known and newly characterised confounding factors of modified Look-Locker inversion recovery (MOLLI) T_1 measurements of the liver. Since the liver is such a complex organ and performs so many metabolic functions, there may very well be many other factors influencing T_1 measurements. This chapter attempts to place all known and potential confounding factors in a global framework, predicting the time frame over which each exerts its effect and the amount of change to be expected as the result of each factor.

2

Magnetic resonance physics

The phenomenon of nuclear magnetic resonance (NMR) was first described separately by Felix Bloch [18] and Edward Purcell in 1946 [19]. In 1952, they were awarded the Nobel prize in physics for their achievement. This chapter aims to briefly describe the classical mechanics (CM) approach to modelling NMR phenomena, as well as details of image formation and basic pulse sequences.

2.1 NUCLEAR SPINS AND MAGNETIC MOMENTS

Atomic nuclei consist of nucleons called neutrons and protons. The fundamental property of these nucleons that is directly linked to the NMR signal is the spin. Every unpaired nucleon contributes to the overall spin of a nucleus by a spin of I = 1/2. Therefore, the nuclei to which NMR is sensitive are those having unpaired protons or unpaired neutrons or both [20]. Nuclei with both paired protons and paired neutrons are "NMR invisible". Magnetic resonance imaging (MRI) and spectroscopy (MRS) - both derived from NMR - are interested mostly in the ^{1}H nucleus, containing a single proton and being highly abundant

in the human body. However, any nucleus with an overall non-zero spin can be studied with NMR techniques. While the individual behaviour of protons is best described by quantum mechanics, the ensemble of protons can be comfortably characterised using CM.

2.1.1 *The classical mechanics model*

Similarly to a compass needle, that is forced to turn in the magnetic field of the Earth, a proton that is not aligned with an applied external magnetic field, will experience a torque. This torque will force the proton to perform a circular motion, called precession, around the axis of the magnetic field. Considering that the magnetic moment is directly proportional to the angular momentum via the quantum mechanical expression $\boldsymbol{\mu} = \gamma \boldsymbol{J}$, the rate of change in the angular momentum can be written as eq. 2.1, where θ is the angle between the magnetic moment and the magnetic field vectors.

$$\left|\frac{d\boldsymbol{J}}{dt}\right| = |\boldsymbol{\mu} \times \boldsymbol{B}| = |\gamma \boldsymbol{J} \times \boldsymbol{B}| = \gamma J B \sin\theta \tag{2.1}$$

Further, from the geometry depicted in fig. 2.1, results:

$$|d\boldsymbol{\mu}| = \mu \sin\theta d\varphi \tag{2.2}$$

From equations 2.1, 2.2, and $\mu = \gamma J$ we have $\gamma \mu B \sin\theta dt = \mu \sin\theta d\varphi$, from where it results:

$$\omega \equiv \left|\frac{d\varphi}{dt}\right| = \gamma B \tag{2.3}$$

Equation 2.3 is known as the Larmor equation and ω is the Larmor-frequency. The precessional motion of the net magnetisation in the absence of relaxation effects is described by a similar equation to eq. 2.1:

$$\left|\frac{d\boldsymbol{M}}{dt}\right| = \gamma \boldsymbol{M} \times \boldsymbol{B_0} \tag{2.4}$$

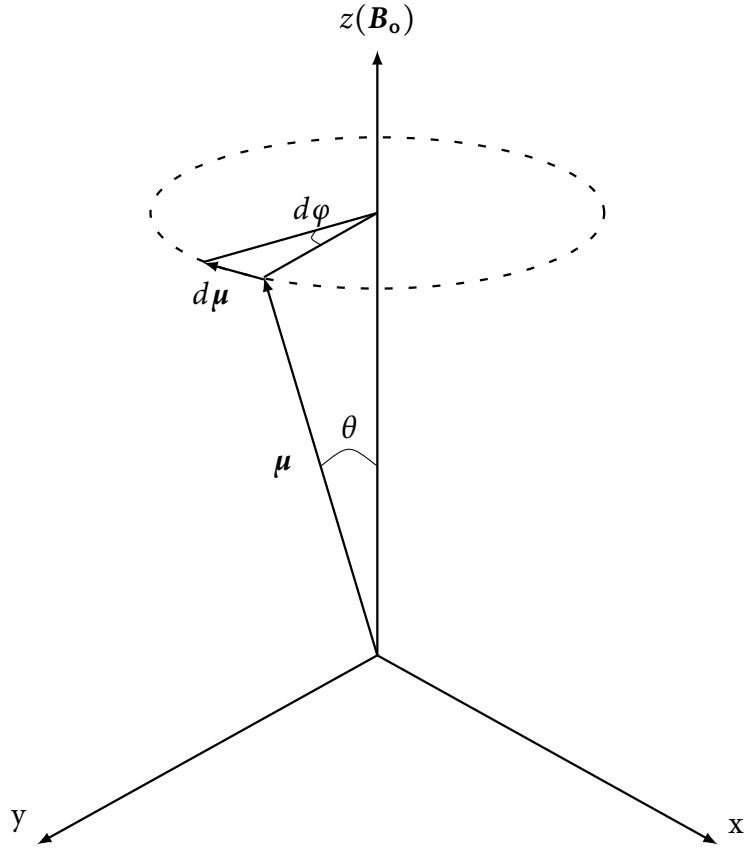

Figure 2.1: Precession of a spin around an external magnetic field ($\boldsymbol{B}_o$)

2.1.2 *Excitation and relaxation*

From a classical mechanics point of view it makes sense to consider an ensemble of spins instead of individual spins. For this, the concept of net magnetisation vector ($\boldsymbol{M}_o$) is used, defined as the sum of the magnetisations of individual spins. The net magnetisation is dependent on the difference between the number of spins in the up and down states, governed by the Boltzmann distribution. Equation 2.5 describes the ratio of spins in the up state ($N_\uparrow$) and spins in the down state ($N_\downarrow$). Here ΔE is the difference between the energy levels of the two spin states, k_B is the Boltzmann constant, and T is the absolute temperature

of the spin ensemble.

$$\frac{N_{\uparrow}}{N_{\downarrow}} = e^{-\frac{\Delta E}{k_B T}} = e^{-\frac{\hbar \gamma B_z}{k_B T}} \tag{2.5}$$

Equation 2.6 provides an approximation of the difference between spins in the up and down states (N_{total} denotes the total number of spins in the studies spin ensemble), from which results the equation for the net magnetisation M_0 (eq. 2.7).

$$\Delta N \approx \frac{N_{total} \hbar \gamma B_z}{2 k_B T} \tag{2.6}$$

$$M_0 = \frac{\Delta N \hbar \gamma}{2} = \frac{N_{total} \hbar^2 \gamma^2 B_z}{4 k_B T} \tag{2.7}$$

While the $\boldsymbol{M_0}$ net magnetisation is at thermal equilibrium in the external magnetic field $\boldsymbol{B_0}$, it cannot be measured by the receiver coils. To detect $\boldsymbol{M_0}$, a second magnetic field - $\boldsymbol{B_1}$ - generated by a radiofrequency (RF) pulse (also called an excitation pulse) oscillating at a frequency equal to the Larmor-frequency is used, which is orthogonal to $\boldsymbol{B_0}$. Such an RF pulse will tip $\boldsymbol{M_0}$ away from the direction of $\boldsymbol{B_0}$, thus creating an $\boldsymbol{M_{xy}}$ magnetisation component in the xy transverse plane. After the start of the RF pulse, the net magnetisation will precess around both $\boldsymbol{B_0}$ and $\boldsymbol{B_1}$. When the RF pulse is turned off, the magnetisation will spiral back to its thermal equilibrium, while individual spins are exchanging energy with each other and their environment. Figure 2.2 depicts excitation by $\boldsymbol{B_1}$ and the return of the net magnetisation to thermal equilibrium. So far, the motion of the net magnetisation vector was described in the stationary laboratory frame of reference. However, following the effects of the $\boldsymbol{B_1}$ field on the net magnetisation vector is easier in a so called rotating frame of reference. In this new frame of reference the transverse plane is rotating around the z axis, i.e. the axis of $\boldsymbol{B_0}$ at the Larmor frequency, such that precessional motion around the main magnetic field "vanishes" and $\boldsymbol{B_1}$ appears to be static. Figure 2.3 shows the concept of excitation in the rotating frame of reference.

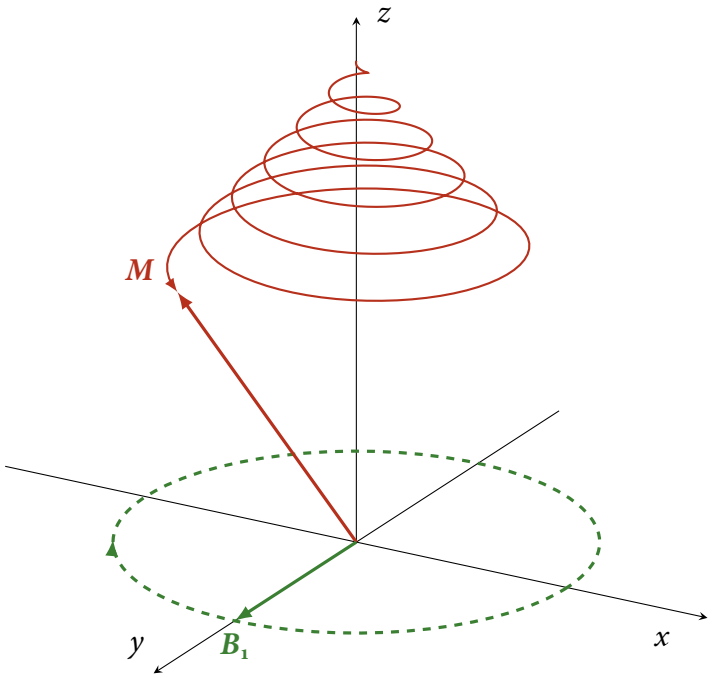

Figure 2.2: The effect of B_1 excitation in the laboratory frame of reference

A flip angle (FA) α associated with the $\boldsymbol{B_1}$ field is defined to describe how much has $\boldsymbol{M_0}$ moved away from $\boldsymbol{B_0}$ as a result of applying the $\boldsymbol{B_1}$ field. The flip angle depends on the amplitude and duration of the RF pulse, and it is given by eq. 2.8.

$$\alpha = \gamma \int_0^t B_1(\tau) d\tau \tag{2.8}$$

While the excited magnetisation vector is returning to thermal equilibrium, its transverse motion induces a voltage oscillating at the Larmor frequency in receiver coils placed in the xy plane. The magnitude of this voltage is proportional to $\sqrt{M_x^2 + M_y^2}$. The signal defined by this oscillating voltage is the NMR signal and it decays to zero as the $\boldsymbol{M_{xy}}$ component of the net magnetisation disappears. This decaying signal is called a free induction decay (FID) and its typical shape is shown in fig. 2.4. The Fourier-transform of the FID provides information on the frequency components the FID consists of and is called the NMR spectrum.

Equation 2.9, called the Bloch equation [18], describes the time evolution of the net

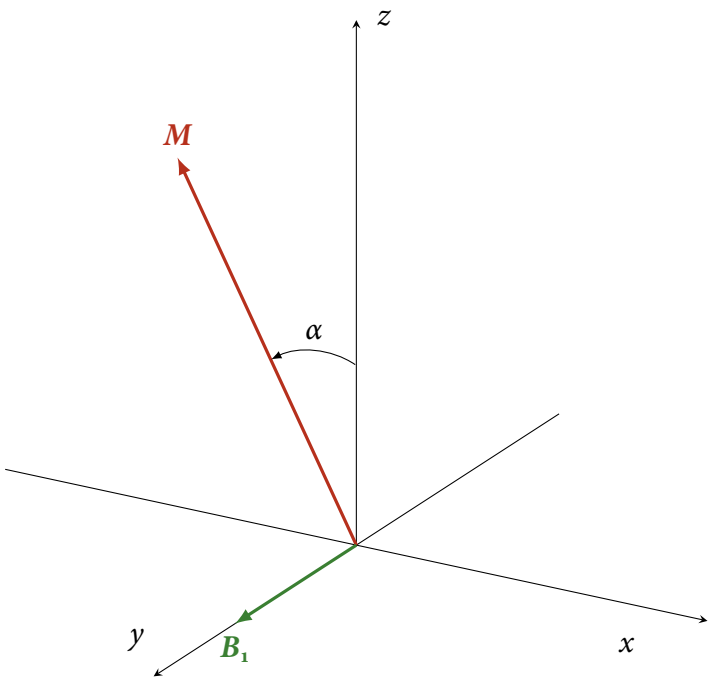

Figure 2.3: The effect of B_1 excitation in the rotating frame of reference

magnetisation vector, including terms for the precessional and recovery motions.

$$\frac{d\boldsymbol{M}(t)}{dt} = \gamma \boldsymbol{M} \times \boldsymbol{B} - \frac{\boldsymbol{M}_x(t) + \boldsymbol{M}_y(t)}{T_2} - \frac{\boldsymbol{M}_z(t) - \boldsymbol{M}_0}{T_1} \tag{2.9}$$

The last two components of eq. 2.9 describe the dephasing of spins in the xy transverse plane and the recovery of the net magnetisation to thermal equilibrium along the longitudinal z axis, respectively. These recovery processes are called T_1 and T_2 relaxation.

2.1.2.1 *T_1 relaxation*

T_1 relaxation arises as a result of individual nuclei interacting with their immediate environment (also called the lattice). As the RF pulse is removed during an NMR experiment, nuclei continue to precess only around $\boldsymbol{B}_0$, while also performing tumbling motion. Since spontaneous energy emission is highly unlikely in the radio-frequency domain [21], it is necessary that the rate of tumbling of nuclei to be at or around the Larmor frequency.

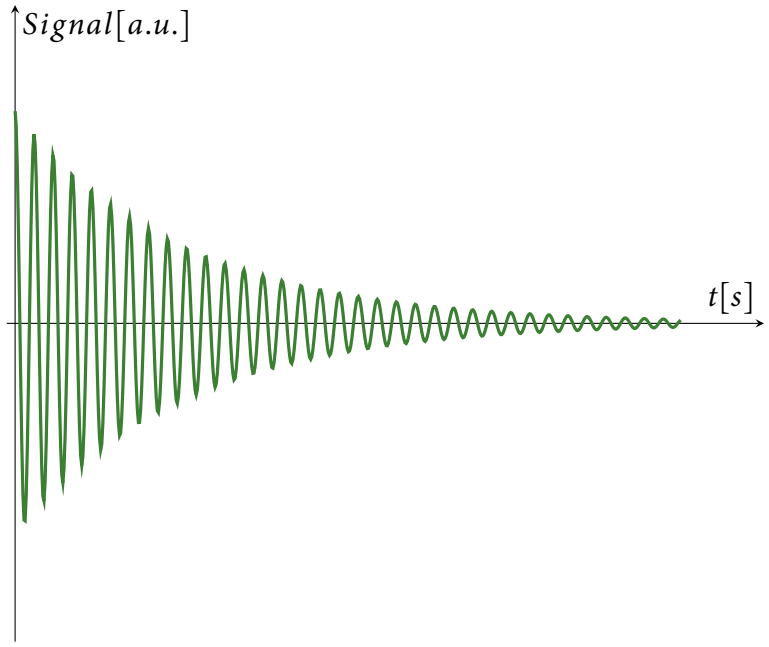

Figure 2.4: A typical FID signal

This will then cause the stimulated release of energy of excited nuclei into the lattice or environment in the form of thermal energy. T_1 relaxation is described by an exponential process and it is characterised by a time constant T_1, which is equal to the time necessary for the longitudinal magnetization component to recover to 63% of the initial net magnetisation. Solving eq. 2.9 for M_z yields eq. 2.10, which describes T_1 recovery.

$$M_z(t) = (1 - e^{-t/T_1})M_0 \tag{2.10}$$

T_1 relaxation is the most efficient, and, therefore T_1 is the shortest, when the molecular tumbling rate is closest to the Larmor frequency. The rate of tumbling of nuclei is determined by their freedom of movement. Therefore, water molecules with restricted movement (e.g. bound to immobile large molecules, such as proteins) have lower tumbling rates than structured water molecules (e.g. residing in tissue compartments), which, in turn, have lower tumbling rates than unrestricted water molecules (e.g. in free water or blood). Thus,

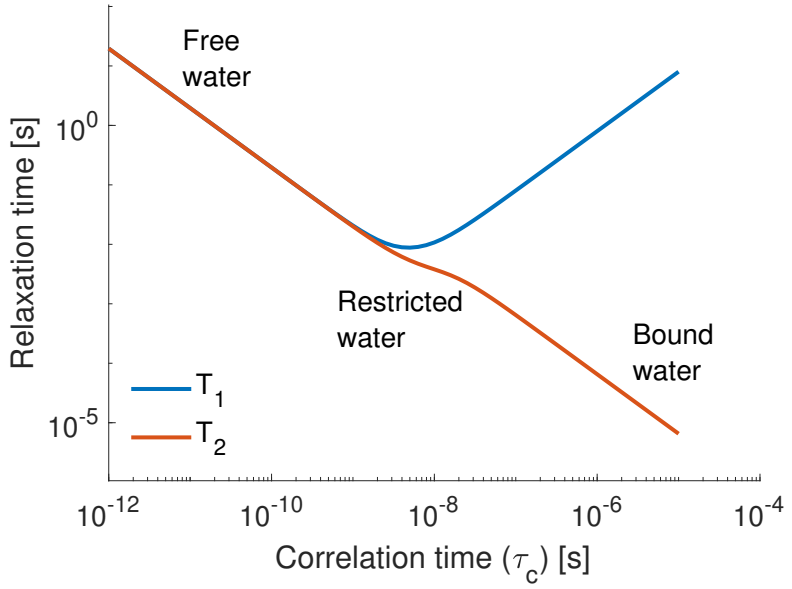

Figure 2.5: Dependence of relaxation times on the correlation time τ_c (i.e. the reciprocal of the tumbling rate)

protons in both restricted and free water pools will have higher T_1 times than protons in structured water pools, as fig. 2.5 also suggests. T_1 relaxation time is also dependent on the main magnetic field for protons in structured and restricted pools. Protons in free water are capable of tumbling over a wide range of frequencies, therefore, their T_1 relaxation times will not be significantly affected by an increase of the field strength. Immobile and restricted protons pools will only contain a fraction capable of tumbling at the new, higher frequency, leading, therefore, to a longer T_1 relaxation time, as explained by fig. 2.6.

2.1.2.2 *T_2 and T_2^* relaxation*

After removing the RF pulse, the net $\boldsymbol{M_{xy}}$ transverse magnetisation will start decaying due to individual nuclear spins losing phase coherence. This relaxation type is also called spin-spin relaxation, as the loss of phase coherence is caused by the effects of local magnetic microenvironments on surrounding spins. T_2 relaxation always occurs during T_1 relaxation: as spins are re-aligning with $\boldsymbol{B_0}$, they do not contribute to the phase coherence of the

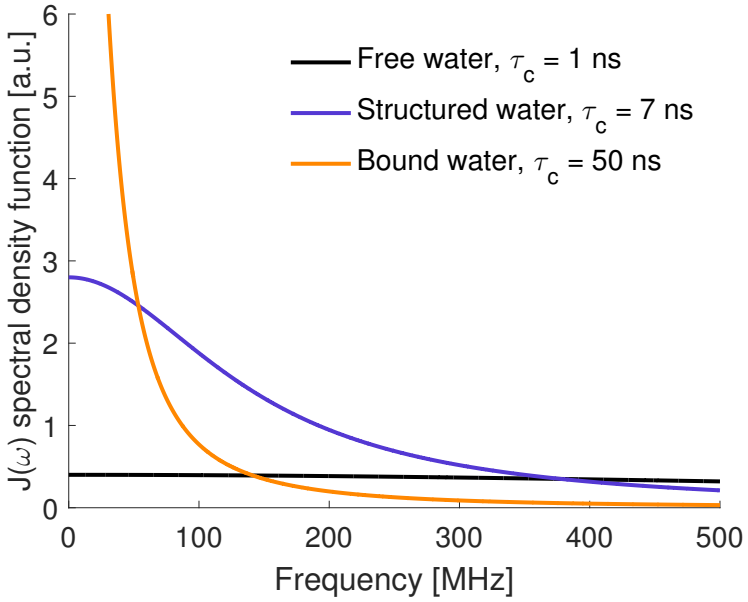

Figure 2.6: Spectral density functions of different water pools

remaining spins in the transverse plane anymore, therefore reducing the magnitude of the net $\boldsymbol{M_{xy}}$. T_2 relaxation is characterised by a mono-exponential decay and a corresponding T_2 time constant, which is the time when the transverse magnetisation has been reduced to 37% of the original transverse magnetisation. Equation 2.11 governs this type of relaxation.

$$M_{xy}(t) = M_0 e^{-t/T_2} \tag{2.11}$$

Local fixed inhomogeneities of the magnetic field, such as iron accumulation or the presence of haemoglobin and deoxyhaemoglobin, can also contribute to the decay of the net $\boldsymbol{M_{xy}}$. Spins located in local magnetic fields different from the main field will precess at frequencies different from the Larmor frequency, thus gaining or losing phase relative to spins that only experience the main field, leading to decay of the net $\boldsymbol{M_{xy}}$ in addition to T_2 decay. The presence of both transverse relaxation mechanisms is characterised by the T_2^* time constant, given by eq. 2.12.

$$\frac{1}{T_2^*} = \frac{1}{T_2} + \frac{1}{T_2'} \tag{2.12}$$

Here T_2' represents the decay constant due to ΔB_0 field inhomogeneities and is given by eq. 2.13.

$$\frac{1}{T_2'} = \gamma \Delta B_0 \tag{2.13}$$

T_2 relaxation does not change significantly over the clinical range of field strengths, however, at ultra high fields (e.g. 7 T) microscopic diffusion and susceptibility effects can lead to a decrease of T_2 relaxation times.

While T_2 relaxation is not reversible, T_2' relaxation can be by manipulating the radiofrequency pulses played out in a pulse sequence.

2.2 IMAGE FORMATION

The previously described FID signal originates from the entire excited volume and carries no spatial information. To be able to produce images, spatial encoding schemes need to be implemented. For this purpose, the bore of an MRI scanner is fitted with three so-called gradient coils, each of which creates a magnetic field whose z component is non-zero and varies linearly in the x, y and z directions. The total field experienced by spins will thus be the sum of the main magnetic field pointing in the z direction and the linear changes applied by one or more gradients. For example, when only the gradient along the x direction is applied, the total field is described by $B_z = B_0 + x\frac{dB_z}{dx} = B_0 + xG_x$, where x is the position in the x direction and G_x is the amplitude of the gradient in the x direction in units of $\mathrm{T\,m^{-1}}$.

In addition to their role in localising the MR signal, gradients are also used to homogenise the main magnetic field in the presence of an imaged object or human body. This process is called shimming.

2.2.1 *Slice selection*

To be able to select an imaging slice, both a gradient perpendicular to the desired slice and an RF pulse are necessary. The gradient will cause a local linear variation of the main field, creating a range of frequencies around the Larmor frequency at which spins will precess along the direction of the gradient. Then, the RF pulse, having a shaped envelope of a relatively narrow bandwidth, will excite only the spins that are precessing at frequencies falling within its bandwidth. The bandwidth of the pulse is centred on the Larmor frequency of spins located at the centre of the gradient field, i.e. where the main magnetic field is unchanged. Slice thickness can be controlled in two ways: changing the amplitude of the gradient while keeping the RF pulse constant or varying the bandwidth of the RF pulse, while using a constant gradient amplitude. In the first case, the larger gradient amplitude is used, the thinner the plane will be in which spins precess with frequencies covered by the RF bandwidth. Conversely, using the same gradient amplitude with an RF pulse that has a narrow bandwidth will result in a thin slice as opposed to using an RF pulse with a wide bandwidth, which results in a thick slice. Figure 2.7 illustrates the concept of slice selection, while fig. 2.8 represents a simple timing diagram of the slice selection process. The RF pulse is represented using its shaped envelope, e.g. a Gaussian pulse, while the gradient is illustrated using a trapezoid, suggesting that there is a delay between the application of a current through the gradient coil and the appearance of the effect of this current. Similarly, when the current is turned off, the linearly varying field will not disappear instantaneously, which is represented by the right edge of the trapezoid. The two delay times are called ramp-up time and ramp-down time. After the RF pulse has been played out, a gradient with negative amplitude has to be applied, such that the area under this second gradient equals the area under the slice selective gradient from the middle of the RF pulse until the

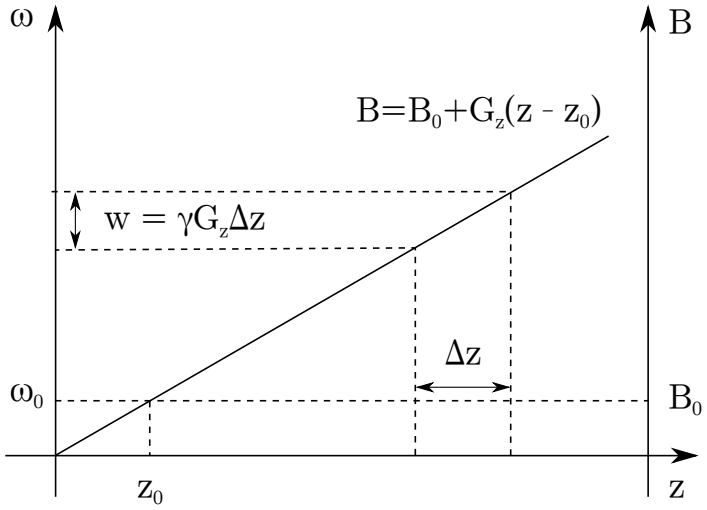

Figure 2.7: The principle of slice selection. *z* denotes position along the direction of the main magnetic field, and z_o is the point where the gradient field is zero and spins precess at the Larmor frequency.

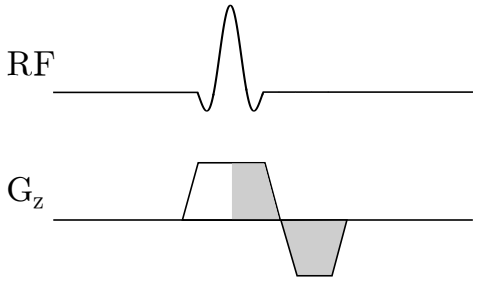

Figure 2.8: Simple sequence diagram illustrating slice selection

end of the slice selective gradient. This is necessary to balance phase dispersion occurring after spins at the centre of the slice had been excited. This "balancer" gradient is called a rephaser gradient and it has to be on the same axis as the slice selective gradient.

2.2.2 *Frequency encoding*

When a gradient is applied, the spins in the selected slice will precess at a frequency that is dependent on their position along the axis of the applied gradient, as shown in fig. 2.9. This allows spatial localisation of spins within a slice if the gradient is applied perpendicular to the slice selection gradient. The gradient that accomplishes this task is called a frequency

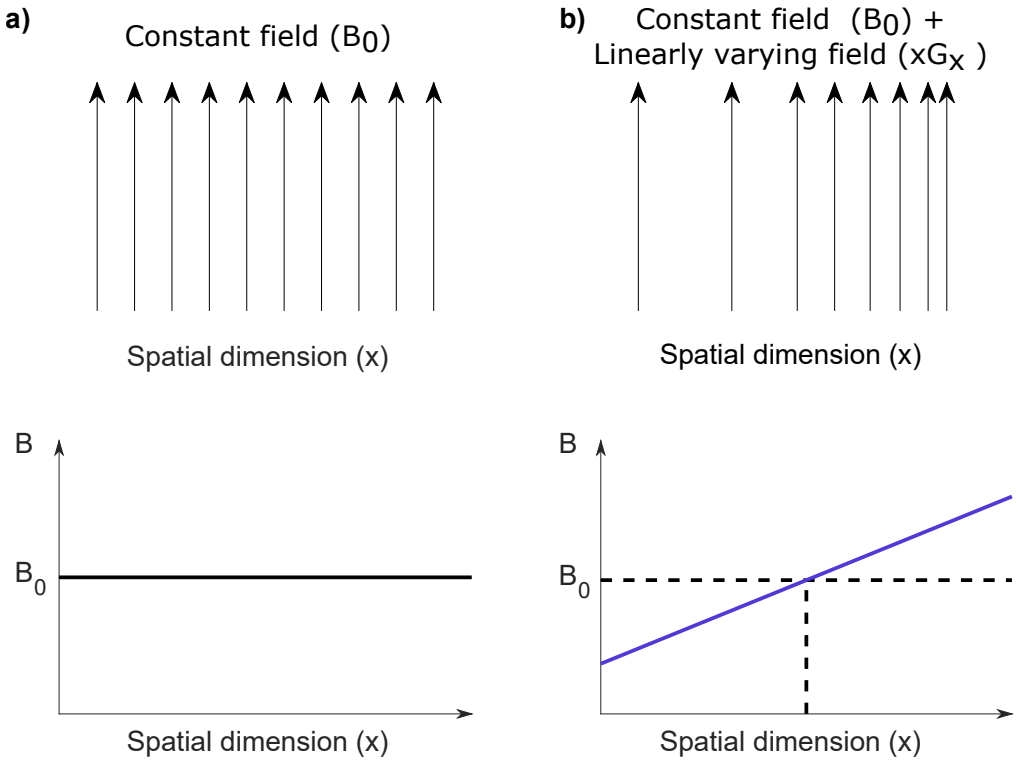

Figure 2.9: The principle of frequency encoding. All spatial locations experience the same field strength in the presence of only the main magnetic field (a), however, turning on an additional linearly-varying gradient field introduces a linear dependence of field strength on position (b).

encoding gradient or readout gradient. Frequency encoding is realised in two steps: first, a strong gradient is applied on the readout axis to forcefully dephase the magnetisation in the transverse plane. Then, a gradient with a smaller and opposite amplitude is applied on the same axis, which will rephase the magnetisation. Spins will get back into phase when the area under the smaller-amplitude gradient matches the area under the initial, dephaser gradient. The newly formed signal is called a gradient-recalled echo (GRE), because it is the echo of the FID signal reassembled with the help of the readout gradient. This gradient echo is sampled using an analog-to-digital converter at a resolution that matches the number of pixels necessary for the final image in the readout direction.

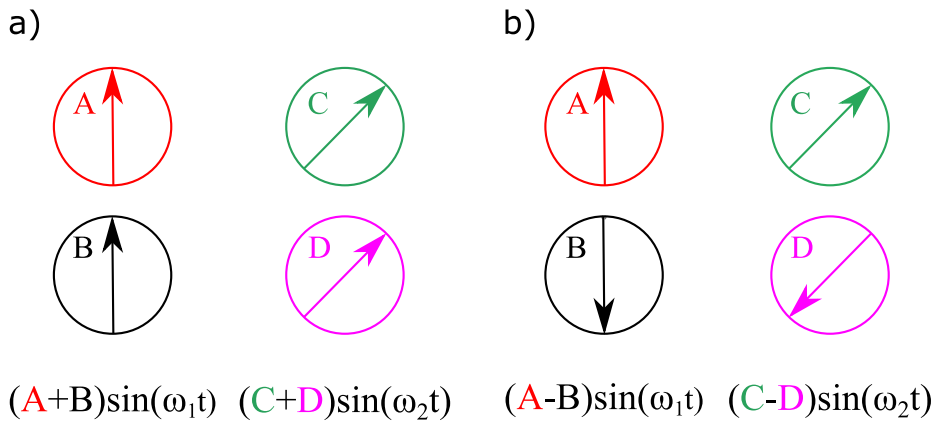

Figure 2.10: Phase encoding using two steps. Frequency encoding alone (a) cannot help in resolving the position difference between spins A and B, and C and D. Using a phase encoding gradient that introduces a phase difference of π between spins A and B, and C and D (b) gives enough additional information to resolve the spatial location of all four spins.

2.2.3 *Phase encoding*

To add a second dimension to the desired MR image, a third encoding step is needed, called phase encoding. This is achieved with the help of the gradient on the third axis. When a phase encoding gradient is turned on, spins start to accrue phase relative to each other while precessing at the Larmor frequency. After the phase encoding gradient is turned off, spins will stop accumulating further phase, while still precessing at the Larmor frequency. Then, as the frequency encoding gradient is turned on on a different axis, spins will start to precess at different frequencies, depending on their position but keeping the phase they acquired after phase encoding. After the MR signal has been acquired and a new RF pulse was played out, a phase encoding gradient of a different amplitude is applied, with an amplitude different from the first case. This new phase encoding gradient will result in a different phase relationship between spins, resulting in a different MR signal. Figure 2.10 illustrates phase encoding using two phase encoding steps and two encoded frequencies. For the first phase encoding step the phase encoding gradient is turned off and so spins will precess in phase. The measured MR signal will consist of two frequency components ω_1 and ω_2

each having an amplitude equal to the sum of pixel values corresponding to each frequency. The second phase encoding step will cause spins in the top row to have a phase of π with respect to the spins in the bottom row. After frequency encoding the resulting MR signal will contain the same two frequencies as before but with amplitudes corresponding to the difference between pixel values in the top row and pixel values in the bottom row. Each pixel value can now be determined from the two MR measurements. When acquiring an entire image, the number of phase encoding steps is several times larger than in the previous example, depending on the prescribed image size.

2.2.4 *k-space and image reconstruction*

Let's assume that N phase encode lines are collected at M frequency encode steps. The acquired N × M matrix is now in the spatial frequency domain, also called k-space. The acquired MRI signals that comprise k-space can be defined as the double integral of the time-invariant proton density ($\rho(x, y)$) over the imaged slice multiplied by the time-varying phase ($\varphi(x, y, t)$) evolution of the spins in the slice, as described by eq. 2.14. In this equation k is a weighting factor characteristic to the measurement system.

$$s(x, y) = k \int_x \int_y \rho(x, y) e^{-i\varphi(x,y,t)} dx dy \tag{2.14}$$

Since frequency is the time derivative of phase and taking the Larmor equation into account, when imaging at the isocentre we can write:

$$\begin{aligned} \varphi(x, y, t) &= \gamma \int_0^t B(x, y, \tau) d\tau \\ &= \gamma \int_0^t B_0 d\tau + \gamma x \int_0^t G_x(\tau) d\tau + \gamma y \int_0^t G_y(\tau) d\tau \\ &= \omega_0 t + 2\pi k_x(t) x + 2\pi k_y(t) y \end{aligned} \tag{2.15}$$

where $k_x = \gamma \int_0^t G_x(\tau)d\tau$, $k_y = \gamma \int_0^t G_y(\tau)d\tau$ and $\gamma = \gamma/2\pi$. Since the carrier frequency ω_0 can be demodulated from the acquired signal, the resulting equation establishes the relationship between MRI signals and k-space:

$$s(x,y) = \int_x \int_y \rho(x,y) e^{-2\pi i(k_x(t)x + k_y(t)y)} dxdy \tag{2.16}$$

Equation 2.16 is an inverse two-dimensional Fourier-transform (2DFT) of proton density, therefore, a simple 2DFT is necessary to retrieve the proton density map, i.e. the complex image space data. In the context of phase encoding and frequency encoding, the relationship between k-space and gradient amplitudes is given by eqs. 2.17 and 2.18, where G_{FE} is the amplitude of the frequency encoding gradient, ΔT is the sampling time during the acquisition process, ΔG_{PE} is the phase encoding gradient amplitude step size and τ is the duration of the phase encoding gradient, m and n represent the number of frequency encoding and phase encoding steps, respectively, such that $-\frac{N}{2} \leq n \leq \frac{N}{2} - 1$ and $-\frac{M}{2} \leq m \leq \frac{M}{2} - 1$

$$k_x = \gamma G_{FE} \Delta t m \tag{2.17}$$

$$k_y = \gamma \Delta G_{PE} \tau n \tag{2.18}$$

Figure 2.11 shows a sampled k-space and its corresponding image space. It is of interest that the centre of the k-space contains most of the signal and, since it corresponds to low spatial frequencies, gives contrast to the image. On the other hand, the edge of k-space, which corresponds to higher spatial frequency components, defines edges in the image space [22].

K-space can be populated with MR signals in multiple ways. One of the most popular ways is to fill k-space line-by-line as presented until now. Other, more complicated, k-space traversal methods include radial and spiral sampling, as shown in fig. 2.12.

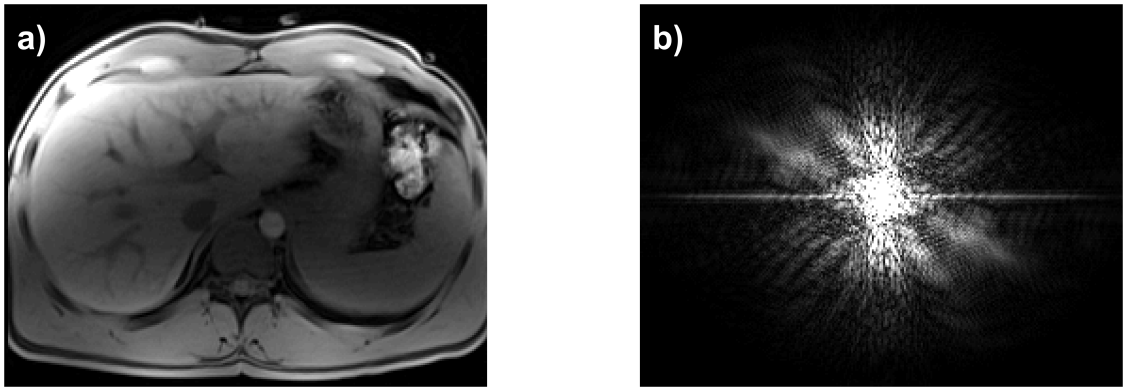

Figure 2.11: An example of image space (a) and k-space (b) pair. The centre of k-space contains contrast information about the image, while the edges of k-space define edges.

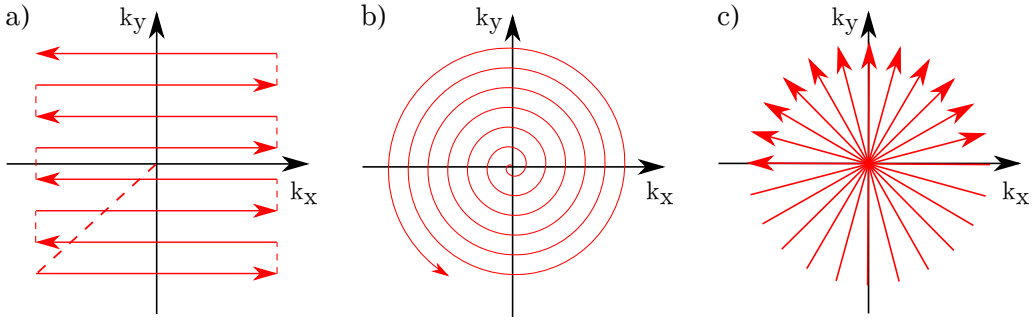

Figure 2.12: Different k-space traversal trajectories: echoplanar (a), spiral (b) and radial (c)

2.3 PULSE SEQUENCES

The combinations of RF pulses, gradients and associated timings determine a pulse sequence, which can provide images with a variety of contrast, emphasising different properties of tissue: T_1 and T_2 maps to explore water and protein content, T_2^* to determine the amount of iron, diffusion-weighted images to assess directionality. An MR scanner is also capable of providing spectroscopy measurements to provide information about metabolites in the tissue of interest.

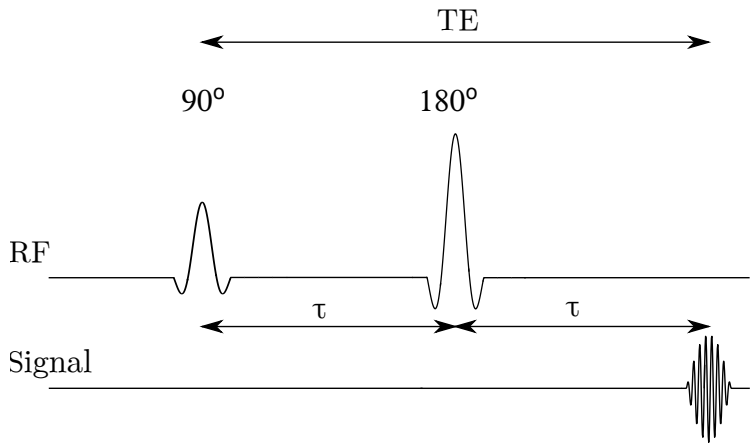

Figure 2.13: One TR interval of the spin echo pulse sequence

2.3.1 *Spin echoes*

A spin echo (SE) sequence employs a 90° excitation RF pulse on the x axis followed by a 180° refocusing pulse on the y axis after a τ delay time. The excitation pulse tips the longitudinal magnetisation into the transverse plane, where spins start to dephase. The refocusing pulse will reverse the phase of spins, and after another τ time has elapsed, spins will get back in phase again, to form an echo, called the spin echo [23]. This rephasing process eliminates phase loss due to fixed magnetic field inhomogeneities and magnetic susceptibility variations, but not T_2 decay. This is in contrast with the gradient echo, which is sensitive to T_2^* decay.

The time delay 2τ between the centre of the excitation RF pulse and the centre of the spin echo is called the echo time (TE), while the time delay between successive excitation pulses is called the repetition time (TR). Figure 2.13 shows a simplified pulse sequence diagram of a spin echo acquisition.

The acquired signal will depend on the proton density, T_1 and T_2 of the imaged tissues. Therefore, the signal intensity is defined by eq. 2.19 and reflects the many possibilities to

achieve contrast with the spin echo sequence.

$$S(TR, TE) = \rho e^{-TE/T_2}(1 - e^{-TR/T_1}) \tag{2.19}$$

Three types of contrast can be defined, based on the manipulation of TR and TE parameters:

- T_2-weighted: achieved by minimising the effects of T_1 recovery, i.e. by choosing a long repetition time, and choosing an echo time that allows for tissues with short T_2 to have lower intensity than tissues with longer T_2, because they decay faster during the allowed echo time;
- T_1-weighted: achieved by minimising the effects of T_2 relaxation, i.e. by choosing a short echo time, and choosing a repetition time that allows for tissues with short T_1 to have higher intensity than tissues with longer T_1, because they can recover more longitudinal magnetisation during the allowed repetition time;
- PD-weighted: achieved by minimising the effects of both T_1 recovery and T_2 relaxation, by setting a short echo time and a long repetition time, thus allowing tissues to give contrast only based on their proton density.

2.3.2 *Stimulated echoes*

There is a third way of giving rise to echoes in NMR in addition to spin echoes and gradient echoes. When using a train of three RF pulses, a total of five echoes appear, as shown in fig. 2.14. Echoes E_1, E_4 and E_5 are spin echoes that appear as a result of applying the pairs of pulses θ_1 and θ_2, θ_2 and θ_3, and θ_1 and θ_3. Echo E_3 appears as a secondary echo of echo E_1, after the dephased spins from echo E_1 are refocused again by pulse θ_3. Echo E_2 is called a stimulated echo, and it arises as the combined effect of the three RF pulses. The first pulse tips the magnetisation into the transverse plane along the x axis, where spins start to

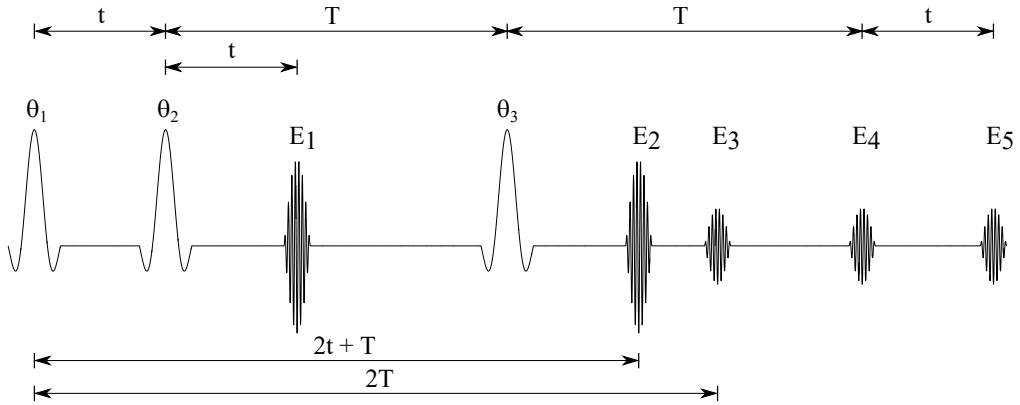

Figure 2.14: Echoes resulting from three RF pulses (θ_1, θ_2 and θ_3) of equal flip angle

dephase. Then, the second pulse brings back the spins along the x axis into the vertical xz plane where T_2 decay is suspended for spins along the z axis, however, T_1 recovery begins. When the third pulse flips spins into the transverse plane again along the x axis, spins that were accumulating phase will start losing phase and vice versa, leading to the formation of the stimulated echo. The signal amplitude is given by eq. 2.20 [24] and is subject to spins being dephased during the first interval and diffusion being negligible.

$$S(TM, TE) = \frac{S_0}{2} \sin\theta_1 \sin\theta_2 \sin\theta_3 e^{-TE/T_2} e^{-TM/T_1} \tag{2.20}$$

2.3.3 *Fast imaging with balanced steady-state free precession*

Previous sections have described how one RF pulse produces a FID, two RF pulses give rise to an echo and three RF pulses produce a stimulated echo. However, many more RF pulses can be played out in quick succession to reach both a longitudinal and a transverse steady-state magnetisation when using a constant TR, which is shorter than the T_2^* of the imaged tissue. The FIDs and echoes overlap during the short TR interval and give rise to a transverse magnetisation that never vanishes completely, an effect called steady-state free precession (SSFP). The most commonly used SSFP sequences are based on the GRE

sequence, which is slightly modified to meet the criteria for the existence of sustained (coherent) steady-state transverse magnetisation:

- The TR needs to be much shorter than the T_2, otherwise the coherence will be broken as the signal decays;
- Phase shifts over a TR interval must be constant. This means that the phase encoding gradient will have an additional lobe, with an equal area of the phase encoding gradient. This lobe is called a rewinder gradient;
- RF pulses must have the same phase or be subjected to a simple phase cycling scheme (e.g. $+\theta$, $-\theta$, $+\theta$, ...).

By manipulating the gradients in various ways, it is possible to refocus either the FID-like, the echo-like or a combination of both FID- and echo-like signals.

When a combination of the FID-like and echo-like signals is acquired, the SSFP sequence is called balanced SSFP, since the gradient moments over one TR interval are zero on each axis, as illustrated by fig. 2.15. This characteristic of the bSSFP sequence means that there is no dephasing due to gradients over one TR interval, therefore, the only phase accrual can be due to differences in the precession of isochromats, leading to the frequency-dependence of the bSSFP signal. This frequency dependence is illustrated by fig. 2.16. The signal acquired by a bSSFP sequence in the steady-state is given by eq. 2.21 for the case when sign-alternating RF pulses are used on resonance.

$$S(\theta, TR, TE) = M_0 \sin\theta \frac{1 - e^{-TR/T_1}}{1 - \left(e^{-TR/T_1} - e^{-TR/T_2}\right)\cos\theta - e^{-TR/T_1}e^{-TR/T_2}} e^{-TE/T_2} \tag{2.21}$$

For short repetition times (i.e. $TR \ll T_2 \ll T_1$; typical TR values at 3 T are in the 2.1–2.5 ms range), the following simplifications can be made: $e^{-TR/T_1} = 1 - TR/T_1$ and $e^{-TR/T_2} =$

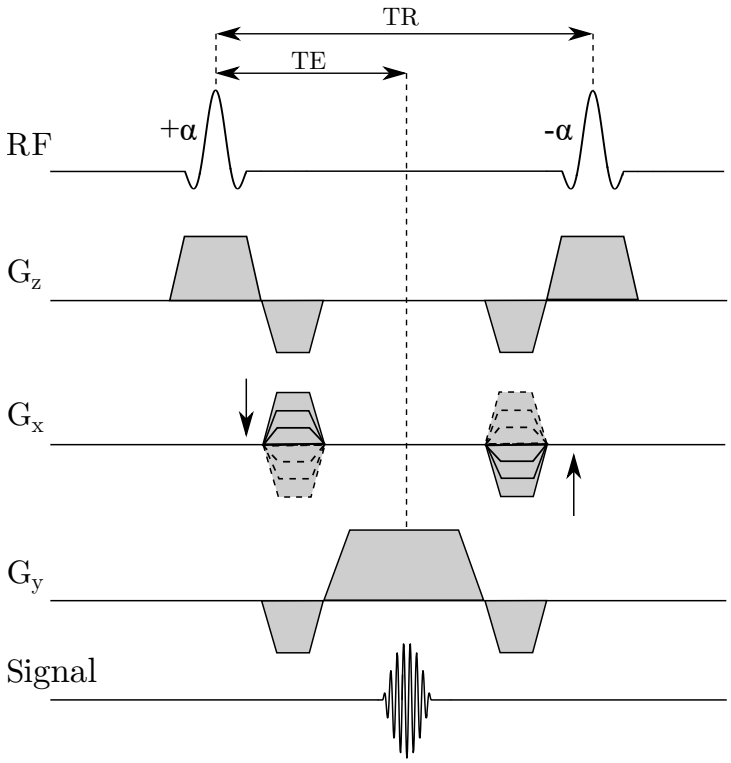

Figure 2.15: One TR interval of the balanced steady-state free precession sequence, with symmetric readout (TE = TR/2)

$1 - TR/T_2$, resulting in the simplified bSSFP signal:

$$S(\theta, TR, TE) = \frac{M_0 \sin\theta}{(T_1/T_2)(1-\cos\theta)+1+\cos\theta} e^{-TE/T_2} \tag{2.22}$$

The final T_2 decay term is only valid when an echo time equal to half of the repetition time is used, i.e. a symmetric echo is formed, making the bSSFP sequence a spin-echo-like sequence. In case of an asymmetric echo, the T_2 decay term becomes a T_2^* decay term.

The bSSFP sequence is often said to have T_2/T_1 contrast, due to the T_1/T_2 factor in the denominator of eq. 2.22, explaining the hyperintense signal from fat and fluids. For flip angles near 90°, the equation becomes more strongly dependent on the T_2/T_1 ratio, providing relatively high signal-to-noise ratio (SNR) and high fluid-muscle contrast for a sequence with very short TR intervals. Due to this property, the sequence is often used in

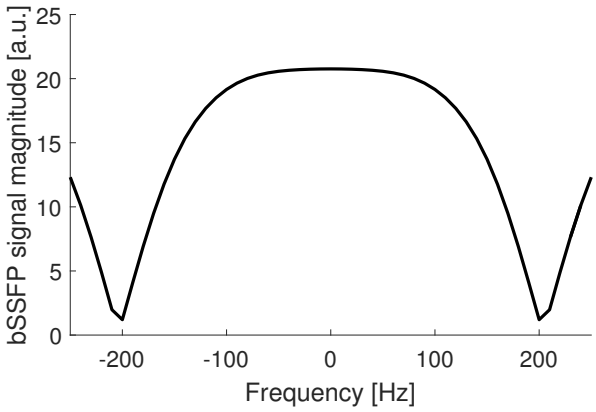

Figure 2.16: Frequency dependence of the bSSFP signal when a pulse sequence depicted in fig. 2.15 is used with TR = 2.3 ms and TE = 1.15 ms. Transition bands of the signal are responsible for characteristic "black bands"

cardiac applications.

One drawback of the bSSFP sequence is that the approach to the coherent steady-state can take a long time, i.e. over several T_1s. To accelerate this, several catalysing methods have been developed: using a $\theta/2$ flip angle excitation pulse at a TR/2 interval before the main excitation pulse train [25] or using linearly increasing flip angle pulses [26, 27] before the main excitation pulse train.

2.3.4 *MR spectroscopy using stimulated echoes*

The chemical structure of a tissue is sometimes of interest, especially in disease. Several conditions of the brain, heart and liver cause changes in the balance of metabolites, which can accurately be assessed using classical, narrow-bore NMR experiments. However, this would necessitate taking a sample of the tissue of interest. In most cases this is not possible either because of the risk of complications or the need for periodic follow-up. In such cases magnetic resonance spectroscopy (MRS) can be a helpful tool. In its most simple embodiment, an MRS experiment is not localised and it is equivalent to collecting a FID

signal. This signal, once Fourier-transformed, provides information about the metabolites in the examined tissue or body part. Different metabolites can be identified based on their position, or chemical shift, in the MR spectrum. This chemical shift is defined by the geometry of the metabolite and the local magnetic environment of ^{1}H protons in the metabolite. In other words, the chemical shift of a metabolite peak represents the resonant frequency of that peak. Although it represents a frequency, it is seldom expressed in units of Hz, most often it is given in units of parts per million and it is defined by eq. 2.23.

$$\delta = \frac{f_{sample} - f_{reference}}{f_{reference}} \tag{2.23}$$

As it is normalised to the frequency of a reference material ($f_{reference}$) it is independent of the magnetic field strength. MRS sequences used in clinical practice and research scans are usually localised and single-voxel spectroscopy (SVS) sequences constitute a special subset of these. One of the most popular variants employs the stimulated echo acquisition mode (STEAM) [28]. Figure 2.17 shows the pulse sequence for this MRS acquisition. The three 90° excitation pulses are not only responsible for the creation of a stimulated echo, but they are also used for localising a voxel of interest, with the help of gradients on each axis. Additional gradients are added to suppress the creation of regular, spin echoes. When assessing the liver, this sequence can be used to determine the amount of fat present in liver cells. A typical ^{1}H spectrum of a liver is shown in fig. 2.18 with water and fat peaks identified. To calculate the fat fraction using this spectrum, the sum of the integrals of the fat peaks is divided by the sum of the integrals of the water and fat peaks. This value is often confounded by T_2 relaxation effects, since livers contain some amount of iron, which causes accelerated dephasing of protons. To correct for this bias, spectra are usually collected at multiple echo times and a T_2 correction of the peaks is performed before calculating the fat fraction [29].

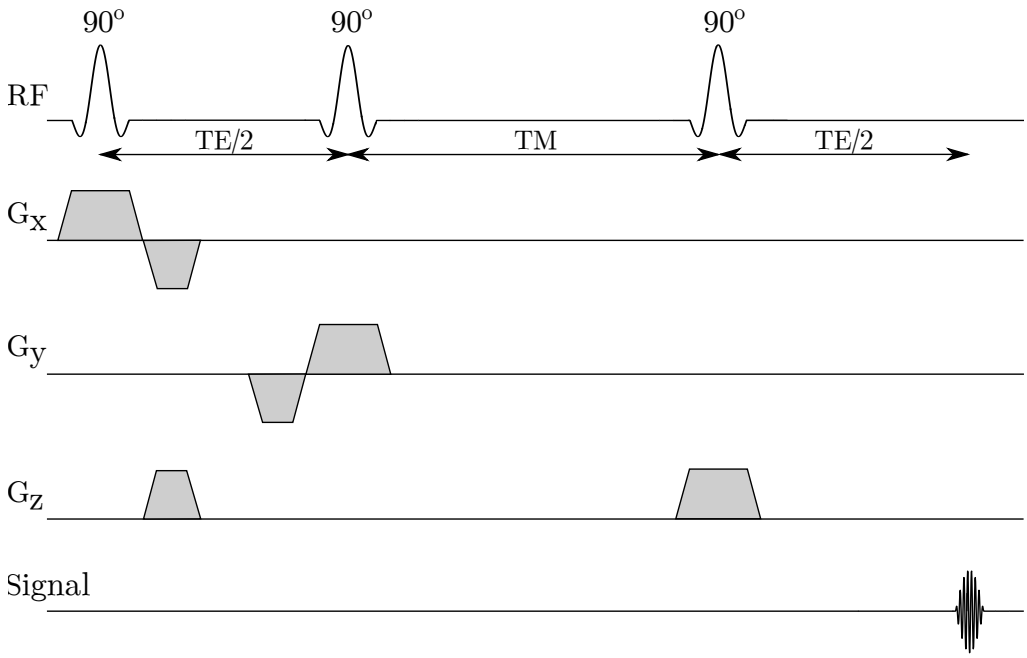

Figure 2.17: The STEAM spectroscopic pulse sequence

2.4 APPLICATIONS

The pulse sequences presented so far are rarely used on their own with only one set of parameters, especially when it comes to quantitative MRI. T_2 maps can only be determined by fitting the decay of a spin echo signal over multiple echo times, T_2^* maps necessitate multiple echo times of a GRE experiment, while T_1 maps need the collection of images at different repetition times. The spin echo and gradient echo sequences are often repeated to form a longer acquisition or they can be preceded by special combinations of RF pulses and gradients that prepare the magnetisation for a specific purpose, e.g. saturating fat, suppressing water, inverting the longitudinal magnetisation. This section briefly presents some of the more important derived pulse sequences and data processing techniques used throughout the rest of the chapters.

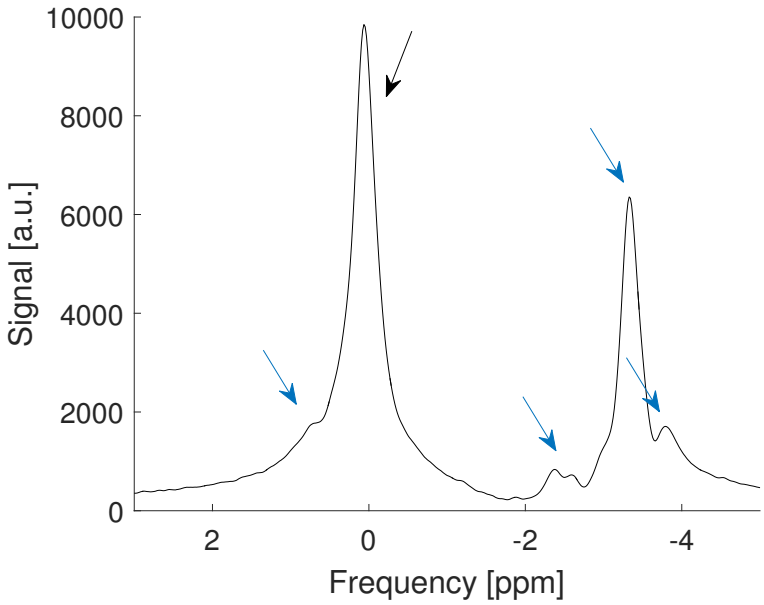

Figure 2.18: Typical appearance of a ^{1}H spectrum of a human fatty liver. The black arrow points to the water signal, while blue arrows show typical locations of fat peaks

2.4.1 *Shortened modified Look-Locker inversion recovery T_1 mapping*

Measuring T_1 can be achieved in a variety of ways. Perhaps the most obvious approach is to use spin echoes by successively applying $90°_x$ pulses followed by subsequent $180°_y$ pulses at different repetition times over the recovery curve of the longitudinal magnetisation. Alternatively, the longitudinal magnetisation can be inverted from the initial M_{z0} value to a $-M_{z0}$ value and performing the spin echo experiment at different inversion times (TI), i.e. different distances in time from the initial inversion pulse. While classical spin echo experiments take a relatively long time, they can be combined with accelerated readout techniques which allow their usage for imaging parts of the body that are subject to cardiac or respiratory motion. The bSSFP sequence, as seen previously, is capable of producing high-SNR images in a very short amount of time. Swapping the spin echo readouts with bSSFP readouts in the inversion recovery experiment and synchronising the acquisition of an entire image with a specific contrast, i.e. collected at a specific TI, to the electrocardiogram (ECG)

of a subject, leads to the MOLLI experiment [30]. While synchronising the imaging readouts to the participant's ECG is important when imaging the heart, this is not necessary for producing T_1 maps of abdominal organs. Given the known influence of participants' heart rate on measured T_1 values [31], replacing physiological ECG-triggering with a simulated ECG of constant rate might reduce T_1 dependence due to variations in heart rhythm. When

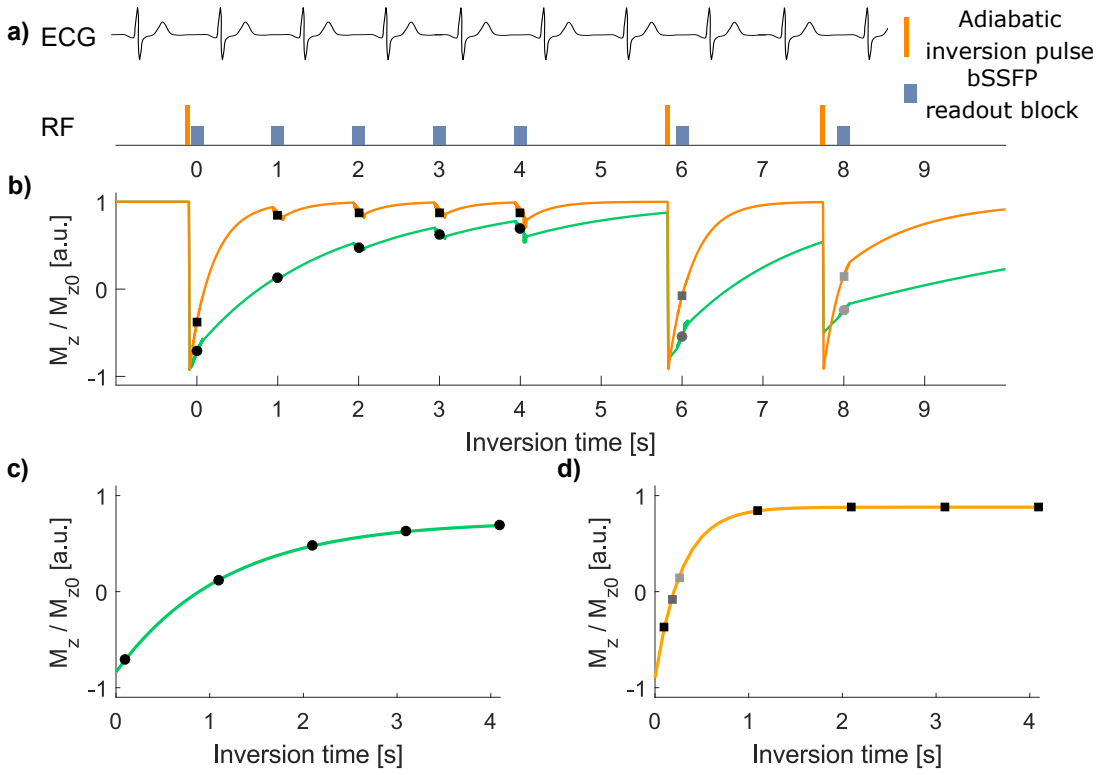

Figure 2.19: Simplified pulse sequence diagram of the shMOLLI T_1 mapping sequence. Balanced SSFP readout blocks (consisting of a train of 35° pulses) are synchronised to the dyastole of the cardiac cycle and follow adiabatic inversion pulses (a). The natural M_z time evolution (b) for species with a long (green) and short (orange) T_1 is interrupted by the bSSFP readouts. Black dots mark the centre of k-space. After reordering individual readouts according to inversion time, mono-exponentials can be fitted to the readout values to obtain T_1 values. As per the shMOLLI conditional fitting algorithm, five points are used for long T_1s (c) and all seven points are used for short T_1 fitting (d).

using a bSSFP readout during an inversion recovery experiment, the T_1 recovery is disturbed whenever a pulse train with short TR is applied, leading to an underestimation of the T_1.

The sampled recovery signal is fitted to eq. 2.24.

$$S(TI) = A - Be^{-TI/T_1^*} \tag{2.24}$$

where T_1^* is called the apparent T_1 relaxation time and it is shorter than the real T_1 relaxation time of the imaged tissue. To correct for the underestimation, the Deichmann-Haase formula [32] is used, as given by eq. 2.25. While the use of this correction formula is widely accepted, it should be noted that it only holds for small flip angles (FA < 10°).

$$T_1 = T_1^* \left(\frac{B}{A} - 1 \right) \tag{2.25}$$

The original MOLLI experiment collected 11 images over a single, 17 heart-beat long breath-hold to produce a single-slice T_1 map. To reduce the length of the breath-hold, which may be uncomfortable for some patients, a shortened version of the MOLLI sequence was developed, called shortened-MOLLI [31]. The shMOLLI sequence only acquires 7 bSSFP images over a 9 heart-beat long breath-hold as shown in fig. 2.19 to produce a single-slice T_1 map. The fitting of the recovery signal is done using a conditional fitting algorithm, which is dependent on an initial estimation of the T_1 using the first 5 images and the heart-beat interval (R-R interval).

2.4.2 *Fat-water separation, T_2^*, and B_0 mapping using gradient echoes*

When using fast spoiled GRE imaging techniques, the acquired signal can be described by eq. 2.26 at any given echo time, where ρ_W and ρ_F are proton densities of water and fat, P is the number of fat spectral peaks considered, α_p is the relative amplitude of the pth peak, such that $\sum_{p=1}^{P} \alpha_p = 1$, f_p is the chemical shift offset of the pth fat peak relative to water and φ is the phase shift due to field inhomogeneities.

$$S(TE) = \left(\rho_W e^{-TE/T_2^{*}{}_W} + \rho_F e^{-TE/T_2^{*}{}_F} \sum_{p=1}^{P} \alpha_p e^{2\pi i f_p TE} \right) e^{-2\pi i \varphi TE} \tag{2.26}$$

$T_2^*{}_W$ and $T_2^*{}_F$ are often considered to be equal [33], leading to the simplified eq. 2.27, where $K = \rho_W + \rho_F$ and $PDFF = \rho_F/(\rho_W + \rho_F)$.

$$S(TE) = e^{-TE/T_2^*} K \left((1 - PDFF) + PDFF \sum_{p=1}^{P} \alpha_p e^{2\pi i f_p TE} \right) e^{-2\pi i \varphi TE} \tag{2.27}$$

The only unknown parameters in eq. 2.27 are T_2^*, K, PDFF and φ, which can be found by fitting the equation to a GRE signal obtained at a number of echo times. This fitting is known as the T_2^*-iterative decomposition of water and fat with asymmetric echo times and least-squares estimation (T_2^*-IDEAL) algorithm [33, 34] and results in a PDFF, a T_2^* and a B_o field map. A short first echo time is needed to quantify short T_2^* values and longer echo times are needed to quantify longer T_2^* values. Therefore, a multiple-echo spoiled GRE sequence is often employed to acquire data that will be analysed using the T_2^*-IDEAL method. To maximise the noise performance of the fitting [35], and to make the fitting of all three parameters possible, a set of optimal echo times must be employed during the acquisition, spaced asymmetrically.

An alternative way of determining a PDFF map is offered by the two-point Dixon method [36], which also forms the basis of the IDEAL algorithm. In this case, a double-echo acquisition is performed at two echo time at which the water and the main fat peak are out of phase and in phase. Since the chemical shift difference between the two peaks is $\delta = 3.4$ ppm, the echo times of choice are $TE_{out} = 1.15$ ms and $TE_{in} = 2.3$ ms at 3 T and $TE_{out} = 2.3$ ms and $TE_{in} = 4.6$ ms at 1.5 T. Then, given the fat and water components of the measured signal can be calculated using eq. 2.28.

$$\begin{cases} S_{in} = W + F \\ S_{out} = W - F \end{cases} \Leftrightarrow \begin{cases} W = \dfrac{S_{in} + S_{out}}{2} \\ F = \dfrac{S_{in} - S_{out}}{2} \end{cases} \tag{2.28}$$

Then, the proton density fat fraction (PDFF) can be calculated using eq. 2.29.

$$PDFF = \frac{S_{in} - S_{out}}{2S_{in}} \tag{2.29}$$

A major drawback of this water-fat separation method is its dependence on perfectly homogeneous B_0 field, which is rarely achievable, therefore fat and water will never be truly in or out of phase. However, the method is still used for rough fat fraction approximation.

2.5 SUMMARY

The theoretical aspects presented in this chapter form the basis of experiments and volunteer studies presented in subsequent chapters. In particular, this chapter focused on describing pulse sequences used for relaxometric quantitation as well as sequences used to measure iron and fat concentrations in the liver.

3

Imaging the liver

3.1 ANATOMY, PHYSIOLOGY AND PATHOLOGY OF THE LIVER

The liver is a large organ located in the upper right quadrant of the abdominal cavity. It weighs 1.5-2 kg in a healthy person, but can reach a several-fold increase in weight in severe cases of cirrhosis. The liver is the main organ responsible for metabolism, energy storage and production as well as bile production and iron storage.

3.1.1 Anatomy

The liver comprises the left, right, caudate and quadrate lobes and it is attached to the diaphragm by the coronary ligaments and to the anterior abdominal wall by the falciform ligament. Another classification of liver regions was developed by Couinaud et al. [37] and divides the liver in 9 segments, as seen on fig. 3.1. Blood is supplied to the liver by two vessels: the hepatic artery and the portal vein; filtered blood from the liver is drained into the inferior vena cava (IVC) via the hepatic venous system [38]. The hepatic artery is

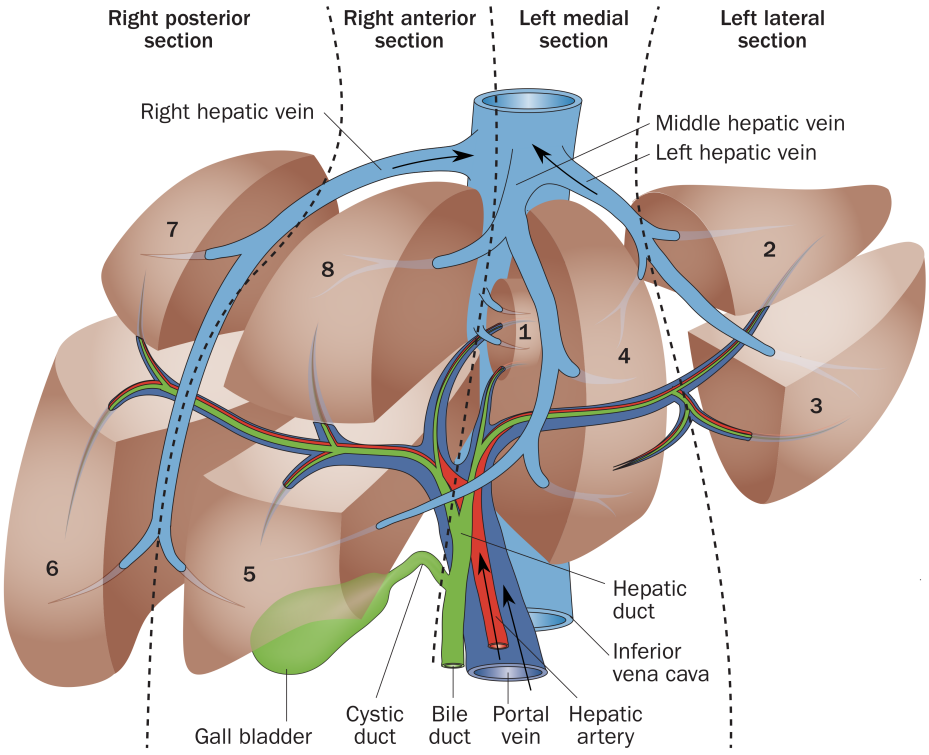

Figure 3.1: Anatomical structure of the liver showing the Couinaud segments. Reprinted by permission from RightsLink Permissions Springer Customer Service Centre GmbH: Springer Nature, Nature Reviews Clinical Oncology (Management of colorectal cancer presenting with synchronous liver metastases, Ajith K. Siriwardena, James M. Mason, Saifee Mullamitha, Helen C. Hancock, Santhalingam Jegatheeswaran, Copyright 2014)

responsible for approximately 25% of the blood supply while the rest is covered by the portal vein, which provides nutrients collected from the spleen and the intestines. The pressure in the portal vein is 3-5 mmHg in healthy humans [38], but can increase in severe stages of cirrhosis, termed portal hypertension.

Bile produced by the liver is emptied into the gallbladder via the common bile duct. The gallbladder stores and concentrates bile and releases it into the duodenum also via the common bile duct when it is stimulated by the secretion of cholecystokinin as a result of thinking about food or food entering the digestive tract. Once the bile is in the intestines, it

helps digestion by emulsifying fats in food.

The lobes of the liver consist of hexagonal hepatic lobules of about 0.7 mm × 2 mm in size [39], as depicted in fig. 3.2. Each of the lobules contains liver cells, or hepatocytes,

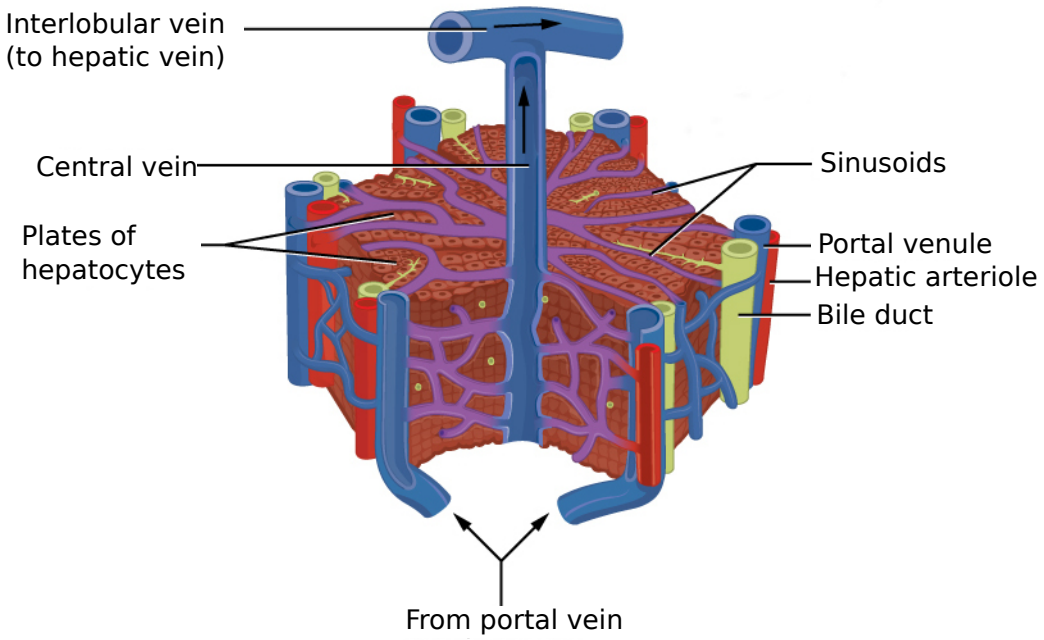

Figure 3.2: The basic structural unit of the liver parenchyma: the hepatic lobule. Figure adapted from OpenStax College - Anatomy & Physiology (CC-BY-3.0 license)

organised in rows surrounding sinusoids radiating from the central vein, which joins the hepatic vein. At the corners of hepatic lobules there are portal triads consisting of a portal venule, a hepatic arteriole and a biliary duct. Blood from the portal venule and the hepatic arteriole is mixed in the sinusoids and is drained by the central vein.

3.1.2 *Physiology*

A more functional definition of the hepatic parenchyma is depicted in fig. 3.3. A portal lobule is a triangular unit of liver parenchyma with a portal triad in the middle of the triangle and central veins in the corners. This unit covers the portion of parenchyma that is

responsible for bile production and secretion into the central bile duct of the portal triad. Another functional unit is the liver acinus, which covers metabolic activity, blood perfusion. A liver acinus is rhombus shaped, with its long axis connecting central veins and its short axis connecting portal triads. An acinus is divided into three zones:

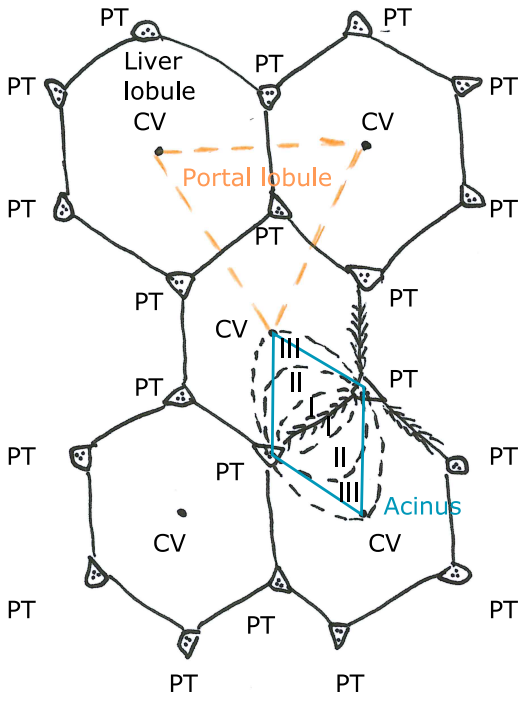

Figure 3.3: Structural and functional organisational units of the liver parenchyma

- Zone I: represents hepatic tissue closest to the portal triads, along the short axis of the acinus. Blood is most oxygenated in this zone and oxidative metabolism takes place here (e.g. gluconeogenesis)
- Zone II: hepatocytes in this zone are second to receive blood, although not as oxygenated as in zone I.

- Zone III: contains cells closest to the central vein. Blood reaching this zone is poorly oxygenated and lacking glucose, as that was absorbed by hepatocytes in zones I and II.

The liver has several metabolic functions, including

- Glucose metabolism: after a meal, blood containing high levels of glucose is filtered by periportal hepatocytes and the glucose is synthesised into glycogen (a process called glycogenesis). Conversely, when blood glucose levels are low after a fasting period, glycogen is broken down to glucose again and is released in the blood. Glycogen stores can contribute up to 8% of the weight of the liver.

- Lipid metabolism: the liver performs fatty acid oxidation for energy production. Excess saccharides are transformed into triacylglycerides (or triglycerides), which are then stored in adipose tissue. Lipoproteins are also synthetised in the liver: very-low-density lipoproteins (VLDL) and high-density lipoproteins (HDL) originate in the liver and are responsible for trygliceride transport in the body. Upon disregulation of lipid metabolism, excess lipid is stored inside the liver, a condition called steatosis.

- Iron storage: the liver is responsible for the regulation of iron homeostasis. Dysregulation results in iron disorders such as anaemia or iron overload. Iron is most commonly stored in ferritin molecules, however, in severe cases of iron overload, the concentration of ferritin saturates and degraded ferritin along with ferric hydroxides clump together to form haemosiderin, a highly immobile and insoluble complex [40].

3.1.3 Diseases of the liver

There are several causes that can lead to development of liver disease: viral infection, obesity, the presence of metabolic syndrome, diabetes mellitus, excessive alcohol consumption and genetic conditions. Based on the underlying cause(s), liver diseases can belong to one or more of the following categories:

Alcohol-related liver disease (ALD) Develops as a result of excessive alcohol consumption. It does not produce symptoms usually until the liver reaches a severely damaged state.

Non-alcoholic fatty liver disease (NAFLD) Can be the result of an unhealthy lifestyle or can be induced by certain medicines. It is of special interest as its world-wide prevalence has drastically increased recently [8] and patients are asymptomatic until the late stages of the disease. NAFLD ranges from simple steatosis (fat build-up in the liver), through fibrosis (scarring of the liver) to cirrhosis and, in some cases, hepatic carcinoma [41]. Like ALD, NAFLD often does not produce symptoms until the disease is well-advanced.

Hepatitis Caused by a viral infection, such as hepatic A, B, C, D and E viri, but drugs, alcohol and metabolic disease can also cause inflammation of the liver.

Haemochromatosis A genetic condition causing the gradual build up of iron in the body. Iron overload can lead to liver, heart, pancreas and joint injury.

Primary biliary cholangitis (PBC) It is an autoimmune disease of the liver, in which small bile ducts are progressively destroyed, resulting in the build up of bile in the liver. PBC can ultimately cause liver fibrosis and, eventually, cirrhosis.

Although liver enzymes (e.g. aspartate aminotransferase, alanine aminotransferase and gamma glutamyl transferase) can be measured from blood samples, they aren't specific enough [42] to provide a clear diagnosis of fibro-inflammatory disease and a liver biopsy is sometimes needed. Liver biopsies are considered to be the gold standard for a number of liver injuries, including ALD and NAFLD. However, it has been pointed out by several authors, that the evaluation of biopsies can be subjective due to high intra- and interobserver variability [43, 44], small biopsy sample size [45] or sampling variability [46]. The outcome of biopsy evaluation is also prone to discrepancies between staging and grading the biopsy and the underlying physical changes characteristic of a certain disease. For instance, staging liver fibrosis does not reflect the amount of collagen, but the architectural features of the biopsy sample [43]. Most liver biopsy evaluation methods provide a semi-quantitative description of chronic liver disease with specific components of grades and scores for inflammation, fibrosis, steatosis and cellular ballooning. The most frequently used fibrosis scoring systems are the NASH Clinical Research Network (NASH CRN) [47] and the Ishak [48] scoring systems. Biopsies also have a 0.13–3.20% rate of complications and 0–0.33% rate of mortality [49].

3.2 IMAGING THE LIVER

As described above, diagnosing liver disease is difficult and often involves invasive procedures. Since many liver pathologies only start producing symptoms when they are in an advanced stage (most notably NAFLD), it is important to have non-invasive, safe and reproducible diagnostic modalities. This section discusses some of the most widely used imaging techniques and their performance in diagnosing NAFLD.

3.2.1 *Ultrasound*

Ultrasound (US) is a cost-effective and readily available technique, often used as a first-line diagnostic tool for the assessment of liver injuries, that captures the reflection of a beam of ultrasound transmitted by a transducer to form images of organs.

Livers with NAFLD uniquely produce bright hepatic echoes, increased hepato-renal echogenicity and vascular blurring of the portal or hepatic vein [50], with US images being shown to be capable of predicting the presence of NAFLD at hepatic steatosis levels over 20% (as determined by biopsy) with a sensitivity over 90%, but sensitivity dropped at low levels of fat [51]. Another study has demonstrated that considering subcutaneous fat thickness, liver heterogeneity, lack of well-defined edges and the already-mentioned echogenicity can yield to a sensitivity of 80% and specificity of 99% when diagnosing NAFLD [52]. While routine US offers an easy way to confirm the presence of NAFLD, it is a poor predictor of fibrosis [53, 54]. However, it has been shown that when parenchymal texture was combined with liver surface nodularity and bluntness of the liver edge, correlation with the degree of fibrosis was $r = 0.95$ [55].

3.2.2 *Transient elastography*

Liver fibrosis and cirrhosis have been shown to correlate with the stiffness of the liver parenchyma (liver stiffness (LS)) [56], a property of tissue that can be determined by applying a force to the liver and measuring the deformity caused by that force, i.e. the elasticity of the liver parenchyma [57]. The most wide-spread way of measuring tissue elasticity is by transient elastography, or FibroScan (Echosens, France). FibroScan employs an ultrasound transducer at 5 MHz attached to a vibrator, which generates mechanical waves of 50 Hz with an amplitude of 2 mm [56]. The 50 Hz vibrations propagate through

the liver parenchyma as elastic shear waves and their speed is proportional with the liver stiffness. This speed is measured using pulse-echo ultrasound and is transformed into a Young modulus in units of kPa.

FibroScan readings showed good area under receiver-operator characteristic curves (AUROC) for METAVIR fibrosis score groups F≥2, F ≥ 3 and F=4 in patients with hepatitis B [58] and hepatitis C [59]. In patients with NAFLD, a study has shown that AUROCs were 0.93 for F ≥ 3 and 0.95 for F=4 [60], significantly higher then AUROCs for blood biomarkers.

There are a number of limitations of FibroScan examinations: they are not guided by US, therefore making it difficult to make sure that readings are made over the liver. Transient elastography also has a higher failure rate than MRI-based methods [61]. FibroScan can not be performed in patients with ascites, it is difficult in obese patients and it is operator dependent [62]. In addition to the shortcomings of transient elastography, liver stiffness measurements can be influenced by acute liver injury [63], acute increase in aminotransferase levels [64], beta-blockers [65] and nutrition [66], which in turn result in the misinterpretation of fibrosis grade.

3.2.3 Computed tomography

Computed tomography (CT) can be used for assessing the level of steatosis and fibrosis of the liver, measuring the volume of the liver, as well as to image the biliary tree. Assessment of steatosis can be performed either by considering the attenuation of the liver parenchyma (in Hounsfield units - HU_{liver}) or the liver-spleen attenuation difference ($CT_{L\text{-}S}$). Since fat has a lower attenuation value than soft tissue, it will reduce the overall attenuation of a steatotic liver. HU_{liver} has shown good correlation with histologic steatosis grade [67], however is

subject to inter-vendor variation. Instead of HU_{liver}, $CT_{L\text{-}S}$ is often used, which correlates well with moderate to severe steatosis (sensitivity 82%, specificity 100% [68]), but not as well with mild steatosis [29,69]. In addition to fat, HU_{liver} can be influenced by other factors, such as iron and certain drugs [67,70], neither of which can be differentiated using conventional or dual-energy CT. Blunt liver edge, nodular surface and morphological changes of the liver and parenchymal abnormalities were found to be suggestive of liver cirrhosis [71]. Based on these features, the diagnostic accuracy, sensitivity and specificity of CT images was found to be 67–86%, 77–84% and 53–68%, respectively [72]. When considering the ratio of the diameter of the hepatic vein and the caudate-to-right-lobe-ratio, liver fibrosis was possible to differentiate from normal liver with a sensitivity and specificity of 83% and 76% [73].

The major limitation of CT imaging is the x-ray radiation that carries the small risk of developing fatal cancer of 1 in 2000 CT procedures [74]. CT imaging is rarely used to look for NAFLD or NASH, diagnosing steatosis, fibrosis or cirrhosis is usually an incidental finding on abdominal CT scans performed for other reasons [75].

3.3 Quantitative characterisation of the liver using MR techniques

3.3.1 Magnetic resonance elastography

Magnetic resonance elastography involves inducing acoustic vibrations in tissue and imaging the propagation of these vibrations to calculate the shear modulus of the tissue [76], which is suggestive of liver stiffness. Tissue displacement is first measured with a MR pulse sequence that employs a motion encoding gradient that enables the encoding of the propagation of shear waves in tissue into the phase of MR images. Tissue displacement is then transformed

into values of the shear modulus.

When applied to the liver, MRE has the potential to differentiate different stages of fibrosis, having 3.45 kPa as a cut-off value between normal and fibrotic/cirrhotic livers. A recent review has shown that AUROC values of MRE for the diagnosis of biopsy-confirmed $F \geq 1$, $F \geq 2$, $F \geq 3$ stages and cirrhosis were 0.84, 0.88, 0.93, 0.92 [77] in a mixed population presenting ALD, NAFLD, HBV and HCV. When only the NAFLD cohort was considered, AUROC values of 0.89, 0.90, 0.94 and 0.90 were found for the groups described above, with sensitivities of 0.78, 0.82, 0.89 and 0.90, and specificities of 0.83, 0.82, 0.84 and 0.76.

Although MRE has good diagnostic accuracy, it is still not widely available at all clinical MRI sites, and, therefore, another non-invasive imaging method capable of discriminating stages of fibrosis is needed.

3.3.2 Fat fraction measurements

Liver biopsy can provide a semi-quantitative staging of steatosis, a hallmark of both alcoholic- and non-alcoholic liver disease. However, this type of invasive assessment is not suitable for regular follow-ups and thus needs a suitable non-invasive substitute measurement that is capable of characterising fat fractions both below and above the clinically significant level of 5% [78,79]. MR spectroscopy- and imaging-based proton density fat fraction measurements reflect the relative abundance of protons belonging to fat and water moieties and have been shown to be related to chemical triglyceride content of the liver [80].

3.3.2.1 MRS PDFF

Over the past years MRS has become the gold standard method for non-invasive quantification of fat in the liver. It is most often carried out using a multiple-echo, T_2-corrected

STEAM or point-resolved spectroscopy (PRESS) measurement, as described and introduced by Hamilton et al. [81], but other implementations exist too [29], e.g. single-echo time acquisitions that use population-based T_2s of water and fat to perform T_2 correction. When T_1-, T_2- and spectral correction is carried out, the resulting fat fraction is called the proton density fat fraction, as it accounts for all the signal produced by fat, not only the most prominent fat peak at 3.4 ppm [29], and it is defined as the ratio of fat proton densities and the sum of fat and water proton densities. The accuracy of MRS-derived PDFF measurements was demonstrated by several studies using histological references [80, 82–84].

Despite its usefulness and excellent accuracy, MRS-based PDFF needs specialist knowledge and it is not readily available at all clinical MR sites. Additionally, an MRS experiment takes a long time to perform and only covers a small portion of the liver, making imaging a more attractive approach to measuring fat.

3.3.2.2 MRI PDFF

Imaging-based PDFF measurements not only allow the assessment of fat over the entire liver, but also make the follow-up of patient more reproducible. MRI PDFF is also superior to MRS PDFF because it allows the visualisation of inhomogeneously distributed fat. PDFF is normally determined from magnitude-only or complex multiple-echo SPGR imaging data that has been acquired with low flip angle and has been corrected for T_2^* decay and incorporates a six-peak spectral model of fat.

Excellent correlation with the gold standard MRS PDFF has been shown both in adults and children [85, 86], as well as agreement between MRI PDFF values acquired at the clinically relevant 3 T and 1.5 T field strengths [87].

MRI PDFF gained much popularity due to the ease of acquisition and its wide availability on clinical imaging systems, however, a recent study has brought attention to sources of

bias for this method [88]: noise bias; Gaussian decay in the slice direction; biexponential decay, suggesting different T_2^* values for fat and water, also described by Reeder et al. [89]; inter-subject variation of the fat spectrum; and water frequency shift due to changes in temperature and pH.

3.3.3 T_2 and T_2^* mapping

Due to its sensitivity to changes in the magnetic micro-environment of liver tissue via transverse relaxation mechanisms, MRI can be used as an excellent non-invasive tool to measure the amount of iron in the liver.

The imaging-based measurement of liver iron concentration using the T_2 relaxation time is being marketed as FerriScan (ResonanceHealth, Australia) and has quickly become the gold standard non-invasive iron measurement in the liver. It is based on a multiple-echo spin echo acquisition in free breathing and the collected imaging data is fitted to a bi-exponential model to derive liver T_2 measurements by taking the proton density-weighted mean of the slow and fast T_2 components [90, 91]. At 1.5 T a non-linear relationship between R_2 (=1/T_2) relaxation rates and biopsy-derived iron concentrations in mg Fe/g dry tissue was found, described by eq. 3.1, where R_2 is given in units of s^{-1} and the iron concentration [Fe] is given in units of mg Fe/g dry tissue.

$$R_2([Fe]) = 6.88 + 26.06[Fe]^{0.701} - 0.438[Fe]^{1.402} \tag{3.1}$$

A different study has shown that the relationship between liver R_2 values and iron concentrations scales linearly from 1.5 T to 3 T, yielding eq. 3.2 [92, 93].

$$R_2([Fe])_{3T} = 1.47R_2([Fe])_{1.5T} - 2.20 \tag{3.2}$$

T_2^* measurements can also be used to quantify liver iron concentration with the benefit of short acquisition times. Multiple-echo spoiled gradient echo (SPGR) images are usually

collected, keeping the shortest echo time under 1 ms [94, 95] to allow the quantification of very short T_2^* values, i.e. to be sensitive to very high iron concentrations. Acquired image data is usually fitted to a mono-exponential model, occasionally extended with a constant term to account for noise, but more complicated models designed to estimate T_2^* values independent of noise via signal truncation have been described [96]. Several studies have investigated the relationship between R_2^* (=1/T_2^*) and biopsy-derived iron concentration, and have suggested similar linear calibration curves [97, 98], while also describing similar relationships between R_2^* values measured at 1.5 T and 3 T [92, 99].

Measurements of liver iron concentration using MRI methods have been shown to be useful in the follow-up of transfusion-dependent thalassaemia and sickle cell disease patients (both adults [97] and children [100]) and haemochromatosis patients [101], covering a range of iron concentrations between 0.3 to 57.8 mg Fe/g dry tissue [16, 90].

While T_2-based HIC-measurements have been shown to be reproducible between multiple centres and scanner types [102] and also between acquisition parameter sets [97], T_2^*-based measurements are more variable. Good inter-scanner and inter-centre reproducibility was demonstrated in several studies [103, 104] and it has also been shown that calibration curves obtained using different T_2^* relaxometry methods can be transformed one into another [105].

Both T_2- and T_2^*-based HIC quantification has some disadvantages. Spin echo-based, free breathing acquisitions for T_2 relaxometry take a long time (typically between 5 and 15 minutes) and also introduce breathing artifacts, resulting in a long image registration process. Multiple-echo SPGR sequences result in images that are sensitive to fat and B_0 inhomogeneities in the liver, both of which problems can be addressed by using an IDEAL fat-water separation algorithm capable of offering both an T_2^*- and a B_0 field map.

3.3.4 T_1 mapping

Fast T_1 mapping methods have initially been developed for myocardial imaging, and has been proven to be useful in the characterisation of myocardial infarction, amyloidosis, Fabry's disease and diffuse fibrosis [10, 11]. Lately, T_1 mapping has been used to characterise fibro-inflammatory liver disease [12, 13] with the assumption that the T_1 of the liver will increase in the presence of water accumulation in swelling of the cells (inflammation) or in the presence of increased extracellular fluid volume (a result of fibrosis).

Both Banerjee et al. and Hoad et al. have found that T_1 measurements can be used to detect advanced fibrosis (AUROC = 0.81) [12] and cirrhosis (AUROC = 0.92) [12] and detecting any stage of fibrosis (AUROC = 0.94) [13] in a mixed population of patients who have had liver biopsy, irrespective of the T_1 measurement technique. Discrimination of individual fibrosis score groups was not possible in these studies. When a more restricted group of patients with suspected or confirmed diagnosis of NAFLD were assessed, T_1 was found to correlate with histologically-determined fibrosis scores (r = 0.51) and the AUROC for the diagnosis of cirrhosis was 0.85 [106]. When comparing T_1 readings with the steatosis, activity and fibrosis (SAF) score summarising histological lesions [107], the same study reported a correlation of r = 0.70.

T_1 measurements have also been shown to correlate well with invasive hepatic venous pressure gradient (HVPG) measurements [108]: portal hypertension translated into longer T_1 values and a correlation coefficient of r = 0.85 was reported. When liver T_1 measurements were combined with blood velocity measurements in the splenic artery, a better coefficient of correlation was achieved with HVPG measurements (r = 0.90).

T_1 mapping is, however, influenced by a number of physiological and measurement parameters, and magnetic properties of tissue. Most notably, the presence of iron affects

not only transverse relaxation times, but also T_1 values, both directly [15, 16] and via T_2 effects [109] when a MOLLI technique is employed. A liver model of fibrosis has been built that allows the reversal of the effects of iron on T_1 values measured with MOLLI techniques [14] using Bloch equation simulations of T_1 measurements in the ideal case of normal iron, at the estimated extracellular fluid volume present during the original measurement. This simulation results in an iron-corrected T_1 value (cT_1).

Women younger than 52 years old have been observed to have significantly higher liver iron-corrected T_1 values (cT_1 = 784 ms) than women older than 52 years old [110], suggesting that changes in pre-menopausal women's hormonal cycle might affect the fluid balance of their liver, thus leading to an increased T_1 measurement. These findings are further supported by the difference seen in cT_1 values in participants with higher inferior vena cava (IVC) and aorta (Ao) cross sectional area ratios [110], also suggesting that higher blood volume in the IVC, and, thus, an increased body hydration level is a predictor of longer cT_1 values. Richards et al. have shown that the T_1 of young male volunteers and pre-menopausal women (both groups' age $\leq$ 40 years) did not show significant difference, however the mean T_1 of pre-menopausal women on oral contraceptive pills and pre-menopausal women not on oral contraceptive pills was significantly different, women who were on the pill having longer T_1 values [111]. This study also looked at the difference between liver T_1 values measured during the week of menstruation and the mean of liver T_1 values over the other three weeks in pre-menopausal women not taking the pill, and found that there was no significant difference between the two T_1 values.

Robson et al. have investigated the effects of magnetisation transfer and T_2 on T_1 measurements performed with MOLLI techniques and the saturation recovery single shot acquisition (SASHA) [112] T_1 mapping method [109], which also employs bSSFP readouts. The authors have found that the longitudinal magnetisation resulting from both the MOLLI

and SASHA sequences was affected by considering exchange between a free and a bound pool of protons; the resulting T_1 values were more affected when using the MOLLI sequence, due to the propagation of the complex magnetisation history between consecutive imaging readouts. T_2 was only found to influence T_1 values measured by MOLLI — measured T_1 values were longer in the presence of longer T_2 values — but not with SASHA.

T_1 values determined with MOLLI sequences also suffer from the influence of local field inhomogeneities [113] due to the frequency-dependence of the bSSFP readout. It has been shown that over a range of ±100 Hz, the measured T_1 can have a variation of up to 8% from the baseline value measured on resonance.

The original MOLLI sequence was shown to be severely influenced by heart rate [30], with an average error of 9%. This dependence was greatly reduced in the shortened MOLLI sequence, leaving only a constant error of 4% in the underestimation of "real" T_1 values [31].

Despite the drawbacks and the number of influencing factors of fast T_1 mapping techniques (e.g. MOLLI, shMOLLI, SASHA), their common major advantage is that they are available on all three major MRI platforms (Siemens, Philips and GE). This makes them an attractive method to use in both clinical and research applications.

Technical details, challenges and limitations of T_1 mapping, and the shMOLLI method in particular are presented in chapters to follow.

3.4 SUMMARY

This chapter presented an overview of liver anatomy, physiology, and pathology, as well as the current state of the art regarding liver imaging techniques, pointing out both advantages and disadvantages of each method. The following chapters will explore in more detail the changes in liver physiology that influence liver T_1 measurements.

4

The influence of fat on liver MOLLI T_1 measurements

4.1 INTRODUCTION

The modified Look–Locker inversion recovery (MOLLI) [30] T_1 mapping sequence and variants of it have been gaining interest in cardiovascular MRI [11] and in liver imaging [13], as described in previous chapters. The T_1 maps provided by these sequences provide diagnostic information in the heart [114], correlate with liver fibrosis and inflammation [13] and predict liver disease outcome [115].

Since livers often show fatty infiltration, it is of interest to study the behaviour of MOLLI sequences in fatty livers. Fat is known to have a short T_1, and in regions of visceral fat the MOLLI sequence measures this short T_1 with high reproducibility [116]. Similarly, the MOLLI sequence also detects the long T_1 of the blood pool with high reproducibility [117]. Patients suffering from liver diseases have been shown to have hepatic lipid concentration

(HLC) values in the 2% to 44% range [84, 118, 119]; thus, in livers with large amounts of fat, simplified reasoning would predict that the measured R_1 (=1/T_1) relaxation rate would be the weighted sum of the R_1 of the fat and the R_1 of the hepatic tissue. The measured T_1 of the liver would thus be expected to be reduced in fatty livers, due to this partial volume effect. Phantom scans and previous work have demonstrated that T_1 decreases with increasing fat concentration when using conventional imaging methods, e.g., spin echo inversion recovery (SE-IR) [120].

MOLLI T_1 values have been shown to be influenced by fat and off-resonance frequencies at 1.5 T in the calf muscle [121] and the myocardium [122], and elevated MOLLI T_1 is often measured in patients with fatty livers [13] at 3 T, where bSSFP repetition times between 2.1 ms and 2.6 ms are commonly used [13, 123]. It is the T_1 of the water component which appears to be of diagnostic significance when using T_1 mapping in the liver [124], while the T_1 of the fat is constant [125] and not a predictor of disease. An important step towards the use of MOLLI T_1 to assess liver disease is the clarification and quantification of the extent to which the presence of fat can mask or exaggerate changes in MOLLI T_1 due to disease.

The aim of this chapter is, thus, to describe the effect of different fat concentrations and off-resonance frequencies on MOLLI T_1 maps at 3 T with a bSSFP TR = 2.3 ms and to explain the mechanisms for this behaviour.

4.2 THEORY

MOLLI is an ECG-gated inversion recovery T_1 mapping method. It uses several inversion pulses and acquires images synchronised to the cardiac cycle using a snapshot bSSFP [126] readout. Sections of readouts are then followed by pauses of a few heartbeats, allowing for full recovery of the longitudinal magnetization, followed by other blocks of inversion pulses

and readouts.

The bSSFP readout results in images that are sensitive to the off-resonance frequency of the protons being imaged (fig. 4.1) [127]. The chemical shift difference between water

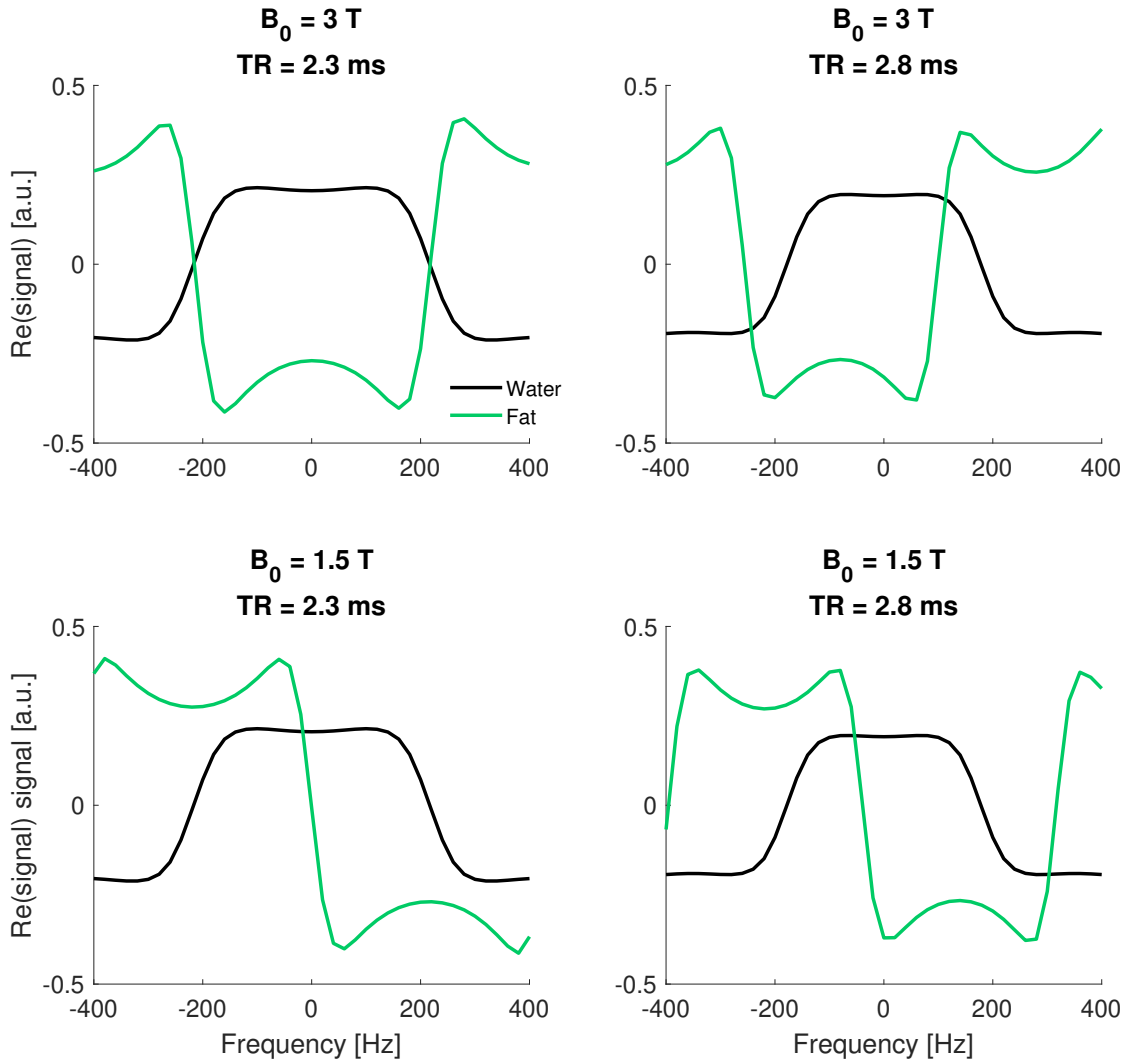

Figure 4.1: Off-resonance dependence of the bSSFP signal. Water and a single fat peak were simulated with T_{1water} = 900 ms, T_{2water} = 30 ms, T_{1fat} = 320 ms, T_{2fat} = 60 ms, δ_{fw} = 3.4 ppm, and $TE_{bSSFP} = TR_{bSSFP}/2$ for each simulation.

and the main fat peak is 3.4 ppm [33], which at 3 T translates into a frequency difference of $\delta_{\text{fat-water}}$ = 447 Hz. Therefore, if bSSFP images are acquired with a repetition time close to

$1/\delta_{\text{fat-water}}$ = 2.23 ms and an echo time equal to half of the repetition time, the fat and water signals will have exactly opposite phase. When a different TR is chosen, the amount of overlap between the bSSFP pass-bands of the fat and water signals will change, leading to a more complex function of off-resonance frequency of the combined signal. An asymmetric echo (i.e. TE < TR/2) is often used for bSSFP readouts. In such cases the phase relationship between the water and fat signals will not be as straightforward as in the case of symmetric echoes. Figure 4.2 illustrates three cases associated with different echo times leading to different phase angles between the water peak and the methylene fat peak situated at 1.3 ppm. However, in reality, fat comprises six different resonant peaks, meaning that the fat-water phase relationships are never as simple as those shown on fig. 4.2.

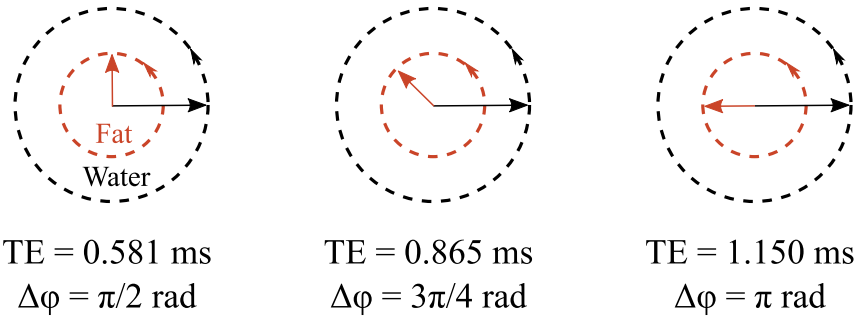

Figure 4.2: The phase relationship between fat at 1.3 ppm and water is determined by the chosen echo time. These phase relationships are valid for simulations at 3 T with TR = 2.3 ms. $\Delta\varphi$ denotes the phase difference between the water and fat peaks.

The signal in a voxel containing both fat and water with no exchange of magnetization between them would be determined by the partial volume effect. If the fat and water were in phase, the recovery would follow the sum of these two recovering exponentials. In practice, if this signal were fit to a single exponential then the measured T_1 would lie between the individual T_1s of the fat and the water. However, when using bSSFP readouts, the water and fat are exactly out of phase for TE = TR/2, and so the signal recovery is the difference of two exponentials weighted by the relative contributions of fat and water. When TE <

TR/2, the resulting signal is a complex sum of the water and fat signals, and ultimately also results in a non-mono-exponential recovery curve. In practical terms, for physiological concentrations of fat, the behaviour described above results in a measured value for T_1 that is longer than the T_1 of either the fat or water component [128]. A conceptual schematic of this behaviour is illustrated in fig. 4.3.

4.3 MATERIALS AND METHODS

4.3.1 Simulations

A Bloch equation [129] simulation was built in MATLAB (MathWorks, Natick, MA) which emulated the exact pulse sequence of a MOLLI acquisition on a Siemens Verio 3 T (Siemens Healthcare, Erlangen, Germany) scanner. The simulated sequence included the waveforms of RF inversion and imaging pulses. The measured signal intensity for each simulation was determined as the signal from a single voxel averaged over a number of phase encode lines symmetrically centered on k = 25. Magnetization transfer effects were not included in the simulation, although they are known to bias T_1 when using the MOLLI method [109].

A single inversion followed by five image readouts was simulated, providing a good approximation to the MOLLI acquisition but eliminating the complexity that is due to the multitude of possible sampling schemes that have been described [109]. Since liver MOLLI T_1 values lie in the 700–1400 ms interval [13], five samples over the recovery curve were enough for determining T_1, as the samples can capture the dynamics of the recovery curve.

Simulation parameters were as follows: 3 T field strength, 192 × 144 matrix, 84 phase encode lines, 24 phase encode lines before the central line, $FA_{readout} = 35°$, TR/TE = 2.3/0.581–1.15 ms, TI = 100, 1000, 1900, 2800, 3700 ms, adiabatic hyperbolic secant 1 inversion pulse of

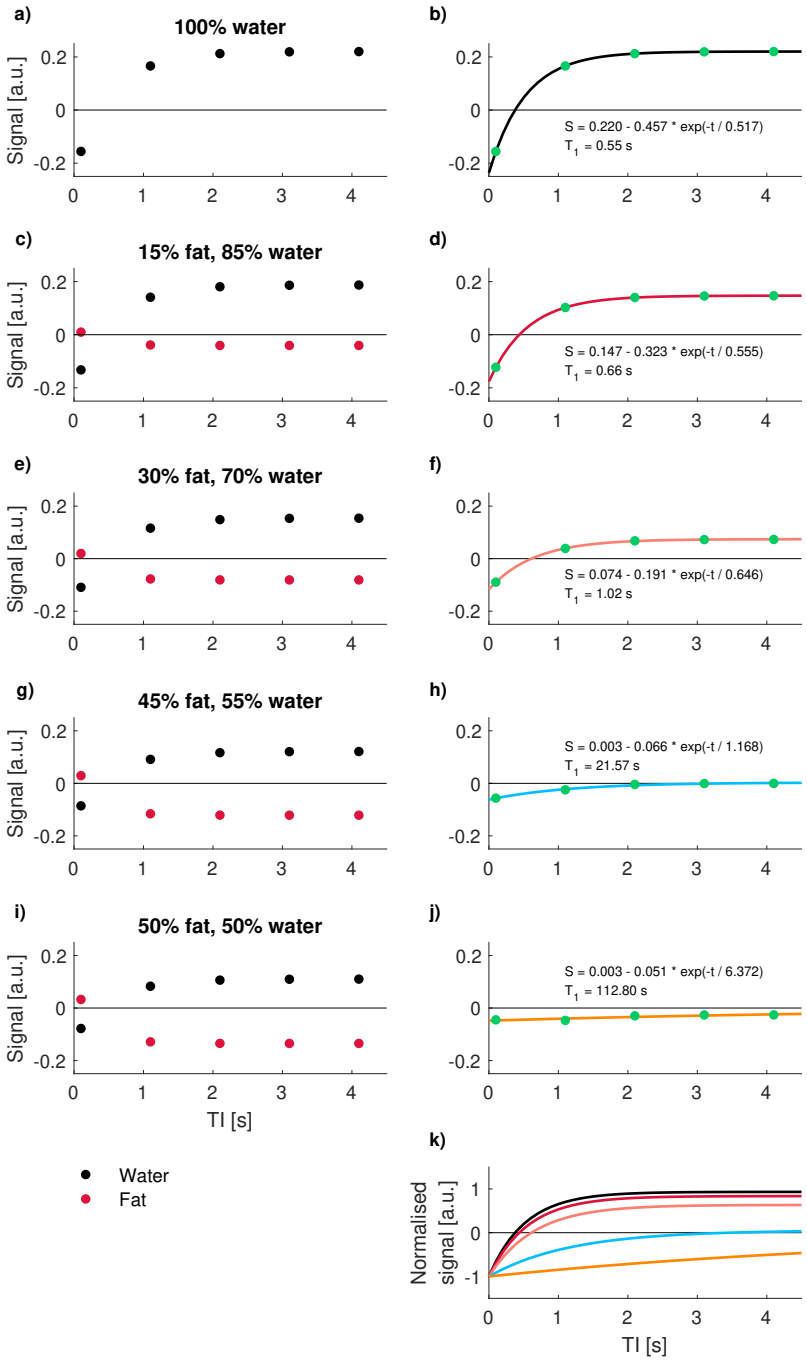

Figure 4.3: Lengthening of (sh)MOLLI T_1 value with increasing fat fractions. Subfigure pairs a-b, c-d, e-f, g-h, and i-j contain sampled simulated fat and water signals and their combination in different proportions. To emphasise the progressively longer T_1 values fitted to the resulting combined signals, subfigure k contains all five fitted curves normalised to the signal value at TI = 0 ms. Simulation parameters were: T_{1w} = 700 ms, T_{2w} = 30 ms, T_{1f} = 320 ms, T_{2f} = 60 ms, TR_{bSSFP} = 2.3 ms, TE_{bSSFP} = 1.15 ms

10.24 ms duration, time-bandwidth product R = 5.48, peak B_1 = 750 Hz and β = 3.45 [109]. The bSSFP readout used five linearly increasing start-up angle (LISA) pulses [26,27] and one half-angle ramp down pulse. The interval of echo times was chosen to reflect a range of fat-water phases between $\pi/4$ (where fat and water signals are perpendicular, and, theoretically are corresponding to the real and the imaginary part of the composite fat-water signal, making them easily separable) and π (where the fat and water signals are collinear).

T_1 and T_2 values for fat and liver components were: T_{1fat} = 382 ms, T_{2fat}=68 ms [130], $T_{1hepatic}$ = 812 ms [131], $T_{2hepatic}$=34 ms [130]. Separate complex signals corresponding to each component of a multiple-peak lipid spectrum were weighted by their relative amplitude provided by Hamilton et al. [81] and summed to obtain a single complex fat signal. Simulated complex fat and water signals were combined in different proportions according to the principle of partial volumes to reflect HLC in the 0–100% range in steps of 1%. Fat fractions, F, were defined using eq. 4.1, where ρ_f and ρ_w denote the proton densities of fat and water.

$$F = \frac{\rho_f}{\rho_f + \rho_w} \times 100[\%] \tag{4.1}$$

The signal points were then fitted to a mono-exponential describing longitudinal recovery, given by eq. 4.2, where T_1^* is the apparent T_1 and A and B are additional fit parameters.

$$S(TI) = A - Be^{-\frac{TI}{T_1^*}} \tag{4.2}$$

The MOLLI T_1 values were computed by using the imperfect [32], but commonly used, Look–Locker correction method described by eq. 4.3 [30].

$$T_1 = T_1^* \left(\frac{B}{A} - 1 \right) \tag{4.3}$$

To show the changes in MOLLI T_1 caused by repetition times other than 2.3 ms, the variation with off-resonance frequency was simulated for two repetition times found in the literature:

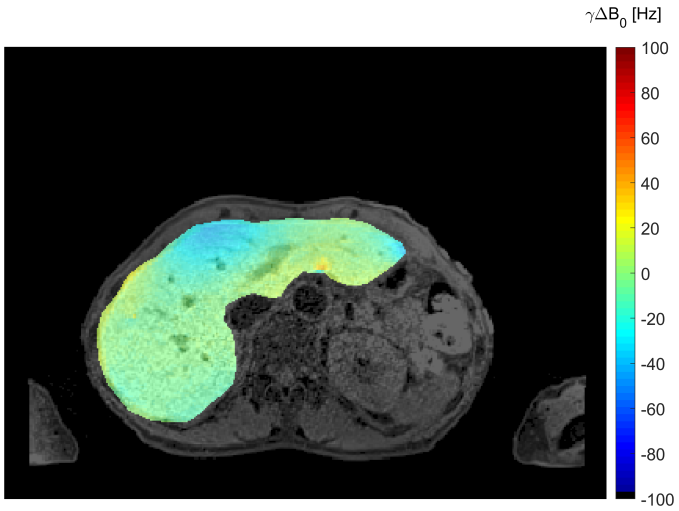

Figure 4.4: A typical example of static field inhomogeneity map collected over the abdomen at 3 T.

TR = 2.14 ms [13] and TR = 2.6 ms [123], each for TE = TR/2. All simulation parameters were the same as described above for the liver simulation, with the simplification that only three lipid concentrations were simulated: 0%, 10%, and 20% as these are representative of the healthy and the mild-to-sever NAFLD population. The chosen off-resonance frequency range was –100 Hz to 100 Hz in steps of 2 Hz, which covers the typical frequency range encountered in abdominal imaging experiments. Figure 4.4 shows an example of an abdominal B_0 field map. Shimming in all cases was performed automatically by the scanner over a 30 mm thick rectangular adjustment volume covering the liver.

To further explore the effects of fat on MOLLI T_1 values, the bSSFP TR was varied in a simulation comprising a water and a multiple-peak fat component with 30% fat fraction. The spectral model of the fat was based on the ^{1}H spectrum of the margarine phantom described below. The same imaging protocol was simulated as described in the previous section, with the following differences: TI = 200, 1200, 2200, 3200, 4200 ms, RR = 1000 ms, and 31 bSSFP TR values between 1.93 ms and 5.75 ms were used. T_1 and T_2 values for fat and water components corresponded to those of a margarine phantom and were T_{1fat} = 325

ms, T_{2fat} = 120 ms, T_{1water} = 2448 ms, and T_{2water} = 207 ms. The measurements leading to these values are described in the next section.

4.3.2 Phantom Scans

Phantom experiments were carried out using a margarine phantom (Flora Light, Unilever) with 30% fat content and all scans were performed on a Siemens Verio 3 T (Siemens Healthcare, Erlangen, Germany) scanner. The margarine phantom was first scanned using a 5-point MOLLI sequence. Imaging parameters followed a standardised MOLLI acquisition protocol (Siemens WIP 561a, Erlangen, Germany): 192 × 144 matrix, FA = 35°, TR/TE = 2.3/0.99 ms, TI = 100, 1100, 2100, 3100, 4100 ms, simulated ECG with RR = 1000 ms. The same margarine phantom was then scanned using the SE-IR sequence with the following sequence parameters: 128 × 128 matrix, TR/TE = 10000/7.4 ms, and TI = 50, 150, 250, 400, 600, 900, 1300, 2000, 3000, 4500, 6500 ms. In both cases images were acquired on a Siemens 3 T Verio scanner, using a 32-channel head RF coil.

Following the margarine scans, a sample of the margarine was heated and spun with a centrifuge (Rotanta 460R, Hettich) at 4000 rpm for 5 minutes. After spinning the sample, separate layers of fat and water were obtained and were scanned using both the MOLLI and the SE-IR acquisition, using the same scanner and same the protocols as described above.

A subsequent experiment was carried out to determine MOLLI T_1 of the whole margarine and the water component over a range of repetition times. The previously described 5-point MOLLI acquisition protocol was used with the following changes: TI = 200, 1200, 2200, 3200, 4200 ms, RR = 1000 ms, and 31 bSSFP TR values ranging from 1.93 ms to 5.75 ms.

MOLLI T_1 values were determined by fitting the signal intensity of a circular region of

interest on the bSSFP images following the inversion pulse to eq. 4.2, then applying eq. 4.3 to obtain T_1. T_1 values for images acquired using the SE-IR sequence were computed by fitting eq. 4.4 to mean signal values sampled from the same region of interest in each image.

$$S(TI) = C(1 - 2e^{-TI/T_1} + e^{-TR/T_1}) \tag{4.4}$$

4.3.3 *Patient Studies*

In order to compare the results of the simulations to results obtained in vivo, data from eight patients (seven female, mean age: 49 ± 10.5 years) were analysed retrospectively. Patients were scanned before weight reduction surgery and 6 months post-operatively. Relevant parameters of the patients before surgery included mean body-mass index (BMI): 45.8 ± 5.5 kg/m², mean waist circumference: 120.25 ± 10.35 cm, and mean hip circumference: 134.5 ± 11.2 cm. Four of the patients suffered from diabetes. Post-operative parameters were: mean BMI: 36.4 ± 4.8 kg/m², mean waist circumference: 107.7 ± 10.6 cm, and mean hip circumference: 120.6 ± 8.6 cm.

The study protocol conformed to the ethical guidelines of the 1975 Declaration of Helsinki, and was approved by the institutional research departments and the National Research Ethics Service (13/SC/0243). All patients gave written informed consent prior to enrolment in the study.

At each time point, patients had liver MOLLI T_1 maps (5-point MOLLI was employed as it captured the relatively short T_1 of the liver and to have consistency with simulations and phantom experiments). T_2^* maps were collected for hepatic iron quantification and ^{1}H MRS for the quantification of HLC using the STEAM sequence. Imaging parameters for the MOLLI scan were: 192 × 134–160 matrix (depending on patient), field of view (FOV) 280–348 × 350–500 mm (depending on patient), slice thickness of 8 mm, generalised

autocalibrating partial parallel acquisition (GRAPPA) acceleration factor 2, pixel bandwidth 898 Hz/px, TR/TE = 2.14/1.07 ms, FA = 35°, TI = 110, 110+RR, 110+2RR, 110+3RR, 110+4RR ms. MOLLI T_1 maps were acquired in the transverse scan plane.

T_2^* maps were determined using a multiple echo SPGR acquisition. Imaging parameters for this acquisition were as follows: same FOV as for the 5-point MOLLI sequence, 192 × 128–160 matrix (depending on patient), slice thickness of 3 mm, GRAPPA acceleration factor 2, TR/TE = 26.5/2.46, 7.38, 12.30, 17.22, 22.14 ms, FA = 20°. Fat saturation and double-inversion black blood preparation were employed.

The STEAM spectroscopy experiment used [132]: TE = 10 ms, TM = 7 ms, TR = 2000 ms for water-suppressed spectra and TR = 4000 ms for non-water-suppressed spectra and voxel volume was 8 cm^3. The voxel of interest was placed in the lateral part of the right lobe of the liver, avoiding vessels, bile ducts, and the edge of the liver. Spectra were processed using AMARES in jMRUI [133] with a specialized MATLAB script [132] and HLC determined as the ratio of the fat signal and the sum of the fat and water signals as in eq. 4.1.

Three curves showing the evolution of T_1 as a function of HLC were also simulated, each with a T_1 at 0% HLC equal to the mean T_1s reported by Banerjee et al. [13] for Ishak fibrosis stage groups 0, 1-2 and 5-6. Simulation parameters were the same as described in section 4.3.1.

4.4 RESULTS

4.4.1 Simulation

Figure 4.5 shows a map reflecting the change of MOLLI T_1 with the variation of echo time and fat fraction. It is apparent that depending on the echo time, T_1 either decreases with

fat fraction monotonically (for TE $\lessapprox$ 0.75 ms), or has a non-monotonic relationship with fat fractions (TE $\gtrapprox$ 0.75 ms). Figure 4.6 presents the evolution of MOLLI T_1 over the entire simulated range of fat fractions at four different echo times. When using echo times close to half the repetition time, the increase in T_1 is quadratic for fat fractions in the 0–16% range and at TE = TR/2 = 1.15 ms this trend can be approximated by eq. 4.5, where MOLLI T_1 is expressed in milliseconds and F is the percent HLC. The root mean square error of this approximation was: 1.3 ms.

$$MOLLIT_1 = 715 + 5.47F + 0.27F^2 \tag{4.5}$$

The increasing trend stops at approximately F = 40%, where fitting becomes impossible owing to the water signal and fat signal canceling each other. For F > 50% MOLLI T_1 values change rapidly, eventually reaching the T_1 of the fat at F = 100%. The increase of MOLLI T_1 is explained by the simultaneous increase of both the B/A ratio and the apparent T_1 (T_1^*) in eq. 4.3.

Figure 4.7 shows the behavior of MOLLI T_1 variation with off-resonance frequencies in the quadratic range of fat dependence. Although the bSSFP readout leads to a symmetric MOLLI T_1 variation around the central water frequency for 0% HLC, the presence of fat transforms this relationship into an asymmetric dependence, e.g. the composite fat-water T_1 value corresponding to 50 Hz off-resonance is longer than that corresponding to -50 Hz off-resonance.

The simulated dependence of MOLLI T_1 on off-resonance frequency when using repetition times from the literature [13, 123] is shown in fig. 4.8. MOLLI T_1 values were found to be higher at shorter repetition times for most fat fractions and off-resonance frequencies. Additionally, the MOLLI T_1–off-resonance frequency dependence is both larger and increasingly asymmetric with respect to frequency in the presence of higher amounts of fat.

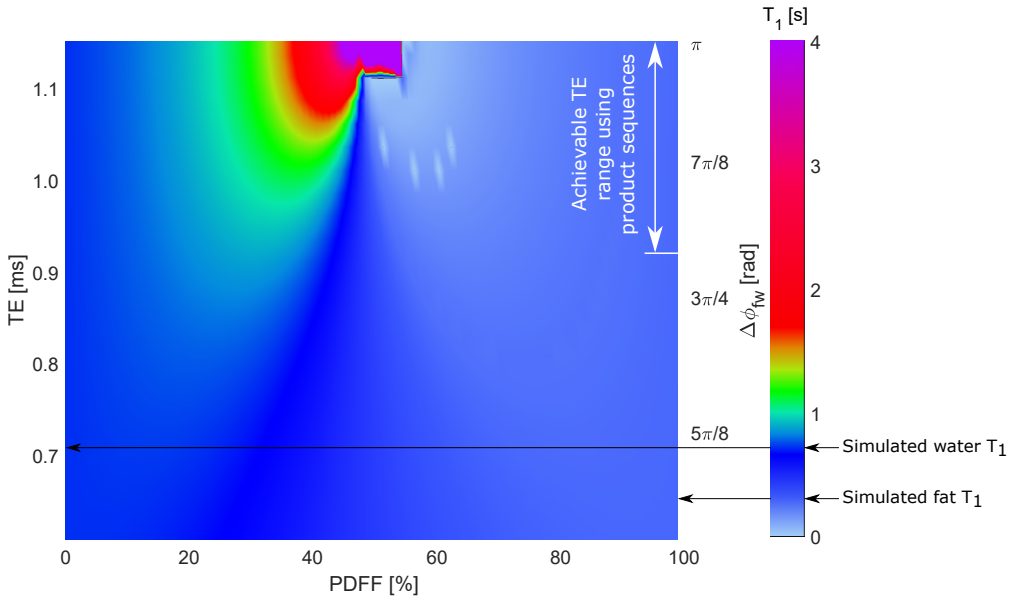

Figure 4.5: (sh)MOLLI T_1 as a function of fat fractions and echo times at a fixed TR = 2.3 ms. T_1 of water (812 ms) is reached at PDFF = 0% and T_1 of fat (382 ms) is reached at PDFF = 100% for all echo times.

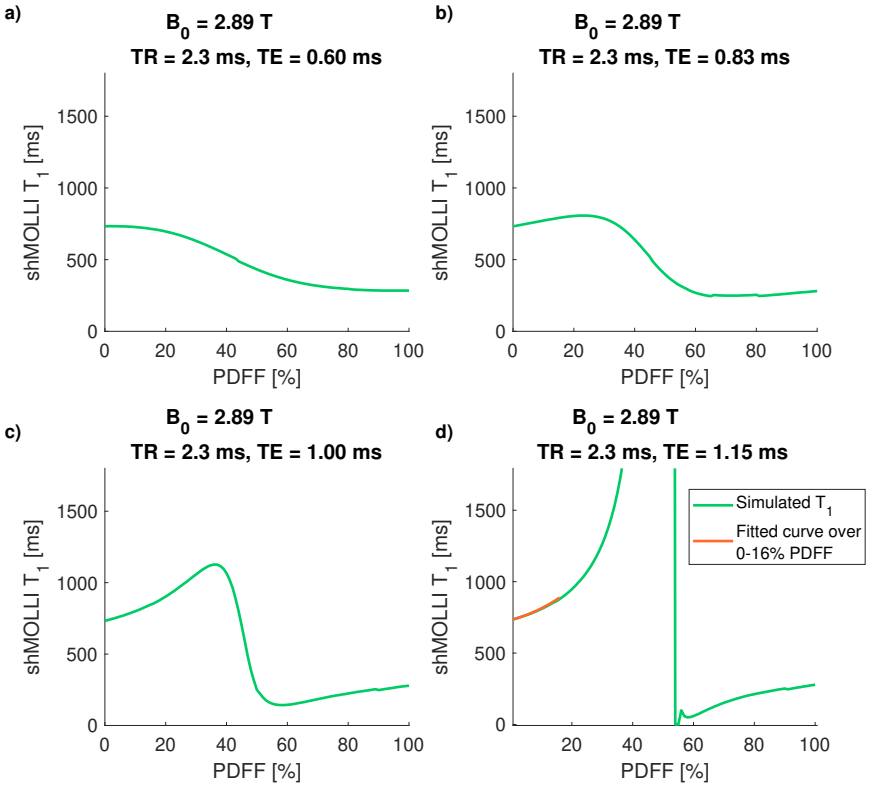

Figure 4.6: Evolution of (sh)MOLLI T_1 values over fat fractions at TR = 2.3 ms and four echo times. Subfigure d) also presents an analytical approximation of this T_1 evolution over the 0–16% fat fraction interval, as given by eq. 4.5.

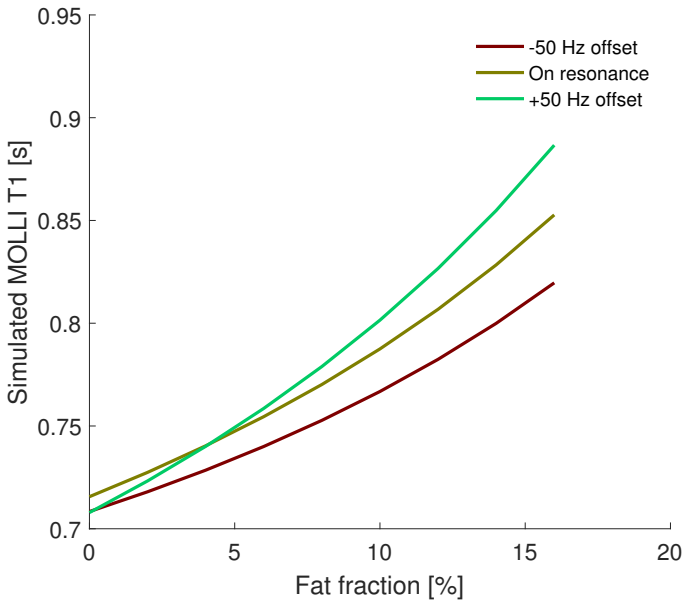

Figure 4.7: Off-resonance behaviour of (sh)MOLLI T_1 in the presence of fat (TR = 2.3 ms, TE = 1.15 ms).

4.4.2 *Phantom Scans*

T_1 values determined from MOLLI and SE-IR experiments in the margarine phantom are presented in table 4.1. As expected, MOLLI T_1 values underestimated those determined with the SE-IR experiment in both the water and fat components [31], however, the MOLLI T_1 of the margarine phantom was longer than the T_1 of the water component, as opposed to the SE-IR T_1, which was shorter then the T_1 of the water component, in accordance with simulations. Figure 4.9 shows the signal intensities taken from regions of interest on SE-IR

Table 4.1: T_1 values measured by the MOLLI method and computed from SE-IR images. *p-value obtained using an equal variance two-sample t-test, †p-value obtained using an unequal variance two-sample t-test

Phantom type	MOLLI T_1 [ms]	SE-IR T_1 [ms]	p-value
Fat component	291 ± 23	325 ± 20	$< 10^{-3*}$
Water component	2266 ± 21	2448 ± 7	$< 10^{-3*}$
Whole margarine	3874 ± 177	1313 ± 14	$< 10^{-3\dagger}$

images and the curves fitted to these points, along with the signal intensities sampled from

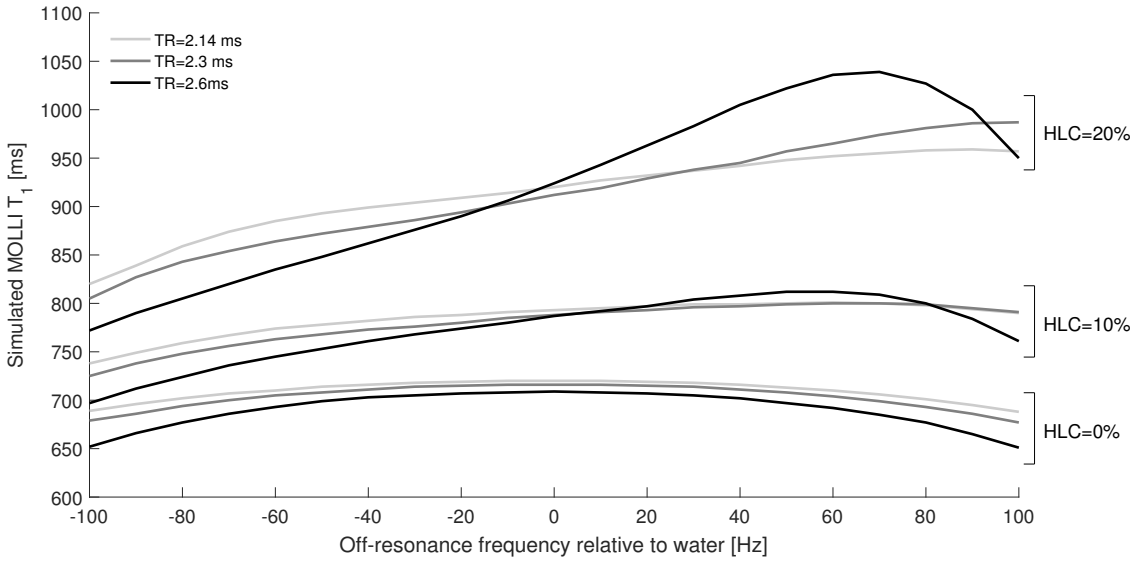

Figure 4.8: Dependence of (sh)MOLLI T_1 on off-resonance effects. The effect of off-resonance frequency becomes stronger at higher fat fractions.

MOLLI acquisitions and corresponding fitted curves. The results of the simulation and

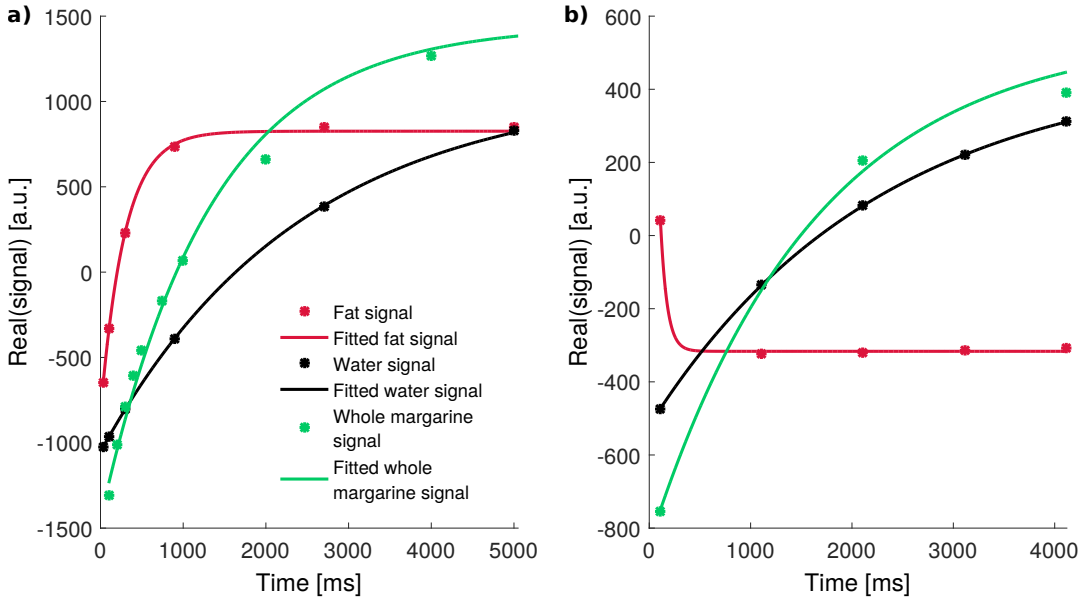

Figure 4.9: SE-IR (a) and MOLLI (b) recovery curves for the margarine phantom

phantom experiment exploring the dependence of MOLLI T_1 on repetition times is shown in fig. 4.10. Both simulated and measured MOLLI T_1 values of the margarine phantom

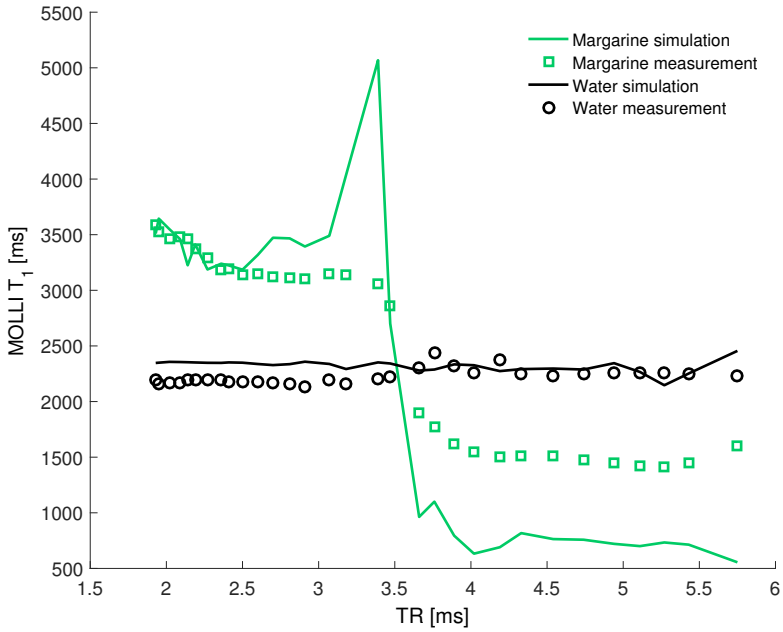

Figure 4.10: Dependence of simulated and measured (sh)MOLLI T_1 on the bSSFP repetition time

with 30% fat were higher than those of water over the 1.8–3.5 ms range and lower over the 3.5–5.75 ms range due to the relative position of the bSSFP profiles of the fat and water when employing symmetric echoes. However, the simulated and measured data did not agree perfectly. A possible explanation for the mismatch could be the missing information on the different T_1 and T_2 values of the individual fat peaks in the margarine phantom or that simulations were performed using symmetric echoes while measurements employed asymmetric ones. A similar difference between simulation and phantom experiments can be seen in the work of Thiesson et al [121].

4.4.3 *Patient Studies*

One patient was excluded from the comparison because the T_1 fit to the MOLLI data failed at the first visit. The measured HLC for this patient was 39.7%, which is in the regime where the Bloch simulated data could also not be fitted to an inversion recovery model.

Six patients had normal T_2^* values larger than 19 ms and one had T_2^* = 15 ms, indicating elevated iron but all within the normal range for T_2^* at 3 T [99].

Pre- and post-operative MOLLI T_1 measurements for seven patients are shown in fig. 4.11, plotted as a function of their spectroscopically measured HLC. Simulated relationships

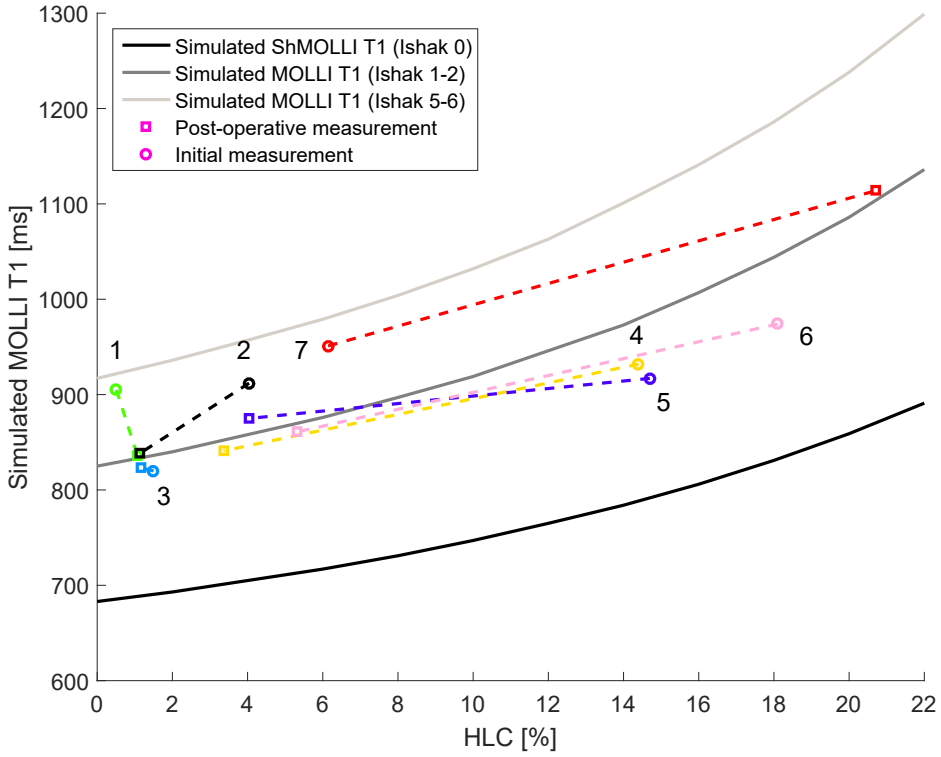

Figure 4.11: Evolution of patient (sh)MOLLI T_1 and fat fraction before and after weight reduction surgery

between T_1 and HLC are also included for three different levels of liver fibrosis, characterized by the Ishak score [48]. MOLLI T_1 values at 0% HLC for the three curves were taken from Banerjee et al, as shown in their fig. 2 of ref. [13]. The changes in MOLLI T_1 that occur in these patients are consistent with the hypothesis that the water in the livers of these patients is elevated but stable between exams and that the fat concentration has changed. These patients are expected to have some level of inflammation or fibrosis, which has previously been shown to elevate MOLLI T_1 [13].

4.5 DISCUSSION

In this chapter I have shown that MOLLI T_1 at 3 T has a complex dependence on fat and it increases with fat concentration in simulation and phantoms, when using typical sequence parameters (TR = 2.3 ms and echo times close to half of the TR), in a physiological range of 0–45% HLC. These observations also apply when the bSSFP TR lies in the 2.1–2.6 ms range. The MOLLI T_1 elevation is seen in vivo with the caveat that there may be other changes in the livers of the patients over 6 months after bariatric surgery that would be expected to modify the T_1 [13].

Due to a chemical shift difference of 447 Hz between fat and water at 3 T, the two tissue components are exactly out of phase with their pass-bands overlapping when using TR = 2.3 ms and TE ≈ TR/2. Thus, combined signals from tissue containing fat and water are less dependent on off-resonance frequency than reported previously using TR = 2.7 ms at 1.5 T [121]. While it might be tempting to use TR > 4 ms in vivo to have T_1 values of fat-water mixtures shorter than the T_1 of water alone, increasing or decreasing the TR from 2.3 ms at 3 T reduces the overlap of the two bSSFP pass-bands, increasing the off-resonance frequency dependence.

These simulations suggest that careful shimming, in addition to the use of a TR of 2.3 ms or less, is useful to maximize the consistency of MOLLI T_1 measurements within a single subject and between subjects.

In contrast to 3 T, where the optimal TR for reducing the frequency dependence of MOLLI T_1 measurements is close to the minimum TR available with existing hardware, at 1.5 T longer TR values would have to be used to produce a similar overlapping of the two bSSFP pass-bands due to the smaller chemical shift difference between fat and water.

Patient MOLLI T_1 evolution over a 6-month interval after bariatric surgery follows the

model describing the influence of fat on MOLLI T_1 values. It is expected that, while the amount of fat changes in these patients, other parameters known to affect the T_1 (such as fibrosis and inflammation) remain fairly constant. In general terms, the change in measured MOLLI T_1 is consistent with the behaviour that is predicted by the simulation for changes in liver fat in five of the seven patients; in patient 3 the change in liver fat was very small and the MOLLI T_1 change was small, and in patient 1 the liver fat change was small, but the MOLLI T_1 change was ~100 ms, not following the model. We believe that this supports the applicability of the model in vivo.

A limitation of this study is the small size of the patient cohort. A change in MOLLI T_1 in two of the patients (1 and 3) was not explained by change in fat fractions, suggesting the existence of other mechanisms responsible for having an influence on hepatic MOLLI T_1 values, perhaps a change in the fibrosis stage.

The MOLLI T_1 mapping method is used extensively in cardiac imaging and so it is important to briefly consider the effect of myocardial fat on MOLLI T_1 maps at 3 T. Since global lipid fractions in the myocardium are in the 0.2% to 2% interval [132, 134], they have a much smaller effect on measured MOLLI T_1 values. Focal lipid accumulations constitute an exception. In such cases fat infiltration can be as high as 35%, e.g. in the case of lipomatous metaplasia [122], leading to replacement of scar tissue with lipid accumulations after myocardial infarction. Effects of these focal lipid concentrations are described in more detail by Kellman et al. [122].

4.6 CONCLUSIONS

This study has shown that the presence of fat influences MOLLI T_1 measurements in the liver. This effect is in addition to the previously known effects of T_2, magnetization transfer,

off-resonance frequency, and increased iron concentration. Simulation has shown that fat fractions up to 40% will have an additive effect on the measured MOLLI T_1 value at 3 T when using a bSSFP readout with TR = 2.3 ms and a symmetric or near symmetric bSSFP echo. This behavior has been confirmed in the livers of patients undergoing weight-reduction surgery.

The influence of fat should be considered in the assessment of hepatic diseases using MOLLI T_1 measurements, as fat fraction values measured in the liver can be large enough to cause severe MOLLI T_1 alterations and shadow the presence of fibro-inflammatory liver disease.

5

Determining water shMOLLI T_1 in fatty livers

5.1 INTRODUCTION

The signal produced by bSSFP is dependent on the T_1 and T_2 of imaged proton species, flip angle, and off-resonance frequency [126]. As shown in the previous chapter, the frequency dependence, in particular, can result in complex behaviour of the bSSFP signal during T_1 recovery when the imaged voxels contain both fat and water [17, 121, 122]. With typical imaging parameters and clinically relevant fat fraction, this leads to the counter-intuitive overestimation of the liver water MOLLI T_1. This effect is in addition to the effect of iron deposits that reduce T_1 and T_2 [15, 135]. Magnetisation transfer [109], heart rate [31], repetition time of the bSSFP readout [17] and B_0 inhomogeneity [17] also influence MOLLI T_1 values. Removing the effect of iron on MOLLI T_1 has previously been demonstrated [14], but to best characterise fibro-inflammatory disease, off-resonance effects need to be removed,

both B_0-related and chemical shift-related, to produce an on-resonance water MOLLI T_1. A disease where this might prove to be important is NAFLD, a condition characterised by hepatic lipid accumulation [2]. NAFLD has a worldwide prevalence of 20-30% [7, 8] and encompasses a range of pathology from non-alcoholic steatosis (simple fat accumulation) to NASH (fat accumulation associated with liver inflammation), to cirrhosis. In some cases, hepatocellular carcinoma may develop [41, 136]. Since both the presence of fat and fibro-inflammation causes MOLLI T_1 values to increase at 3 T when using TR $\approx$ 2.3 ms, differentiating these two processes may provide additional insight into the disease and its progression.

This chapter explores whether the confounding effect of lipids and off-resonance frequency can be, in addition to the previous correction for the effect of iron, taken into account to provide a MOLLI T_1 independent of the influence of these factors. Therefore, the target is a water MOLLI T_1 value that would have been measured if a subject had no fat, normal iron, and imaging had been done on resonance.

5.2 METHODS

To determine a water-only shMOLLI T_1 value, an algorithm based on comparing simulated and measured bSSFP signals was developed with the aim of matching the best simulated signal to measurements to ultimately extract a signal unaffected by iron, fat and off-resonance frequency from a predefined model of the liver parenchyma. The algorithm was first validated in phantoms and subsequently tested in patients.

5.2.1 *Phantom experiments*

5.2.1.1 *Construction*

Fifteen agar-based phantoms were built with varying proportions of fat and water. Phantoms were stored in 30 ml plastic sample containers (King Scientific, UK) and were built in three batches, using a recipe similar to that described by Hines et al. [137]. To vary the T_1 of water in each of the batches, $NiCl_2$ (Sigma-Aldrich, St. Louis, MO, USA) solutions with concentrations of 0.45 mM, 0.73 mM, and 1.61 mM were used. Next, 2%/weight agar (Sigma-Aldrich), 0.01%/weight sodium benzoate (Sigma-Aldrich), 43 mM sodium chloride (Sigma-Aldrich), and 43 mM sodium dodecyl sulfate (Sigma-Aldrich) were added. Each of the three solutions was boiled until it became transparent and viscous. Five sample containers were prepared for each batch, having 0%, 5%, 10%, 20%, and 30% volume of peanut oil (Tesco, UK). Each container was filled to 30 ml with water-agar solution. Each sample container was further homogenised for five minutes using an ultrasonic homogeniser (Eumax UD200SH, Hong Kong). The sodium dodecyl sulfate in the solution ensured that water and fat formed a homogeneous emulsion. A sixteenth sample container was filled with 100% peanut oil. Peanut oil was chosen due to its ^1H spectrum resembling the ^1H spectrum of human subcutaneous fat [138].

5.2.1.2 *Imaging*

Phantoms were scanned using a Siemens Tim Trio 3 T imager (Siemens Healthineers, Erlangen, Germany) equipped with a 6-channel body matrix coil (Siemens Healthineers, Erlangen, Germany) and a spine array coil (Siemens Healthineers, Erlangen, Germany) with 24 channels, of which 9 were used. A set of multiple-echo SPGR images were collected to compute a map of the main magnetic field variation ($\gamma \Delta B_0$). Parameters of the 2D multiple-

echo GRE sequence were: FA = 6°, TR/TE = 22.2/1.25, 2.46, 3.69, 4.92, 6.15, 7.38, 8.61, 9.84 ms, FOV 302 × 245 mm², acquisition matrix 128 × 104, phase encoding direction anterior-posterior, BW = 1180 Hz/px, bipolar gradient readout scheme and slice thickness 7 mm. The map of $\gamma\Delta B_0$ field variation was determined from a T_2^*-IDEAL fat-water separation method with field map estimation using a graph-cut algorithm [139, 140].

T_2 values of the fat-free phantoms were determined using a multiple contrast spin echo (MCSE) experiment to quantify the effect of the agar and $NiCl_2$ on transverse relaxation. The following sequence parameters were used: TR/TE = 9000/15–480 ms in steps of 15 ms, FOV 270 × 270 mm², matrix 128 × 110, slice thickness 8 mm. Images with different contrasts were fitted to eq. 5.1, where S is the measured signal and S_0 is the signal at TE = 0 ms:

$$S = S_0 e^{-TE/T_2} \tag{5.1}$$

A MOLLI variant, shMOLLI [31] was used to acquire a T_1 map by collecting images at 7 inversion times, over 9 simulated heart beats with 3 inversions, using the 5(1)1(1)1 scheme, i.e. the first inversion pulse was followed by five readouts and a pause with a duration of one RR interval, the second inversion pulse was followed by one readout and a pause with a duration of one RR interval and the third inversion pulse was followed by one readout. ShMOLLI parameters followed a standardised protocol (Siemens WIP 561a, Erlangen, Germany): readout FA = 35°, TR/TE = 2.52/1.05 ms, FOV 290 × 343 mm², matrix 192 × 182, phase encoding direction anterior-posterior, BW = 898 Hz/px, slice thickness 8 mm, 28 lines before the central line, 82 total k-space lines, shortest TI = 110 ms, inversion time increment 80 ms, GRAPPA [141] acceleration factor 2 with 24 reference lines, partial Fourier factor 6/8 in the phase encoding direction and simulated heart rate of 60 beats/min. The approach to steady-state was accelerated using 5 LISA pulses [26, 27] and one half-angle ramp down pulse. T_1 values were obtained by applying the shMOLLI conditional fitting algorithm [31].

All images were acquired in a coronal slice.

5.2.1.3 Spectroscopy

A set of ^{1}H spectra with multiple TR and TE were collected using the multiple-TR, multiple-TE STEAM SVS sequence [125] to characterise the T_1 and T_2 values of six fat peaks in the pure peanut oil phantom. Relaxation time measurements of the pure peanut oil phantom were repeated at 20°C and 37°C. The multiple-TR, multiple-TE STEAM sequence followed the approach described by Hamilton et al. [125]: no water suppression, voxel size: 14 × 14 × 24 mm^3, TM = 9 ms, 24 spectra collected with TR varying between 150 and 2000 ms (150, 175, 200, 225, 250, 275, 300, 325, 350, 400, 450, 500, 600, 700, 800, 900, 1000, 1250, 1500, 2000 ms) and TE fixed at 15 ms, then 8 spectra collected with a fixed TR of 1000 ms and TE changing from 20 to 110 ms (20, 25, 30, 35, 50, 70, 90, 110 ms). A version of the sequence with multiple-TR but fixed TE = 15 ms was used to quantify individual T_1 values of water and fat peaks in the mixed water and oil phantoms. PDFF values were also determined from ^{1}H spectroscopy data. The obtained spectra were fitted using the MATLAB-adapted version of the AMARES algorithm [142, 143] and the resulting amplitudes for each peak were fitted to eq. 5.2, where S_{oi} is a scaling factor proportional to proton density, TE is the echo time, τ is the time from the third 90° pulse of the STEAM sequence to the end of the TR interval, i.e. the time during which the longitudinal magnetisation recovery occurs and i is an index for each spectral peak.

$$S_i = S_{oi}\left(1 - e^{-\tau/T_{1i}}\right) e^{-TE/T_{2i}} \tag{5.2}$$

When analysing multiple-TR only experiments, the T_{2i} were fixed to be those determined in the pure peanut oil phantom and the 0% fat phantom. PDFF was defined as the ratio of the sum of observed fat proton densities and the sum of proton densities of water and observed

fat peaks, as defined by eq. 5.3. Here S_{of_i} denotes the proton density of the ith fat peak and S_{ow} is the proton density of water. These values were determined from fitting spectroscopy data to eq. 5.2.

$$PDFF\,[\%] = \frac{\sum_i S_{of_i}}{S_{ow} + \sum_i S_{of_i}} \times 100 \tag{5.3}$$

5.2.1.4 Simulation

A Bloch equation simulation of the shMOLLI sequence was built in MATLAB (The MathWorks, Natick, MA, USA). The simulation used the same parameters of the shMOLLI protocol that were used during the imaging experiments. The measured signal was determined as the average signal over 59 phase encode lines centered at k = 29. A hyperbolic secant 1 (HS1) inversion pulse of 10.24 ms duration was used for inversion with time-bandwidth product R = 5.48, peak B_1 = 750 Hz, and β = 3.45. The evolution of magnetisation over time was simulated using Brian Hargreaves' Bloch equation simulator (http://mrsrl.stanford.edu/~brian/blochsim/).

Fat was characterised using the same six spectral peaks as evaluated by MRS. The chemical shift offset relative to water, relative amplitude, T_1 and T_2 relaxation times for each simulated component were determined from the multiple-TR, multiple-TE STEAM spectra of the peanut oil phantom. As an initial test of the phantom model, three simulations of the water signal were carried out corresponding to the three $NiCl_2$ concentrations, using the water T_2 values measured using the MCSE experiment and average STEAM water T_1 values for the given $NiCl_2$. The water and fat bSSFP signals were then combined according to the principle of partial volumes to reflect the PDFF determined by the multiple-TR, multiple-TE STEAM spectroscopy experiment for each fat-water phantom and input to the shMOLLI T_1 fitting algorithm. These simulated shMOLLI T_1 values were then compared with the measured shMOLLI T_1 as described in the statistics section.

5.2.1.5 *Determining the water shMOLLI T_1*

To determine the shMOLLI T_1 of the water component of the phantoms, the simulations above were repeated with water T_1 varied over the 500 – 1600 ms range in steps of 1 ms, and the complex water and fat signals were again combined according to the measured PDFF. The simulated signal that satisfied the maximisation problem described by eq. 5.4 was selected as the closest to the measured signal, where s represents simulated bSSFP signal vectors, s_{meas} is the measured bSSFP signal vector, θ is the angle between the simulated and measured signal vectors, the numerator of the fraction represents the absolute value of the dot product of the two vectors while the denominator represents the product of the lengths of the two vectors.

$$s = \underset{s\in\mathbb{C}7}{\operatorname{argmax}} \cos(\theta_{s-s_{meas}}) = \underset{s\in\mathbb{C}7}{\operatorname{argmax}} \frac{|s \cdot s_{meas}|}{||s|| \cdot ||s_{meas}||} \tag{5.4}$$

In practice, the cost function to be maximised in eq. 5.4 is the cosine of the angle between the experimentally sampled bSSFP signal and the simulated bSSFP signal. The cost function reaches its maximum when the vectors formed by the two signals are collinear. Once the maximisation was complete, an additional Bloch simulation was carried out to obtain the water-only signal that would have been generated by the MOLLI sequence on resonance. This signal was then fitted to eq. 5.5 to determine the apparent T_1 (T_1^*). ShMOLLI T_1 was obtained using the imperfect Look-Locker correction [30, 32] as described by eq. 5.6.

$$S_{sim}(TI) = A - Be^{-TI/T_1^*} \tag{5.5}$$

$$T_1 = T_1^* \left(\frac{B}{A} - 1\right) \tag{5.6}$$

The T_1 obtained in the last step was considered to be the water shMOLLI T_1 value. This process was repeated for each of the phantom vials.

5.2.2 *Patient study*

5.2.2.1 *Patient population*

A total of 30 patients (18 females, mean age: 53 ± 8.3 years) with normal livers (N = 11), alcoholic (N = 1) and non-alcoholic fatty liver disease (N = 18) were included. Participants were recruited from a hepatology clinic for a number of clinical imaging studies looking at various aspects of NAFLD. Inclusion criteria were: adults aged between 18 and 75 years old, BMI between 25 and 50 kg/m^2, 1.5 ≤ ALT < 10 ULN, blood pressure < 160/100 mmHg and primary diagnosis of NAFLD. Exclusion criteria were: diagnosis of diabetes, blood haemoglobin < 120 mg/dl, haemorrhagic disorders, anticoagulant treatment, presence of any contraindications to an MRI exam. Inclusion and exclusion criteria were chosen to minimise possible comorbidities. The study conformed to the ethical guidelines of the 1975 Declaration of Helsinki, and was approved by the institutional research departments and the National Research Ethics Service. All patients gave written informed consent.

5.2.2.2 *Imaging*

Patients were scanned using the same scanner and coils as described in the phantom work and using the same imaging and spectroscopic sequences. 6 or 9 channels of the spine array coil were used, depending on patient liver size. T_2^* values were obtained using a T_2^*-IDEAL fat-water separation method with field map estimation using a graph-cut algorithm and a signal model described by Hernando et al. [140] (eq. 5.7).

$$S(\rho_w, \rho_f, T_2^*, \psi, TE_n) = e^{-TE_n/T_2^*} \left(\rho_w + \rho_f \sum_{k=1}^{p} \alpha_k e^{2\pi i f_k TE_n} \right) e^{-2\pi i \psi TE_n} \tag{5.7}$$

Here, ρ_w and ρ_f stand for the relative proton densities of water and fat, ψ represents field inhomogeneities, T_2^* is common for fat and water, TE_n represents the nth echo time, a_k is

the relative amplitude of the kth fat peak, f_k is the chemical shift offset of the kth fat peak and p is the total number of fat peaks (p = 6 in the present model). Equation 5.7 was fitted to multiple-echo GRE data to find ρ_w, ρ_f, T_2^* and ψ, with TE, α_k and f_k being kept constant. Eq. 5.8 was then applied to obtain HIC values in milligrams per gram dry weight of hepatic tissue [16, 99].

$$HIC\,[mg/gd.w.] = \frac{0.0254}{2}(1/T_2^* + 11) + 0.202 \tag{5.8}$$

Hepatic shMOLLI T_1 maps had TR = 2.45 ms, bSSFP TE varied between 1.02 and 1.05 ms, FOV 270–300 × 360–400 mm^2, 24 k-space lines before the central line, 66 total k-space lines, shortest inversion time was either 100 ms or 110 ms, inversion time increment 80 ms. Additionally, a single-voxel long-TR STEAM ^1H spectroscopy sequence [132] was also run with and without water suppression. These spectra were used to quantify PDFF. Sequence parameters were: TR was cardiac gated and at least 2 s for suppressed spectra and at least 4 s for non-suppressed spectra, TE = 10 ms, and TM = 7 ms. Voxel size was 20 × 20 × 20 mm^3 for both spectroscopy experiments. Water suppressed and non-water suppressed spectra were processed using AMARES and combined with a specialized MATLAB script [132]. PDFF was determined as the ratio of the sum of areas of fat peaks and the sum of water and fat peak areas, and was T_2-corrected using eq. 5.9. Whenever fat peaks were not visible, their amplitudes were determined using the relative amplitudes reported by Hamilton et al. [81].

$$PDFF\,[\%] = \frac{\sum_i F_i}{We^{TER_2} + \sum_i F_i} \times 100 \tag{5.9}$$

where F_i are the fitted amplitudes of fat peaks, W is the fitted amplitude of the water peak, TE is the spectroscopic echo time and R_2 is the transverse relaxation rate of the water in the liver in s^{-1}, given by eq. 5.10 [16, 92, 144], where HIC is measured in mg/gdryweight.

$$R_2 = 1/T_2 = 1.47(6.88 + 26.06HIC^{0.701} - 0.438HIC^{1.402}) - 2.2\,[s^{-1}] \tag{5.10}$$

All images were acquired in a single transverse slice positioned between the tenth and eleventh thoracic vertebrae, during a breath-hold. Breath-held localized spectroscopy was performed in a voxel placed in the right lobe of the liver, away from the margin of the liver and from major blood vessels and bile ducts making sure the voxel lay in the plane used for imaging. Breath-hold lengths varied between 9 and 15 seconds for imaging and were 12 seconds for the long-TR spectroscopy acquisition and 21 seconds for the multiple-TR, multiple-TE acquisition.

5.2.2.3 The MOLLI water T_1 determination algorithm

Time-varying magnetisation of water and fat were simulated using Brian Hargreaves' Bloch equation simulator (http://mrsrl.stanford.edu/~brian/blochsim/). A version of the liver model introduced by Tunnicliffe et al. [14] was used, as shown in fig. 5.1. This model comprises an intracellular and an extracellular space, with the extracellular space divided into an interstitial fluid pool and a blood pool in fast exchange. In this model the intracellular space is subdivided into a semisolid pool representing macromolecules and a liquid pool representing the cytosol of hepatocytes. This liver model was extended with an additional fat component and volume fractions of the extracellular fluid and the intracellular compartment were adjusted to reflect the fat fraction of the liver. Volume fractions, and T_1 and T_2 constants for the modelled compartments are summarised in table 5.1.

In a separate simulation water exchange between intra- and extracellular spaces and magnetisation transfer (MT) between the semisolid and liquid intracellular pools have also been modelled using the Bloch-McConnell equations as described by Tunnicliffe et al. [14]. Additional volume fractions and T_1 and T_2 constants, and exchange rates are summarised in table 5.2.

Fat was again characterised using six spectral peaks, with the chemical shift offsets

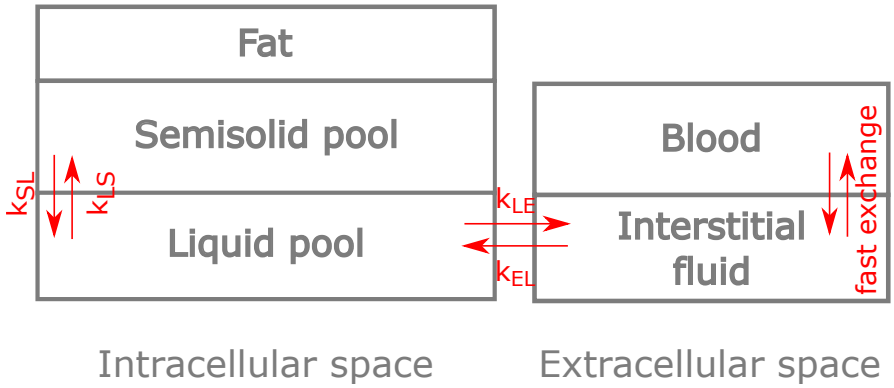

Figure 5.1: A diagram of the liver tissue model used in this chapter. Arrows show the direction of exchange, k_{EL} and k_{LE} are exchange rates between the liquid pool of the intracellular space and the interstitial fluid of the extracelllular space, while k_{SL} and k_{LS} are exchange rates between the semisolid and the liquid pools of the intracellular space.

relative to water and relative amplitudes given by Hamilton et al [81]. T_1 and T_2 values of different lipid spectral peaks were fixed to values measured in the peanut oil spectra collected with the multiple-TR, multiple-TE STEAM sequence, except for the 2.76, 2.1, 1.3, and 0.9 ppm peaks of the human liver fat, for which T_2 values reported by Hamilton et al. [81] were used. T_1 of the methylene fat peak at 1.3 ppm was quantified in patients with PDFF > 5% using the multiple-TR STEAM ^{1}H MRS sequence, and a value averaged over subjects was used in the simulations. Table 5.1 summarizes parameters used for the simulation, while table 5.2 contains additional parameters used in the model that includes exchange effects.

Longitudinal and transverse relaxation rates of non-fatty compartments and their iron dependence were the same as described in the main simulation by Tunnicliffe et al [14] and are shown in Table 5.3. The longitudinal relaxation rate of the intracellular compartment in the absence of iron, was determined such that the simulated signal for normal HIC (1.0 mg/gdryweight [14]), 0% fat, on resonance, and normal extracellular fluid volume fraction (v_E) (0.4) had a fitted T_1 value equal to the shMOLLI T_1 in healthy volunteers of 717 ms [13].

Table 5.1: Simulation parameters for the liver model at 3 Tesla

Parameter	Value
PDFF	Proton density fat fraction as measured by ^{1}H STEAM MRS
v_C	$1 - v_E$
v_E	Simulated from 0.25 to (0.95 - PDFF)
v_B	$(1 - v_E)/3$
v_I	$v_E - v_B$
f [Hz]	As determined from the multiple-echo GRE sequence
Fat chemical shifts [ppm]	As determined by the multiple-TR, multiple-TE STEAM ^{1}H MRS sequence of peanut oil
T_{1fat} [s]	T_1 of methylene peak determined from human ^{1}H spectra. Others as determined by the multiple-TR, multiple-TE STEAM ^{1}H MRS sequence of peanut oil.
T_{2fat} [s]	Values have been taken from literature [145] where available or from peanut oil spectra.*
R_{2E} [s^{-1}]	$(3.64v_B + 2.9v_I)/v_E + 26.82HIC^{0.701} - 0.45HIC^{1.402}$
R_{2C} [s^{-1}]	$11.0 + 46.0HIC^{0.701} - 0.773HIC^{1.402}$
R_{1E} [s^{-1}]	$(0.52v_B + 0.44v_I)/v_E + 0.029HIC$
R_{1C} [s^{-1}]	$1.6 + 0.029HIC$

PDFF: proton density fat fraction, $v_{(C,E,B,I)}$: unitless volume fractions of the intracellular pool, extracellular fluid, blood, and interstitial fluid, f: off-resonance frequency.

$R_{2(E,C)}$: transverse relaxation rates, $R_{1(E,C)}$: longitudinal relaxation rates.

* For the full characterisation of fat, see data in table 5.3.

Table 5.2: Additional simulation parameters for the liver model at 3 Tesla when considering exchange effects

Parameter	Value
v_s	$0.07(1 - PDFF)$
v_L	$0.93(1 - PDFF)$
R_{2S} [s^{-1}]	$1/(7.7 \times 10^{-6})$
R_{2L} [s^{-1}]	$11.0 + 46.0HIC^{0.701} - 0.773HIC^{1.402}$
R_{1S} [s^{-1}]	1.00
R_{1L} [s^{-1}]	1.6 + 0.029HIC
k_{LS} [s^{-1}]	$3.52/v_L$
k_{SL} [s^{-1}]	$3.52/v_s$
k_{EL}, k_{LE} [s^{-1}]	$0.52/v_E$
k_{LE} [s^{-1}]	$0.52/v_L$

$v_{S,L}$: unitless volume fractions of the semisolid and liquid components of the intracellular pool. $R_{2(S,L)}$: transverse relaxation rates, $R_{1(S,L)}$: longitudinal relaxation rates.

v_E was varied between 0.25 and 0.95 in steps of 0.01 and was used as a proxy for liver fibrosis. To have as good an approximation of the scanner measurement as possible, the shMOLLI RF pulse sequence was simulated using the exact inversion, repetition, and echo times, as well as number of phase encoding lines, extracted from the patient shMOLLI images. Once separate bSSFP signals were simulated for the intracellular pool, extracellular pool, and hepatic fat, they were combined as a volume fraction-weighted sum, as given by eq. 5.11.

$$S_{sim} = (v_E \times S_e + (1 - v_E) \times S_i) \times (1 - PDFF) + PDFF \times S_f \tag{5.11}$$

In this equation S_{sim} represents the overall simulated shMOLLI signal, S_e is the simulated extracellular signal, S_i is the simulated intracellular signal and S_f is the simulated fat signal. As before, the optimal simulated signal was identified by solving the maximisation problem

described by eq. 5.4. ROIs were placed in the posterior and lateral parts of the right lobe and in the left lobe, in a way to avoid vessels and bile ducts. The v_E corresponding to the optimal signal was used to simulate a fat- and iron-free signal on resonance and T_1 and T_2 values of the liver compartments corresponding to normal HIC. This signal was then processed using the shMOLLI conditional fitting algorithm to obtain a water shMOLLI T_1 which should be independent of iron, fat and off-resonance frequency.

In addition, in one subject, three separate shMOLLI T_1 maps were produced for a single liver slice: an iron-corrected, on-resonance water (as above using ROIs); iron-corrected, on resonance mixed fat-water; and iron-corrected, inhomogeneous B_0, water MOLLI T_1. Voxel-by-voxel PDFF values were determined from the T_2^*-IDEAL fat-water separation method described above. The shMOLLI T_1 map and GRE data used for this experiment were collected after a linear frequency change was induced in the right-left direction by changing the value of the shim gradient in the x direction. The mechanisms used for both phantom and patient on-resonance water MOLLI T_1 are summarized in a block diagram shown in fig. 5.2. The liver model was verified against a forward simulation of patient shMOLLI T_1 measurements by simulating the extracellular, intracellular and fat bSSFP signals. The extracellular volume fraction for each patient was estimated based on the spectroscopically measured water T_1 and using the relationship between blood volume fraction and interstitial volume fraction as given in Table 5.2 and given T_1 of intra- and extracellular compartments. T_1 and T_2 for the simulations were determined based on Table 5.2 for the intracellular and extracellular compartments, given the patients' measured HIC. The fat signal was simulated using the T_1 and T_2 values in Table 5.3. These simulated signals were combined as a volume-fraction weighted sum and fit using the shMOLLI algorithm to produce the expected shMOLLI T_1 given this measured spectroscopic T_1.

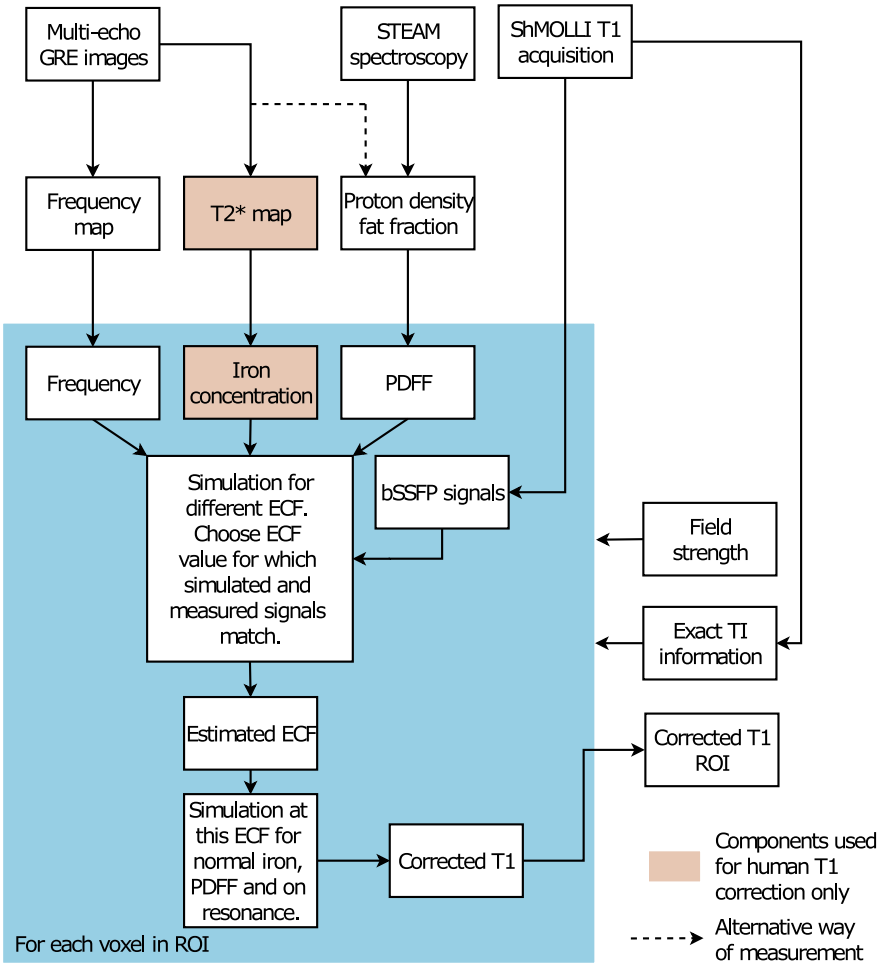

Figure 5.2: Block diagram of the water shMOLLI T_1 determination algorithm. In addition to the shMOLLI T_1 map, a multiple-echo GRE image set and a STEAM ^1H spectrum were also collected to derive a B_0 field map of the imaged slice and the PDFF. When the algorithm was used to determine water shMOLLI T_1 values in patients, the GRE images were also used to generate T_2^* values and, thus, hepatic iron concentration values. Knowledge of field strength was necessary for the correct modelling of lipid peaks and the effect of iron. The actual (heart rate dependent) inversion times were used as in the imaging experiments to eliminate possible errors caused by variable heart rates [31]

5.2.3 *Statistical analysis*

Correlation between simulated and measured shMOLLI T_1 values of phantoms, as well as correlation of iron-corrected shMOLLI T_1 and iron-, fat- and off-resonance-independent water shMOLLI T_1 values with spectroscopically determined water T_1 values in patients

was evaluated using Pearson's correlation coefficient. Bland-Altman plots [146] were built to evaluate agreement between water T_1s derived from STEAM spectroscopy and iron-corrected shMOLLI T_1s, and between water T_1s derived from STEAM spectroscopy and iron-, fat- and off-resonance-independent water shMOLLI T_1s. A left-tailed F-test was used to evaluate the change in the variance of T_1 differences shown on the Bland-Altman plots. All statistical hypothesis testing was performed at significance level $\alpha = 0.05$.

5.3 RESULTS

5.3.1 *Phantom experiments*

Table 5.3 summarizes the results of measurements made using the 100% peanut oil phantom. These values were used to characterise fat in the phantom correction algorithm. Table 5.4 shows PDFF, T_1, T_2, and shMOLLI T_1 of individual fat-water phantoms. Simulated and measured phantom shMOLLI T_1 values showed good agreement ($r = 0.999$, $p < 0.001$), as reflected by fig. 5.3a. Figure 5.3b shows the corrected on-resonance water shMOLLI T_1 in comparison with the measured shMOLLI T_1 values. Fat-dependent shMOLLI T_1 had a clear systematic dependence on PDFF and a weaker correlation ($r = 0.910$, $p < 0.001$) with spectroscopy-based T_1 than fat-independent water shMOLLI T_1 ($r = 0.998$, $p < 0.001$). On-resonance water shMOLLI T_1 had significantly ($F = 15.003$, $p < 0.005$) lower variance than measured shMOLLI T_1 of the difference between phantom water T_1s measured by STEAM and by shMOLLI, as shown in fig. 5.4, a modified Bland-Altman plot that captures the dependence of the difference between STEAM and shMOLLI T_1s on their average value.

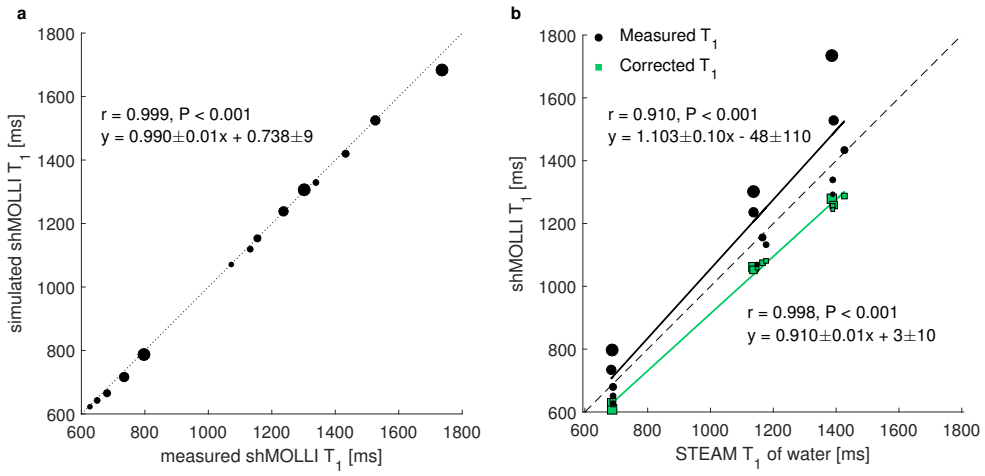

Figure 5.3: (a) "Forward" shMOLLI simulation of the phantoms shows excellent agreement with measured shMOLLI T_1 values. (b) Correlation between shMOLLI T_1 and spectroscopy-based T_1 increases after removing the effects of fat. It is expected to obtain shMOLLI T_1s lower than T_1s obtained from spectroscopy after the determination of water shMOLLI T_1 values, due to the recovery of the longitudinal magnetisation being disturbed by the bSSFP readouts and the dependence of shMOLLI on the T_2 of the imaged tissue [31, 109]. Points on both graphs are size-coded as a function of phantom PDFF.

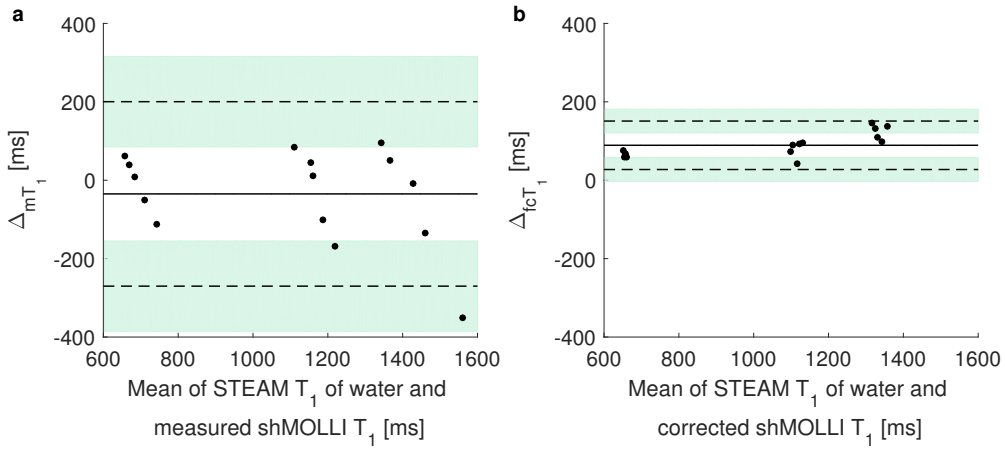

Figure 5.4: Modified Bland-Altman plots showing phantom data before (a) and after (b) applying the water shMOLLI T_1 determination algorithm. Δ_{mT_1} is the difference between STEAM T_1 and the measured shMOLLI T_1; Δ_{fcT_1} is the difference between STEAM T_1 and the fat-independent water shMOLLI T_1. The near-zero bias on subfigure (a) is due to the increased shMOLLI T_1 values observed at high fat fractions, while a bias of 89 ms on subfigure (b) can be explained by the expected [31] underestimation of T_1 values by the shMOLLI method. An F-test performed on the two differences shown in the subfigures revealed that the variance of the measurements statistically significantly decreased after removing the effects of fat, iron and off-resonance frequency ($F = 15.003$, $p < 0.001$).

Table 5.3: Fat peak parameters used in the Bloch simulation of the shMOLLI sequence. T_1 and T_2 values of fat peaks in peanut oil were measured at room temperature (20°C) for the phantom work and at human body temperature (37°C) for human experiments

			Peanut oil (T=20°C)		Participants (T=37°C)	
Peak no.	Chemical shift (relative to tetramethylsilane) [ppm]	Relative amplitude [a.u.]	T_1±SD [ms]	T_2±SD [ms]	T_1±SD [ms]	T_2±SD [ms]
1	0.90	0.087	264±20	54±3	333±12	83*
2	1.30	0.693	291±21	61±1	312±17**	62*
3	2.10	0.128	231±18	52±3	254±8	52*
4	2.76	0.004	248±25	61±5	273±8	51*
5	4.30	0.039	193±14	43±2	228±8	49±3
6	5.30	0.049	285±15	48±2	332±15	50±4

*As reported by Hamilton et al. [81]

**As measured in livers of participants

5.3.2 *Patient studies*

Of 30 patients, 19 (63.3%) had hepatic steatosis (PDFF > 5%). The patient's fat fractions ranged from 1.53% to 20.33% and T_2^* values ranged from 6.3 ms to 37.9 ms (HIC range 0.677 mg/g dry weight – 2.357 mg/g dry weight). Relaxation times of individual fat peaks used for modelling the fat compartment are summarized in table 5.3. Figure 5.5a shows the results of the forward simulation, while fig. 5.5b shows the results of the fat correction in patients. While iron-corrected shMOLLI T_1 values correlated moderately ($r = 0.493$, $p = 0.005$) with spectroscopically measured water T_1s, the fat-independent water shMOLLI T_1 determination algorithm yielded a stronger correlation with STEAM T_1 values ($r = 0.771$, $p < 0.001$).

Table 5.4: Baseline parameter values for fat-water phantoms, as measured with multiple-contrast spin echo, shMOLLI, and multiple-TR STEAM ^{1}H MRS. Water T_2 and shMOLLI T_1 were averaged over circular regions of interest on corresponding maps.

$NiCl_2$ concentration [mM]	PDFF [%]	STEAM T_1 of water ± SD [ms]	T_2 of water ± SD [ms]	shMOLLI T_1 ± [ms]
0.45	0.0	1390±30	78±3	1294±31
	7.0	1386±24	*	1340±29
	10.3	1425±35	*	1433±38
	15.6	1392±29	*	1527±42
	26.8	1386±17	*	1736±62
0.73	0.0	1148±29	82±2	1071±18
	7.3	1177±34	*	1132±25
	11.1	1169±20	*	1156±21
	16.0	1136±30	*	1236±31
	24.7	1135±28	*	1303±39
1.61	0.0	690±23	89±5	627±7
	6.8	690±29	*	651±7
	12.6	689±27	*	680±8
	21.5	684±20	*	735±11
	27.0	687±16	*	798±12

*As the MCSE experiment could not be used to determine water T_2 when mixed with fat, we have used the same water T_2 within a $NiCl_2$ concentration group as the T_2 measured in the 0% fat phantom of each group.

Similarly, the large variability between STEAM and iron-corrected shMOLLI T_1 introduced by the effect of fat is significantly reduced by the water shMOLLI T_1 determination algorithm ($F = 0.345$, $p < 0.005$), as seen on the modified Bland-Altman plot of fig. 5.6.

Figures 5.7b and 5.8 show similar improvement in the correlation between STEAM T_1s and shMOLLI T_1s, and a reduction in the variance of shMOLLI T_1 values (according to a similar modified Bland-Altman diagram to those described in previous sections) when using a liver model that incorporates water exchange and magnetisation transfer effects. The forward simulation results in the presence of magnetisation transfer and water exchange effects (fig. 5.7a) are somewhat inferior to those obtained without considering exchange effects. A paired t-test between water shMOLLI T_1s with and without exchange modelling has not revealed a significant difference between the two resulting sets of water shMOLLI T_1 values ($p = 0.528$). The values determined when considering exchange effects were numerically, but not statistically significantly (left-tailed t-test, $p = 0.459$) lower than their counterparts from the simulation without exchange effects, which is in line with previous results [14].

Table 5.5 contains linear regression coefficients for the dependence of shMOLLI T_1 on water STEAM T_1, PDFF and R_2^* ($= 1/T_2{}^*$) values as well as P-values associated with these coefficients, showing that on-resonance water shMOLLI T_1 values do not show statistically significant dependence on fat. Figure 5.9 shows the results of applying the algorithm pixel-by-pixel over the a single slice liver shMOLLI T_1 map of a patient. The liver had, on average, HIC = 1.0 mg/g dry weight, PDFF = 14%, and a linearly varying frequency offset in the right-left direction with frequency offsets ranging from -50 Hz to 35 Hz, which was artificially applied by manually modifying the B_0 shim. Figures 5.9b, d, and g show the results of the algorithm with three different models applied on the same T_1 map of the liver: full modelling of the effects of iron, fat and B_0 inhomogeneity (fig. 5.9b), a model of iron and fat effects (fig. 5.9d) and a model containing effects from iron and B_0 inhomogeneity (fig. 5.9g). The maps in the third column of the last two rows show the T_1 difference between the complete model and the partial models. As was expected, a linear variation in off-

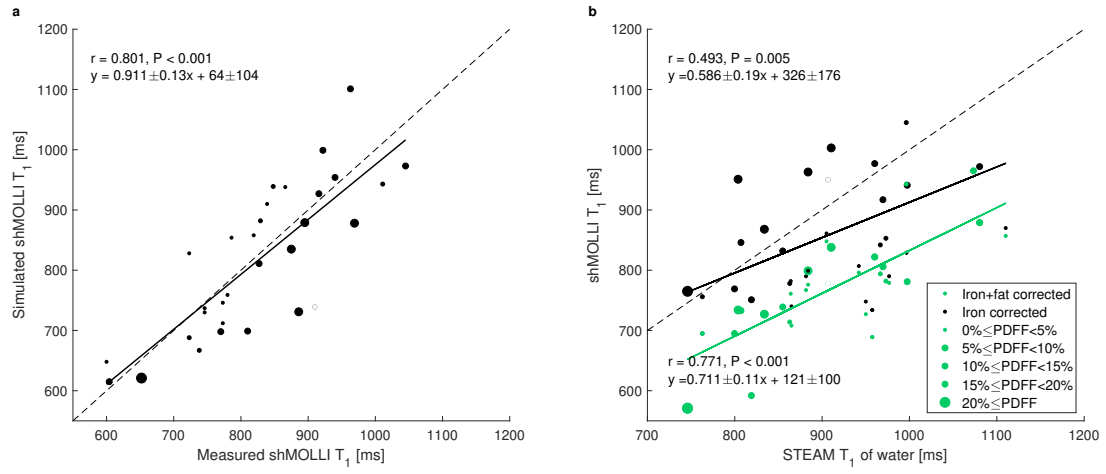

Figure 5.5: (a) "Forward" simulation of patient shMOLLI T_1 measurements. (b) Correlation between water shMOLLI T_1 values and spectroscopically measured T_1s of the water in the liver increased after extending the initial iron-only correction to removing the effects of iron, fat, and off-resonance. The dashed line represents the line of identity.

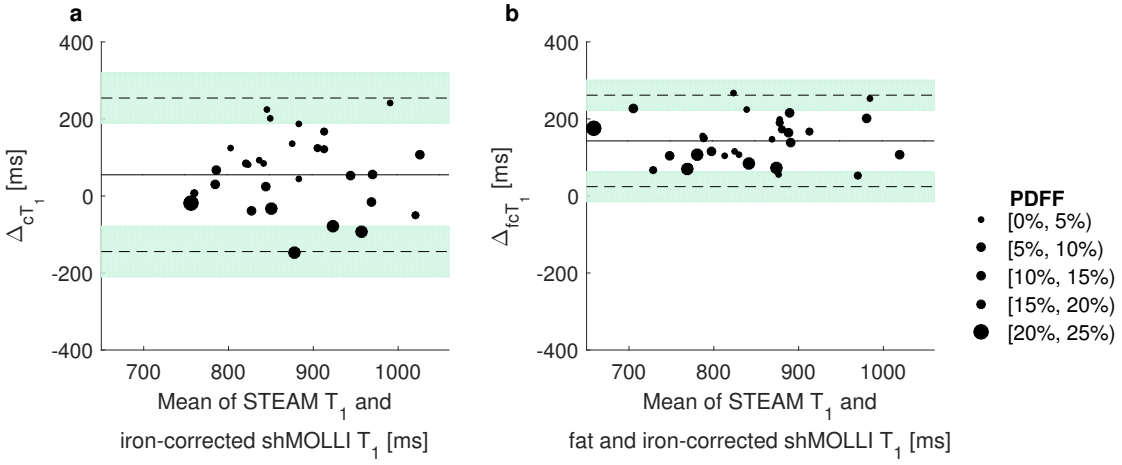

Figure 5.6: Modified Bland-Altman plots of the iron-corrected (a) and iron-, fat-, and off-resonance-independent patient data (b). Δ_{cT_1} is the difference between STEAM T_1 of the water in the liver and the iron-corrected shMOLLI T_1; Δ_{fcT_1} is the difference between STEAM T_1 of the water in the liver and the iron-, fat- and off-resonance-independent water shMOLLI T_1. A statistically significant (F statistic = 0.345, $p < 0.005$) reduction of the variance in the difference between STEAM T_1 and shMOLLI T_1 values is observed after removing the effects of iron, fat and B_0 inhomogeneities, as well as the removal of the systematic trend for higher fat concentration to lead to longer shMOLLI T_1. As in the case of phantoms, the large bias in subfigure b is caused by the underestimation of T_1s by the shMOLLI method.

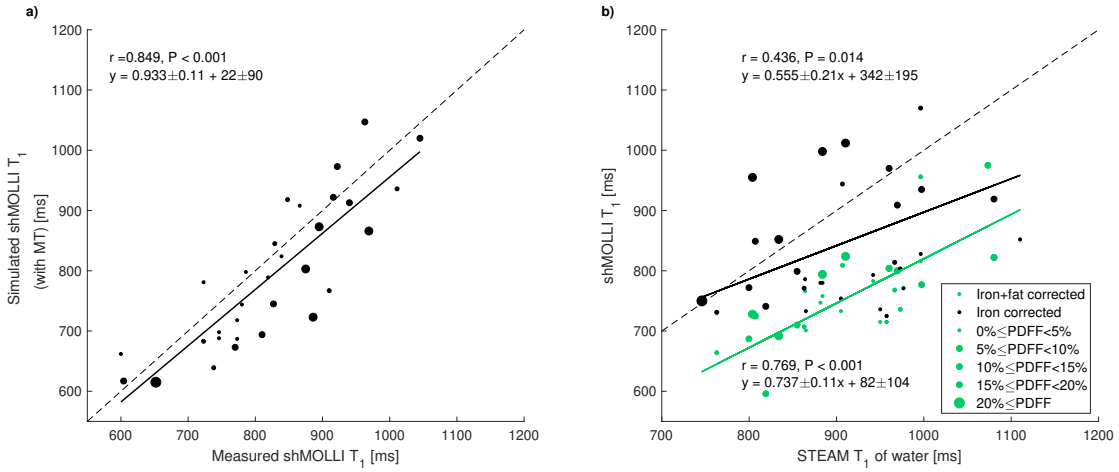

Figure 5.7: (a) "Forward" simulation of patient shMOLLI T_1 measurements while also considering magnetisation transfer effects. (b) Correcting for fat when also considering magnetisation transfer effects increases the correlation between STEAM T_1 of the water in the liver and shMOLLI T_1 values. PDFF of individual data points is encoded in symbol size. The dashed line represents the line of identity.

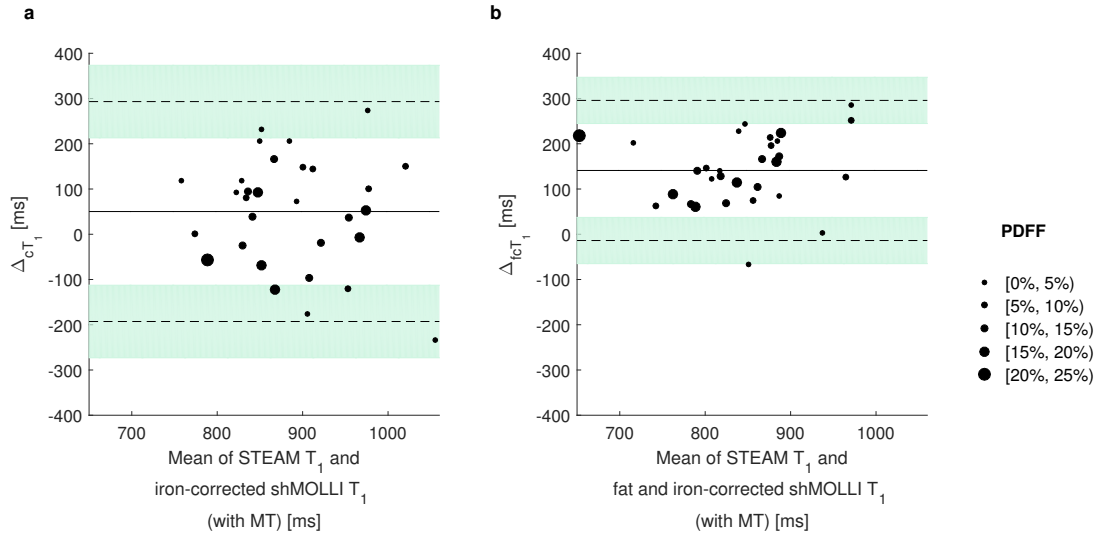

Figure 5.8: Modified Bland-Altman plots showing patient data after iron-only (a) and after (b) iron, fat, and off-resonance correction with an exchange-enabled liver model. Δ_{cT_1} is the difference between STEAM T_1 of the water in the liver and the iron-corrected shMOLLI T_1; Δ_{fcT_1} is the difference between STEAM T_1 of the water in the liver and the iron-, fat-, and off-resonance-corrected shMOLLI T_1. The underestimation of T_1 values by the shMOLLI T_1 method explains the bias on the agreement plots. An F-test performed on the two differences shown in the subfigures revealed that the variance of measurements significantly decreased after the correction (F statistic = 0.294, $p < 0.001$).

Table 5.5: Linear regression correlation coefficients for shMOLLI T_1 dependence on water STEAM T_1, PDFF and liver R_2^*, determined from original measured shMOLLI T_1 values, iron-corrected shMOLLI T_1 values, and iron-, fat-, and off-resonance-independent water shMOLLI T_1 values. Coefficients are shown as estimate ± standard error

	STEAM T_1 coefficient [ms/ms]	P-value	PDFF coefficient [ms/%]	P-value	R_2^* coefficient [ms/s^{-1}]	P-value
Model without exchange effects						
Measured shMOLLI T_1	0.5±0.2	0.005	11.7±2.5	<0.001	-1.7±0.4	<0.001
Iron-corrected shMOLLI T_1	0.8±0.1	<0.001	13.9±2.1	<0.001	-0.4±0.4	0.354
Iron-, fat- and off-resonance-independent water shMOLLI T_1	0.7±0.1	<0.001	2.9±1.7	0.104	-0.6±0.3	0.040
Model with exchange effects						
Measured shMOLLI T_1	0.5±0.2	0.005	11.7±2.5	<0.001	-1.7±0.4	<0.001
Iron-corrected shMOLLI T_1	0.9±0.1	<0.001	14.8±2.3	<0.001	-0.04±0.4	0.925
Iron-, fat-, and off-resonance-independent water shMOLLI T_1	0.8±0.1	<0.001	2.5±1.9	0.203	-0.3±0.3	0.432

resonance frequencies over a range including both positive and negative values caused both an increase and a decrease of T_1 values 10, in this case by up to 50 ms. This under- and overestimation of T_1 values is reflected in the difference between the iron-, fat- and off-resonance-independent water shMOLLI T_1 map and the iron and fat-independent T_1 map of fig. 5.9e. When removing the effects of iron and off-resonance frequencies only, the effects of fat lead to higher-than-expected shMOLLI T_1 values, as shown in fig. 5.9h, in this case by up to 250 ms.

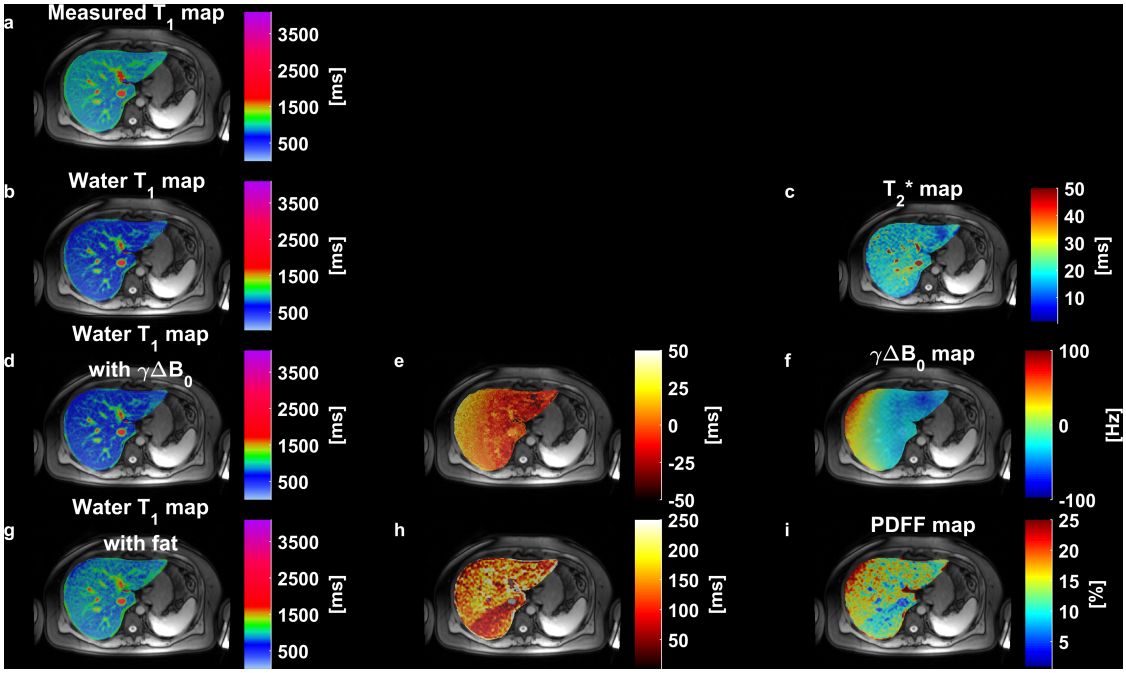

Figure 5.9: (a) An example of liver shMOLLI T_1 map affected by fat and B_0 inhomogeneity. (b) A normal liver T_1 map resulted after removing the effects of fat, iron and B_0 inhomogeneity. (c) The calculated T_2^* map shows a homogeneous distribution of normal iron concentrations. Two additional models were used to determine the water shMOLLI T_1: one without accounting for B_0 inhomogeneity and another without accounting for fat. Subfigure (d) shows the resulting T_1 map after the effects of iron and fat have been removed; subfigure (e) shows the difference between the T_1 map obtained by using the full model and this alternative corrected T_1 map (e=b-d). Subfigure (f) presents the B_0 inhomogeneity map over the liver of this patient, showing the forcibly set linearly varying frequency in the left-right direction. Removing the effects of iron and B_0 inhomogeneity only (g) yields higher-than-normal T_1 values. The difference between this alternative T_1 map and the water shMOLLI T_1 map determined using the full model (h, h=b-g) is explained by the effects of the fat, as shown in the PDFF map (i).

5.4 DISCUSSION

This study describes an extension of the liver model proposed by Tunnicliffe et al. [14] to include a variable sized fat compartment and a frequency offset calculated from the GRE data used for T_2^* mapping, thus obtaining a model reflecting the effects of iron, fat, and off-resonance frequencies on T_1 measured by MOLLI variants. This model then allowed the identification of an on-resonance water (sh)MOLLI T_1 value: the value that would have been measured if subjects had 0% PDFF, and normal HIC (i.e. 1 mg/gdryweight) and were imaged in a perfectly homogeneous static magnetic field. The results of the on-resonance water shMOLLI T_1 determination algorithm showed excellent correlation with spectroscopically determined water T_1 values in phantoms, and increased, statistically-significant correlation in human participants, when compared to iron-corrected shMOLLI T_1, and reduced variance of the difference between STEAM T_1 of water and water shMOLLI T_1.

In addition to the assumptions of Tunnicliffe et al. regarding the homogeneous distribution of iron between the liver parenchyma and extracellular fluid, we further assumed that fat droplets in hepatocytes appear in a macrovesicular form, which is mostly prevalent in non-alcoholic fatty liver disease [147], thus not affecting the tumbling rate of water molecules in hepatocytes. We have not explored possible different relaxation mechanisms in the presence of microvesicular fat.

A further assumption was that the T_1 and T_2 relaxation times of lipid protons are independent of iron. It has been shown previously that the T_2^* of both water and fat is affected by iron [89]. However, fat diffuses much more slowly than water molecules because of the high molecular weights of constituent triglycerides, therefore, their transverse T_2 relaxation will be affected less by local field inhomogeneities. The independence of

longitudinal relaxation of fat on iron is guaranteed by the lack of magnetisation transfer between lipid macromolecules and water [148].

In the T_2^*-IDEAL model, we assumed equal T_2^* for fat and water. As Bydder et al. have pointed out in a recent work [88], the T_2^* of fat and water cannot be considered to be equal, due to the susceptibility difference of the two species. Although using a single T_2^* in the fat-water signal model ensures numerical stability of the fitting, it can also lead to the underestimation of PDFF values. The error on the PDFF determined with and without modelling the different T_2^* times was <1.5% and we did not consider different T_2^* values in this work. We expect that this simplification will lead to negligible errors in the determination of on-resonance water T_1s.

Our proposed algorithm can be implemented in at least two ways. Running the algorithm "on-line", as we have done here, by simulating patient signals every time an on-resonance water shMOLLI T_1 is needed is one option. The time needed to run the on-line version of the algorithm for an individual voxel is ~25 seconds, resulting in a long time (~1.5 days) necessary for the generation of an entire fat, iron and frequency independent shMOLLI T_1 map of the liver. Alternatively, one can build a look-up table a priori and look up the measured T_1 values along axes of off-resonance frequency, PDFF and HIC and then project the T_1 value along the identified v_E axis to 0 Hz off-resonance frequency, 1 mg/gdryweight HIC, and 0% PDFF. In this study, we have used ^{1}H STEAM MRS to determine PDFF locally and determine the water shMOLLI T_1 over a spectroscopic voxel of interest, as well as a T_2^*-IDEAL fat-water separation method with field map estimation method to map fat fractions over the imaging slice, allowing determination of water shMOLLI T_1 values over the whole liver slice.

Human hepatic lipid was modelled using a hybrid model comprising chemical shift, relative amplitude, T_1 and T_2 values taken from human hepatic lipid literature and – due

to its similarity to subcutaneous fat [149] – peanut oil spectroscopy measurements. However, it has been shown that the hepatic fat spectrum is different from the spectrum of abdominal subcutaneous adipose tissue [150, 151], therefore, errors in the correction due to the inaccurate spectral modelling might reveal themselves at higher fat fractions where small fat peaks have a larger contribution to the overall signal. Furthermore, T_1 and T_2 relaxation times of individual fat peaks of the peanut oil spectra were determined using mono-exponential fitting. However, it is known that J-coupling effects disturb the pure mono-exponential behaviour of these peaks. Since J-coupling effects were not included in Bloch equation simulations and approximate relaxation times of fat peaks gave satisfactory results in phantoms, we chose not to consider J-coupling effects in the patient study either.

Validation of the whole multi-compartment model as an extension of the model described by Tunnicliffe et al. [14] is difficult, due to the challenge of building phantoms with multiple sub-voxel water compartments, mimicking liver tissue. However, we built an array of fat–water phantoms with two compartments and proved the validity of fat modelling and the water shMOLLI T_1 determination algorithm using these phantoms.

While the T_1 value of the tissue water can be determined spectroscopically [125], there have been attempts to also produce T_1 maps of tissue that are independent of fat. Hoad et al. [12] reported results of a liver imaging study involving participants with fibrotic livers, in which a liver T_1 determined using an IR SE-EPI sequence was shown to be independent of fat and to correlate well with fibrosis. Pagano et al. [152] proposed an IDEAL-T_1 technique that is a modified version of SASHA [112] collecting images at several echo times for each saturation time over two breath-holds. A different approach was described by Nezafat et al. [153] that uses a modified version of the slice-interleaved T_1 (STONE) sequence [154] with spectrally water-selective inversion pulses instead of adiabatic inversion pulses. A more recent method uses the Water-Only Look-Locker Inversion recovery (WOLLI)

sequence [155], that produces water-only T_1 maps by using hypergeometric inversion pulses to selectively invert water. However, our proposed method of determining water (sh)MOLLI T_1 maps independent of the effects of fat also shows promise as (sh)MOLLI is widely available and water shMOLLI T_1 values can be extracted retrospectively.

One of the limitations of this study is that water shMOLLI T_1 values of only 30 patients were determined and only 19 patients had clinically significant fat fractions in their livers, i.e. PDFF > 5%. The range of fat fractions in our patient population was 1.53% – 20.33%, therefore the correction method was not validated in patients with higher liver fat fractions, although it is known that the concentration of fat in the liver can reach 45% [84, 119]. We also considered only single slice coverage of the liver, along with performing ROI-based analyses instead of mapping over the acquired slice in all but one case. While the forward simulation of patient shMOLLI T_1 did not completely recover the measured shMOLLI T_1 irrespective of the inclusion of exchange effects, the gradient and intercept are statistically equivalent to 1 and 0 and simulation results were spread relatively uniformly around the unity line with respect to fat and iron concentration distributions (when ignoring exchange effects), suggesting that the remaining variability in water shMOLLI T_1 values determined by our algorithm might be due to the variability of the normal population and random measurement errors of the input model parameters, and not other influencing factors, such as inflammation, in which case the simulation results would be either predominantly above or below the line of unity. Errors in estimating T_1 using all or individual model parameters might be possible to determine using sensitivity analysis. Even though the multivariable regression analysis of on resonance water T_1 values of patients has shown statistically significant dependence on iron, this was due to a single participant with high iron concentration and a very low on resonance water T_1.

5.5 CONCLUSION

An algorithm for the determination of water shMOLLI T_1 values unaffected by iron, fat and magnetic field inhomogeneities was presented and has been shown to be reliably capable of recovering water shMOLLI T_1 in phantoms and in patients with fatty livers. This algorithm, when used in conjunction to a multi-parametric MRI study protocol, may contribute towards a better non-invasive characterisation of fibro-inflammatory liver disease using MRI methods. The association between liver fibrosis stages and shMOLLI T_1 values obtained with the algorithm will be explored in the next chapter.

6

Water-only shMOLLI T_1 is associated with fibrosis stage

6.1 INTRODUCTION

Chapter 4 characterised the effect of fat on liver shMOLLI T_1 measurements, while chapter 5 presented a method to determine water-only shMOLLI T_1 values in the presence of fat. As has been emphasised in previous chapters, NAFLD is a disease with increasing world-wide prevalence, therefore it is of great importance to develop non-invasive biomarkers that facilitate its diagnosis and follow-up. ShMOLLI T_1 mapping was suggested to be of help in solving this problem [13, 115]. However, in the light of previously presented results, it is reasonable to expect that removing the effects of fat and off-resonance frequency, in addition to that of iron, will increase the correlation between shMOLLI T_1 and indicators of fibrosis, assuming that it is the T_1 of water that is of clinical significance. The aim of this chapter is, thus, to test this hypothesis by determining the water shMOLLI T_1 in livers of

participants with $PDFF_{liver} \geq 5\%$.

6.2 METHODS

6.2.1 *Participants*

Data from participants enrolled in a previously described study [13] group were retrospectively analysed. This study compared MRI measurements to liver needle biopsy outcomes as reference standard. Out of 97 participants with successful biopsy and MRI results, only those were selected for this retrospective analysis who had $PDFF_{liver} \geq 5\%$ (N = 28). Fibrosis was described using the histological Ishak scoring system.

6.2.2 *MRI data acquisition*

All participants underwent one MR imaging session on a 3 T scanner (Siemens Trio, Siemens Healthcare, Erlangen, Germany), after a 4 hour fast. ShMOLLI T_1 maps, 2D multiple-echo GRE images to quantify T_2^* and SVS STEAM spectroscopy to quantify liver PDFF were collected. Sequence parameters of the shMOLLI acquisition were: FOV = 200–300 × 350–380 mm², matrix 192 × (106–192) matrix, FA = 35°, TR/TE=2.45/0.97–1.05 ms, BW = 898 Hz/px, TI = 110–120, 190–200, 270–290, (110–120)+k × RR ms ($k = \overline{1, 4}$), slice thickness 8 mm, phase encoding direction anterior-posterior, 24 k-space lines before the centre of k-space, 66 total k-space lines acquired, GRAPPA acceleration factor 2, partial Fourier factor 6/8 in the phase encoding direction. The 2D multiple-echo GRE sequence used the following parameters: FOV = 200–300 × 350–380 mm², matrix 192 × (108–186), FA = 20°, TR/TE = 600/2.48, 7.38, 12.3, 17.22, 22.14 ms, phase encoding direction anterior-posterior, BW = 389 Hz/px, bipolar gradient readout scheme and slice thickness 8 mm. The ECG-

triggered SVS STEAM acquisition used TR_{min} = 2 s for water-suppressed measurements with 5 repetitions and TR_{min} = 4 ms for non-water-suppressed measurements with 3 repetitions; other parameters were: TE = 10 ms, TM = 7 ms, voxel size was 20 × 20 × 20 mm^3.

6.2.3 *Data analysis*

T_2^* values were derived by fitting the magnitude GRE images to equation 6.1.

$$S(TE) = S_0 e^{-TE/T_2^*} \tag{6.1}$$

Spectroscopic data was fitted using the OXSA toolbox [143] implementation of the AMARES algorithm [142] with an in-house MATLAB (The Mathworks, Natick, MA, USA) script [132]. PDFF of the liver was determined as the ratio of the sum of all fat peak amplitudes to the sum of all fat peak amplitudes plus the water peak amplitude and it was corrected for T_2 effects mediated by iron.

Iron-corrected shMOLLI T_1s (cT_1) were determined using a method described by Tunnicliffe et al. [14], while fat- and iron-independent water shMOLLI T_1s (fcT_1) were determined using the algorithm described in chapter 5. Correcting for the effects of off-resonance frequencies was not possible as the multiple-echo GRE data sets only contained magnitude data. Since both lobulitis and ballooning scores were available in the examined patient cohort, their influence on the variability of T_1 values within Ishak scores was also evaluated.

6.2.4 *Statistical analysis*

To assess the performance of removing the effects of iron and fat, Spearman's rank correlation coefficients were calculated between Ishak fibrosis scores and determined cT_1 and fcT_1 values, respectively, for three groups: all participants, participants with $PDFF_{liver}$ < 10%, and participants with $PDFF_{liver} \geq 10\%$. Correlation between Ishak fibrosis stage and

T_1 values was also evaluated in a subgroup of patients with NAFLD as the primary aetiology. Multiple-comparison ANOVA with Bonferroni correction was performed to assess differences between Ishak fibrosis stages after iron-correction and after removing the effects of iron and fat. Dependence of measured shMOLLI T_1 (mT_1) and residual dependence of iron-corrected and iron- and fat-independent shMOLLI T_1 values on iron and PDFF was assessed using Pearson's correlation coefficient.

6.3 RESULTS

Table 6.1 summarises baseline characteristics of the 28 participants, out of which 12 had $PDFF_{liver} < 10\%$ and 16 had $PDFF_{liver} \geq 10\%$. Removing the effects of fat in addition to the effects of iron increased the correlation of water shMOLLI T_1 values with Ishak scores, as reflected by Spearman's correlation coefficients in table 6.2. Figure 6.1 shows a breakdown of the effect of different correction methods on the original shMOLLI T_1 data, grouped by Ishak fibrosis stage. Iron- and fat-independent water shMOLLI T_1 values were significantly different between Ishak fibrosis stages 0 and 1 ($p = 0.025$), 1 and 3 ($p = 0.002$), 1 and 6 ($p < 10^{-3}$), 2 and 6 ($p = 0.002$), and 3 and 6 ($p = 0.034$), respectively, when considering the entire patient cohort. Figure 6.2 shows the dependence of measured shMOLLI T_1 and residual dependence of iron-corrected, and iron- and fat-independent water shMOLLI T_1 on liver PDFF. While measured (Pearsons's ρ = -0.049, $p = 0.805$) and iron-corrected (Pearson's $\rho = 0.131$, $p = 0.508$) shMOLLI T_1 values did not show significant dependence on PDFF, there was a significant relationship between iron- and fat-independent water shMOLLI T_1s and liver PDFF (Pearson's ρ = -0.571, $p = 0.002$). It should be noted, that after removing the effects of iron and fat, the higher shMOLLI T_1 values corresponded to patients with higher Ishak stage of fibrosis, who generally also tend to present lower concentrations of fat.

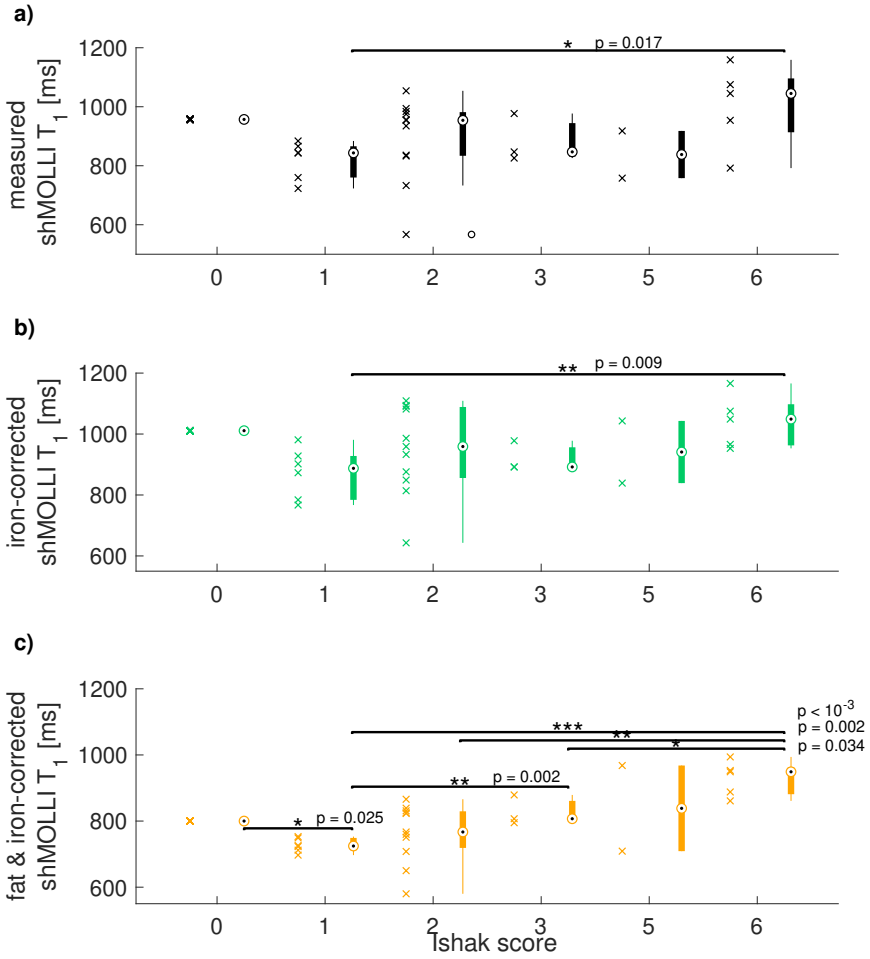

Figure 6.1: Box plots comparing measured (a), iron-corrected (b), and iron- and fat-independent water shMOLLI T_1 values (c) with Ishak fibrosis stages. Individual T_1 values within each fibrosis stage are shown next to boxplots. None of the participants had histology corresponding to an Ishak 4 stage.

Compared to measured shMOLLI T_1 values (Pearson's ρ = -0.685, p = 5.8×10^{-5}), dependence on HIC was reduced in both iron-corrected (Pearson's ρ = -0.393, p = 0.039) and iron- and fat-independent shMOLLI T_1 (Pearson's ρ = -0.511, p = 0.006), but correlation with T_1 values was still significant. Figure 6.3 shows the distribution of lobulitis and ballooning scores within Ishak fibrosis stage groups. Due to the low number of patients with scores of 0 and 2 in either lobulitis or ballooning, it was not possible to assess whether higher scores introduces larger variability in the distribution of T_1 values within Ishak stage groups.

Table 6.1: Baseline characteristics of the 28 participants included in the retrospective analysis

	Mean	SD	Range
Males:Females	18:10		
Age (yr)	50	15.00	26–78
Weight (kg)	88	24.00	45–128
BMI ($kg\,m^{-2}$)	29.30	6.40	17.10–45.40
PDFF (%)	11.75	5.13	5.58–24.88
HIC (mg/g dry weight)	1.23	0.39	0.45–2.09
Ishak fibrosis stage	N	%	
0	1	3.57	
1	6	21.43	
2	11	39.28	
3	3	10.72	
4	0	0.00	
5	2	7.14	
6	5	17.86	
Aetiology	N	%	
NAFLD	16	57.14	
HBV	1	3.57	
HCV	5	17.86	
ASH	6	21.43	

6.4 DISCUSSION

This chapter aimed to retrospectively apply the combined iron- and fat-correction algorithm to a cohort of a prospectively acquired clinical research study. Assuming that liver shMOLLI T_1 is a biomarker of hepatic fibrosis, one of the desired outcomes of the retrospective analysis

Table 6.2: Spearman's rank correlation coefficients between Ishak fibrosis stages and measured, iron-corrected, and fat- and iron-independent water shMOLLI T_1 values

	ρ	p
$PDFF_{liver} \geq 5\%, n = 28$		
mT_1	0.283	0.144
cT_1	0.307	0.112
fcT_1	0.640	<0.001
$5\% \leq PDFF_{liver} < 10\%, n = 12$		
mT_1	0.598	0.039
cT_1	0.786	0.002
fcT_1	0.799	0.001
$PDFF_{liver} \geq 10\%, n = 16$		
mT_1	0.154	0.570
cT_1	0.154	0.570
fcT_1	0.208	0.440
NAFLD group, n = 16		
mT_1	0.003	0.991
cT_1	0.194	0.471
fcT_1	0.543	0.030

was the assessment of the performance of the algorithm by evaluating the correlation between resulting T_1 values and histologically-determined Ishak fibrosis stage. Since only liver PDFF > 5% is considered clinically relevant, this study only focused on participants whose liver PDFF fell into that region.

Although determining the iron- and fat-independent water shMOLLI T_1 values generally reduced the variance in individual Ishak fibrosis stage groups and improved the overall correlation with Ishak fibrosis stage, this correlation was not statistically significant in the

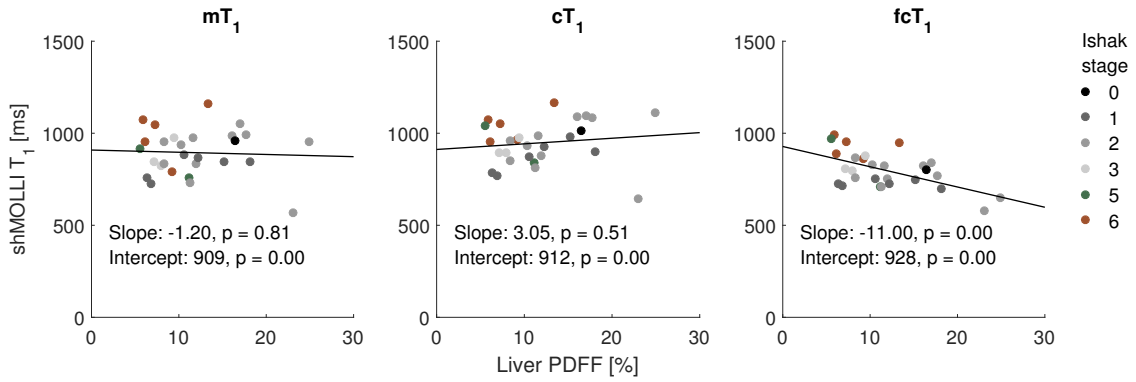

Figure 6.2: Relationship between measured, iron-corrected, and iron- and fat-independent water shMOLLI T_1 and liver PDFF. Columns correspond to measured, iron-corrected and iron- and fat-independent water shMOLLI T_1

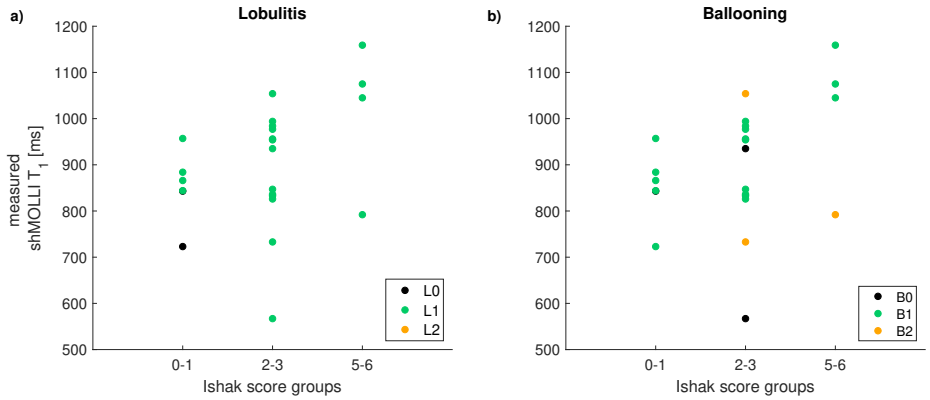

Figure 6.3: The distribution of lobulitis (a) and ballooning (b) scores in Ishak stage groups. The majority of patients were diagnosed with a score of 1 for both lobulitis and ballooning.

subgroup presenting liver PDFF > 10%. Additionally, cT_1 values did not show a marked dependence on liver PDFF, as it was expected based on observations from chapter 4 and existing literature [122, 156] and still had a significant dependence on iron concentration. Consequently, the iron- and fat-independent water shMOLLI T_1 values showed significant dependence both on liver PDFF and iron concentration, leading, in some cases, to an over-correction of shMOLLI T_1 values. The unexpected dependence of corrected T_1 values (cT_1 or fcT_1) on iron and fat, respectively, might be due to using a biased calibration curve between T_2^* and HIC values, as calibration curves available in the scientific literature were

derived from studies covering a wide range of iron concentrations, while the HIC values in the current study are only covering a small subset of the usual range. It is, therefore, possible that iron concentrations derived in this study are underestimating real HIC values, which, in turn, causes an overestimation of iron-corrected liver PDFF values leading to an over-correction of fat effects in shMOLLI T_1 values.

Differences between parameters of the simulated shMOLLI sequence and the actual sequence parameters used during data acquisition (e.g. bSSFP repetition time, inversion and excitation pulse shapes) along with off-resonance effects might also influence estimated cT_1 and fcT_1 values.

Another possible mechanism driving the over-correction of fat effects might be a non-linear relationship between liver PDFF and extracellular fluid volume. There is evidence suggesting that increasing amounts of fat cause a reduction in the number of hepatocytes and hepatic lobules, however, this effect saturates at approximately 20% fat proportionate area at the expense of extracellular space [157]. The water shMOLLI T_1 determination algorithm would benefit from the characterisation of this phenomenon.

6.5 CONCLUSIONS

In conclusion, the suggested iron- and fat-independent water shMOLLI T_1 determination algorithm did improve the correlation of shMOLLI T_1 and Ishak fibrosis stages, but needs further development. For instance, it does not account for inflammation in the liver, which is the hallmark of NASH, also a wide-spread chronic liver disease but is a characteristic of viral hepatitis too. In addition to having a realistic model of the liver, it is also of great importance to have reliable readings of liver T_2^* and liver PDFF values, as well as having an off-resonance frequency reading. The effects of frequency offsets are especially important to

counter-balance in studies that have been conducted without careful setup of the shMOLLI protocol with respect to choosing a combination of TR and TE that allows a minimal dependence on off-resonance frequencies.

While having a retrospective correction algorithm can prove useful, it might be more efficient to have a sequence developed that provides water-only T_1 maps without the need for complex biophysical models of the imaged tissue. In this context, methods employing fat suppressed inversion recovery or multiple-echo Dixon imaging with inversion recovery (mDIXON-IR) might be good alternatives. mDIXON-IR in particular would offer a more reliable fat-water separation than a fat-suppressed sequence and frequency-dependence could further be reduced using non-bSSFP readout schemes.

7

The influence of liver glycogen concentration and body hydration status on liver T_1 measurements

7.1 INTRODUCTION

ShMOLLI T_1 measurements of the liver can be useful for characterising disease and predicting disease outcomes, as described in previous chapters. However, there still is an unexplained variance in the liver shMOLLI T_1 of healthy volunteers when compared to myocardial shMOLLI T_1 values of healthy individuals: σ^2_{liver} = 2401 ms² [13] vs $\sigma^2_{myocardium}$ = 625 ms² [158]. This difference between the two organs suggests that there are effects unaccounted for when performing shMOLLI measurements in the liver.

It has been previously shown that pre-menopausal women have elevated liver T_1 times in comparison with post-menopausal women and men [111], most probably due to hormonal

changes that affect the overall fluid balance of the body. Additionally, women actively using contraceptive pills also had elevated T_1 values [111]. Gore et al. have shown that glycogen concentration shortens both T_1 and T_2 relaxation times [159], an effect likely to be caused by the viscosity of the glycogen macromolecule. Hydration status has been previously proven to influence T_1 times of the brain [160], therefore it is reasonable to assume that it would also have an impact on liver T_1 values, since the liver is exposed to variations in fluid balance. Of the aforementioned effects glycogen stands out as one that can vary most across a mixed cohort of healthy participants. Glycogen is stored in the liver and in skeletal muscle and serves as an energy deposit, comprising glucose residues. Simplistically, when blood glucose levels decrease, glycogen in the liver is broken down in a process called glycogenolysis. Glucose is then released in the blood stream. During glycogenesis, glycogen is built up from ingested food. The metabolic cycle regulating glycogen synthesis and degradation is presented in fig. 7.1 [161].

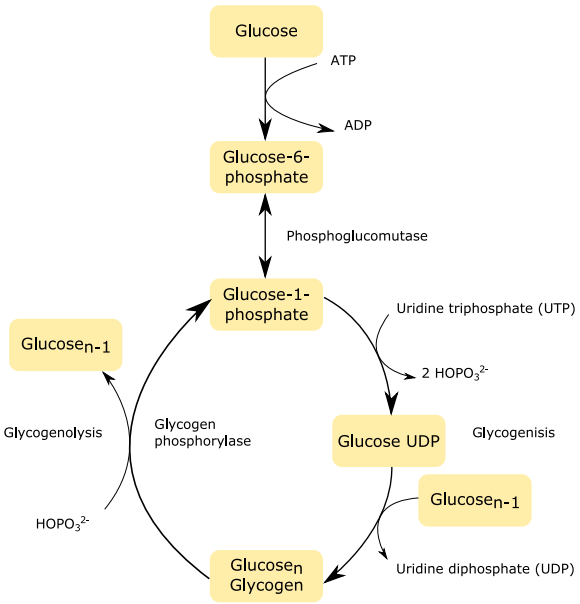

Figure 7.1: Metabolic pathways describing the synthesis (glycogenesis) and degradation (glycogenolysis) of glycogen.

Both liver glycogen concentration and body hydration status can experience significant diurnal variation, and, therefore, can be easily influenced by nutritional interventions. Thus, the aim of this chapter is to explore the effect of these two variables on liver shMOLLI T_1 measurements.

7.2 METHODS

7.2.1 Phantom experiments

Twelve phantoms were built with varying concentration of oyster glycogen (Sigma Aldrich, UK) dissolved in deionised water. Phantoms were stored in 30 ml universal sample containers (King Scientific, UK). Glycogen was dissolved in 25 ml of water to form solutions of 0% to 11% by weight in steps of 1% by weight.

Phantoms were then scanned in a 37°C water bath both in a 1.5 T Avanto Fit and a 3T Prisma scanner (Siemens Healthcare, Erlangen, Germany). 8 elements of a 32-channel spine array coil and 6 elements of an 18-channel flexible coil were used. Turbo spin echo inversion recovery (TSE-IR) and MCSE images were collected on both scanners. Sequence parameters for the TSE-IR sequence were: FOV = 135 × 180 mm², matrix 144 × 192, TI = 50, 100, 200, 400, 800, 1600, 2400, 3200 ms, TR = 9000 ms, TE = 12 ms, slice thickness 6 mm, turbo factor 4. The MCSE sequence used the following parameters: FOV = 187 × 187 mm², matrix 128 × 128, TR = 9000 ms, TE_{min} = 15 ms, echo spacing 15 ms, number of echoes 32 , slice thickness 6 mm. Individual TSE-IR images were fitted to eq. 7.1, while MCSE images were fitted to eq. 7.2 to obtain T_1 and T_2 maps, respectively.

$$S(TI) = S_0(1 - 2e^{-TI/T_1} + e^{-TR/T_1}) \tag{7.1}$$

$$S(TE) = S_0 e^{-TE/T_2} \tag{7.2}$$

In these equations S_0 represents the signal at TI = 0 ms and TE = 0 ms, respectively.

R_1 (=1/T_1) and R_2 (=1/T_2) measurements were then fitted to eq. 7.3 to obtain longitudinal and transverse relaxivities of glycogen at 1.5 T and 3 T. Here, $R_{1,2}$ represent longitudinal and transverse relaxation rates, $R_{1,20}$ are relaxation rates in the absence of glycogen, $r_{1,2}$ are relaxivity values of the glycogen and g is the concentration of glycogen.

$$R_{1,2} = R_{1,20} + r_{1,2}g \tag{7.3}$$

7.2.2 Pilot human experiments

One athletically active healthy volunteer was enrolled in a pilot study aimed to explore the effects of glycogen on liver shMOLLI T_1 maps. The subject was scanned on eight different days: four scans were performed in a fed state and four in a fasted state. The average time between fed and fasted scans was two days. The fasted state was reached after a twelve-hour overnight fasting and two hours of cycling exercise; during this period the participant was allowed to consume water. The fed state was achieved after consuming a high-calorie, high-carbohydrate meal for lunch and having a three-hour rest to allow glycogen build-up in the liver of the participant.

Scans were performed on a 3 T Prisma imager (Siemens Healthcare, Erlangen, Germany). 8 elements of a 32-channel spine array coil and 12 elements of an 18-channel body flexible array coil were used. ShMOLLI T_1 maps were collected during each scan. Multiple-echo GRE images were also collected to make sure that the participant's hepatic iron and lipid concentrations were normal (HIC $\leqslant$ 1 mg/g Fe dry weight [14] and PDFF $\leqslant$ 5 % [29,79,162]). The shMOLLI acquisition followed a standardised protocol: FOV = 331 × 248 mm², matrix

144 × 192, TR/TE = 2.48/1.05 ms, TI = 100, 180, 260, 100 + k× RR ms (k=$\overline{1, 4}$) slice thickness 8 mm, BW = 1302 Hz/px, bSSFP FA = 35°, phase encoding direction anterior-posterior, 24 k-space lines before the centre of k-space, 66 total k-space lines acquired, GRAPPA acceleration factor 2, partial Fourier factor 6/8 in the phase encoding direction. The approach to steady state was achieved using 5 LISA pulses [26, 27] and it was interrupted by a half-angle ramp down pulse [163]. The 2D multiple-echo GRE sequence used the following parameters: FOV = 331 × 248 mm², matrix 128 × 104, FA = 6°, TR/TE = 22.2/1.25, 2.46, 3.69, 4.92, 6.15, 7.38, 8.61, 9.84 ms, phase encoding direction anterior-posterior, BW = 1260 Hz/px, bipolar gradient readout scheme and slice thickness 6 mm.

Two healthy volunteers were enrolled in a different pilot study aimed to assess the impact of changes in overall body hydration status on liver shMOLLI T_1 maps. Subjects were scanned using the same scanner, same coils, and same sequences as described in the previous paragraph. Each volunteer consumed 1.5 l of isotonic water while in the scanner followed by a shMOLLI acquisition at 5 minute intervals for approximately 1 hour. Liver and erector spinae muscle shMOLLI T_1 values were recorded every 5 minutes before and after water consumption. The muscle was chosen as a control organ against which the evolution of liver T_1 was compared, assuming that only a small increase of extracellular water will be observable in the muscle, as opposed to the liver. Since the inferior vena cava is known to distend as a response to hydration, but the aorta is not affected by hydration, the ratio of the cross-sectional area of the inferior vena cava and the aorta (IVC/Ao ratio) was also calculated from bSSFP images every 5 minutes before and after the water consumption to serve as a surrogate marker of body hydration status.

7.2.3 *Multi-participant study*

7.2.3.1 *Protocol*

Based on the results of the two pilot studies described in the previous subsection, a larger study was designed. Ethical approval was sought and received from the Central University Research Ethics Committee (reference: R55780/RE001). Participants underwent five MRI examinations during the study:

1. After a standardised, high-calorie (1000 kcal), high-carbohydrate meal, to measure liver T_1 when glycogen levels are expected to be high and hydration status is expected to be normal (participants were in an *euvolaemic fed* state);

2. After a 12-hour long overnight fast, to measure T_1 when glycogen levels are expected to be low (typically by 40-50% compared to baseline levels [164]; participants were in a *low glycogen fasted* state);

3. After a 2-hour long stationary bicycle exercise session with an effort corresponding to a score of 6 on the modified Borg scale for perceived exertion [165], to measure T_1 when glycogen is expected to be close to depletion (participants were in a *depleted glycogen fasted* state);

4. After another standardised, high-calorie (1000 kcal), high-carbohydrate meal, a 12-hour long overnight fast, and 3 hours of dehydration, to measure T_1 at moderate amounts of glycogen and lower-than-normal hydration levels (participants were in a *hypovolaemic* state);

5. After the consumption of 1.5 l of isotonic water, to measure T_1 at a high hydration level (participants were in a *hypervolaemic* state).

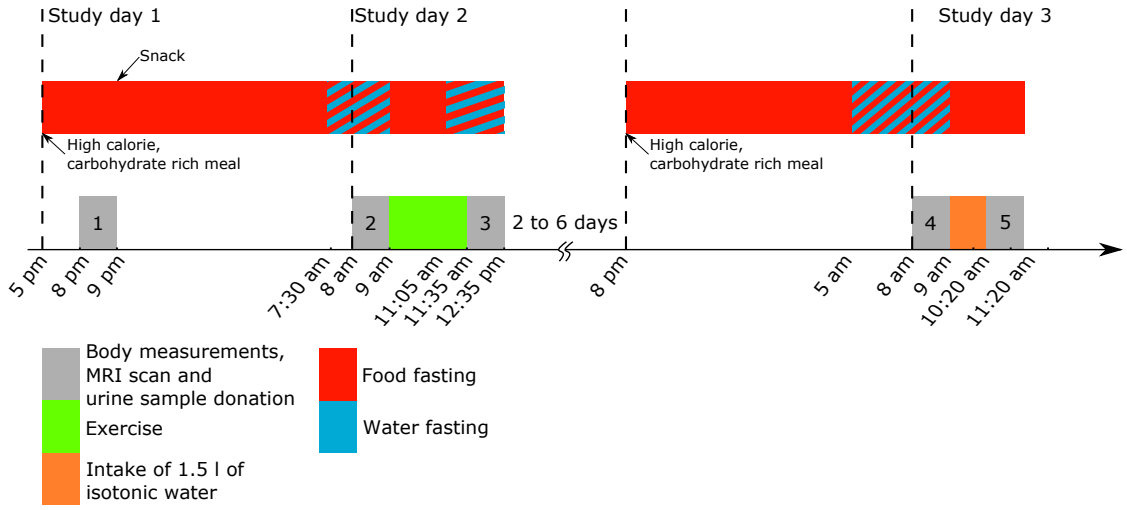

Figure 7.2: Timing of study procedures for a single volunteer. Numbers in grey boxes (for MRI scans) correspond to the following physiological states: high-glycogen, high hydration - euvolaemic fed (1), low glycogen - fasted (2), depleted glycogen - fasted (3), low glycogen, low hydration - hypovolaemic (4), and low glycogen, high hydration - hypervolaemic (5), as described in subsection 7.2.3.1.

The timing chart of study visits is shown in fig. 7.2.

The primary objective of the study was to characterise the change in liver shMOLLI T_1 values resulting from a change in liver glycogen concentration in healthy individuals. The secondary objective was to characterise the change in liver shMOLLI T_1 values resulting from a change in body hydration status in healthy individuals. Inclusion and exclusion criteria are summarised in table 7.1.

7.2.3.2 Data acquisition and analysis

Glycogen concentration was measured using non-localised, natural abundance ^{13}C spectroscopy and concentration values were obtained using the phantom replacement method [166]. For this, a phantom containing 300 mM glycogen and 1.36 mM $NiCl_2$ was prepared in 1 l of phosphate-buffered solution. Sequence parameters of the ^{13}C spectroscopy were: TR/TE = 400/0.6 ms, number of averages 2504, no decoupling, rectangular pulse of τ_p = 1 ms length, FA=90°, BW = 10 kHz, acquisition delay 0.1 ms, vector size 512 samples.

Table 7.1: Inclusion and exclusion criteria for the glycogen-hydration study

Inclusion criteria
Candidate is a healthy adult, aged 20 to 50 years
BMI between 18 kg/m² and 30 kg/m²
Candidate is willing to donate four urine samples after the last four MRI scans
Candidate enjoys (or has enjoyed in the past) sports activities
Exclusion criteria
Self-reported liver, kidney, heart or lung disease or diabetes
Regular consumption of alcohol, exceeding 14 units per week
Presence of metallic implants, pacemakers
Pregnancy
In case of female candidate: the use of oral contraceptive in the past 3 months
Any other conditions rendering the candidate unsuitable for an MRI scan

The shMOLLI T_1 acquisition was the same as described in subsection 7.2.2, but a different multiple-echo GRE sequence was used to quantify PDFF and T_2^* values: FOV = 331 × 248 mm², matrix size 128 × 96, TR/TE =17/0.94, 2.28, 3.60, 4.92, 6.24, 7.56, 8.88, 10.20, 11.52, 12.84, 14.16, 15.48 ms, FA = 3°, phase encoding direction anterior-posterior, BW = 1560 Hz/px, monopolar gradient readout scheme, and slice thickness 10 mm. PDFF and T_2^* values were obtained using the T_2^*-IDEAL algorithm [139, 140].

To quantify liver volumes, a multislice 3D FLASH sequence was used with sequence parameters: FOV 308 × 380 mm², matrix size 195 × 320 × (60-64), FA=9°, TR/TE = 3.97/1.29, 2.52 ms, BW = 1040 Hz/px, and slice thickness 3 mm.

Urine samples were used to measure urine osmolality, an indicator of urine concentration, in order to assess hydration status [167]. Additionally, IVC/Ao ratio [168, 169], body weight, liver volume and blood T_1 were also considered as indicators of hydration status.

Blood T_1 is known to correlate well with haematocrit level [158,170], which, in turn, is a good predictor of dehydration [171]. Liver volumes were calculated from the stack of volumteric interpolated breath-hold examination (VIBE) images by taking three linear measurements of the liver: cranio-caudal (CC), latero-lateral (LL), and antero-posterior (AP) maximum distances, as described in [172]; the liver volume was then approximated using equation 7.4.

$$V_{liver} = CC \times LL \times AP \times 0.31 \tag{7.4}$$

IVC/Ao ratio, body weight and liver volume were assumed to correlate with changes in extracellular fluid in the liver, while liver volume was also considered a predictor of hepatic intracellular fluid.

Liver shMOLLI T_1 values were determined as the average T_1 over three ROIs placed in the liver such that they avoided the edge of the liver, vessels and bile ducts. Two ROIs were placed in the right lobe, one posteriorly and one anteriorly, and one ROI was placed in the left lobe, an example of ROI placement being shown in fig. 7.3. Since all participants were healthy volunteers and liver PDFF levels were typically below 3%, fat correction was not performed. As frequency variation over the liver was in the -20–20 Hz range, corresponding to a variation of less than 10 ms in measured shMOLLI T_1s, according to fig. 4.1, frequency correction was also considered unnecessary.

7.2.4 Statistical analysis

A paired t-test was used to determine the significance of shMOLLI T_1 change in the pilot study concerning the effects of glycogen, as well as for comparing change in shMOLLI T_1 values, glycogen concentrations and IVC/Ao ratios between fed and fasted states and hypovolaemic and hypervolaemic states. Data were fitted to linear mixed models (LMM) to derive a relationship between shMOLLI R_1 measurements, body weight, liver volume,

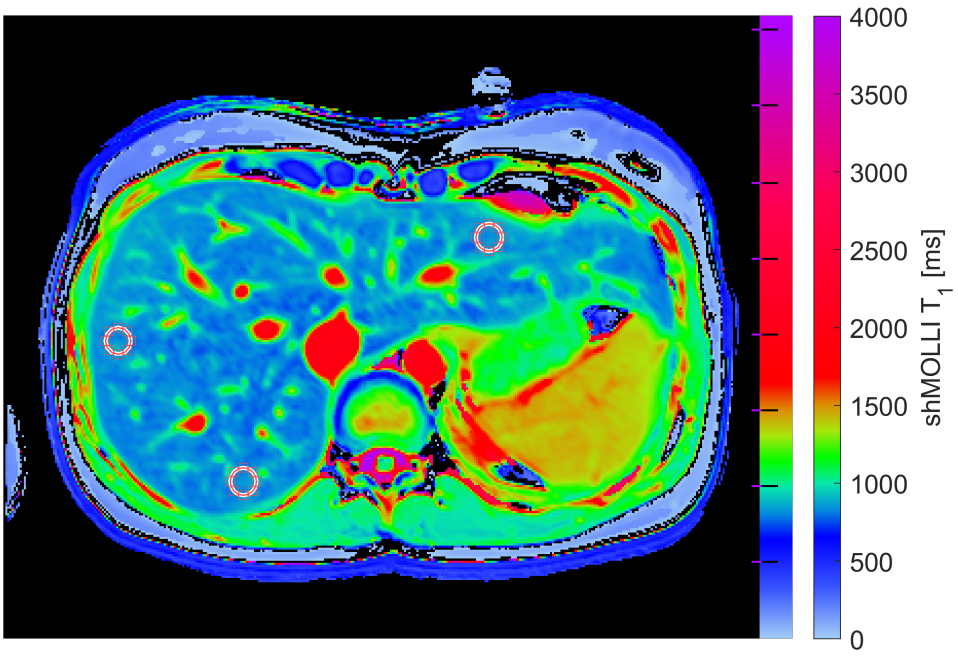

Figure 7.3: Typical placement of ROIs: two in the right lobe and one in the left lobe.

liver glycogen concentration, and body hydration status markers. LMMs were chosen over simple linear models due to the presence of repeated measures in the data set necessitating the inclusion of random effects. The intra-subject correlation of shMOLLI R_1 values was considered as a random effect and a random intercept per participant (i.e. an intercept for each participant was determined by the model to accommodate for the different baseline T_1s in each participant) was introduced in the LMMs.

A Shapiro-Wilk test was used to evaluate whether model residuals belonged to a normal distribution.

For all statistical tests an $\alpha = 0.05$ significance level was considered.

7.3 RESULTS

7.3.1 *Phantom experiments*

Phantom R_1 and R_2 values showed linear dependence on glycogen concentration at both 1.5 T and 3 T, as shown in fig. 7.4. Longitudinal and transverse relaxivities are shown in table 7.2.

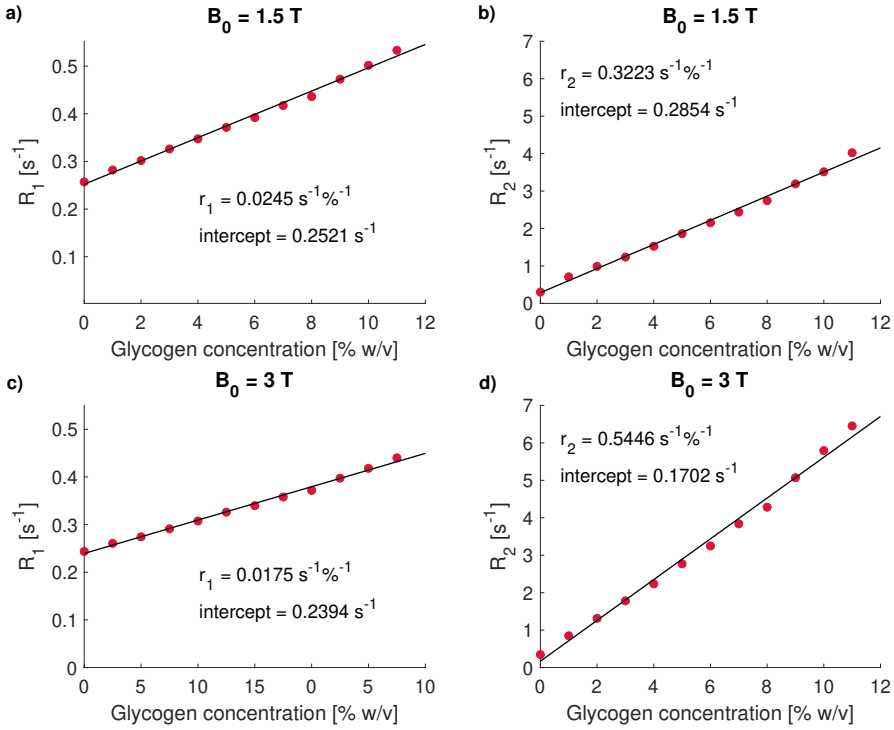

Figure 7.4: Transverse and longitudinal relaxation rates in glycogen phantoms had a linear dependence on glycogen concentration at both 1.5 T and 3 T.

Table 7.2: Longitudinal and transverse relaxivities of glycogen determined by spin echo experiments at 1.5 T and 3 T, as given by eq. 7.3.

B_0 [T]	r_1 [%$^{-1}$s^{-1}]	r_2 [%$^{-1}$s^{-1}]
1.5	0.0245 ± 0.020	0.3223 ± 0.027
3	0.0175 ± 0.001	0.5446 ± 0.051

7.3.2 *Human experiments*

7.3.2.1 *Pilot studies*

Figure 7.5 shows the results of the glycogen experiment. A mean increase of 34.5 ms was observed between the fed and the fasted state, although the volunteer did confess to a 40 km bicycle time trial the night before the outlier data point in the fed group was collected, suggesting that glycogen concentration might not have been as high as expected. Liver

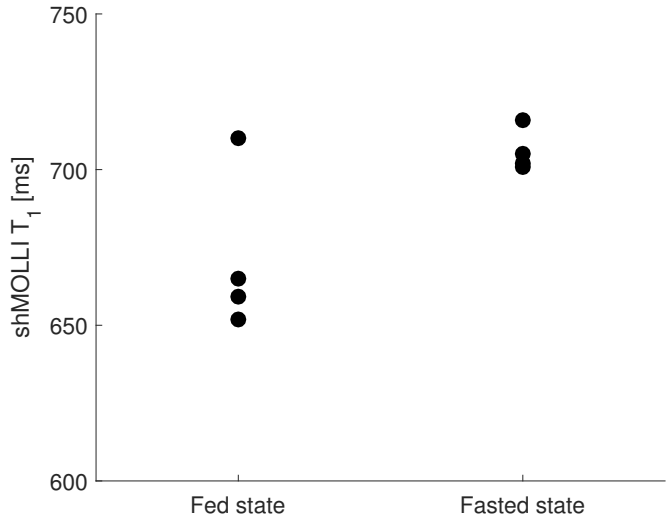

Figure 7.5: An increase in shMOLLI T_1 was observed from the fed state to the fasted state

shMOLLI T_1 increased after the 1.5 l isotonic water intake for approximately 25 minutes, reaching a maximal increase of 65 ms compared to the baseline shMOLLI T_1 value of 677 ms. ShMOLLI T_1 was still 23 ms longer than baseline T_1 60 minutes post-water administration. IVC/Ao ratio increased and reached a steady-state value 15 minutes after water intake, peaking at 1.5, even after 60 minutes post-water administration. Erector spinae shMOLLI T_1 increased steadily after water ingestion. Figure 7.6 shows the time evolution of liver and erector spinae shMOLLI T_1s, and the IVC/Ao ratio for a single participant.

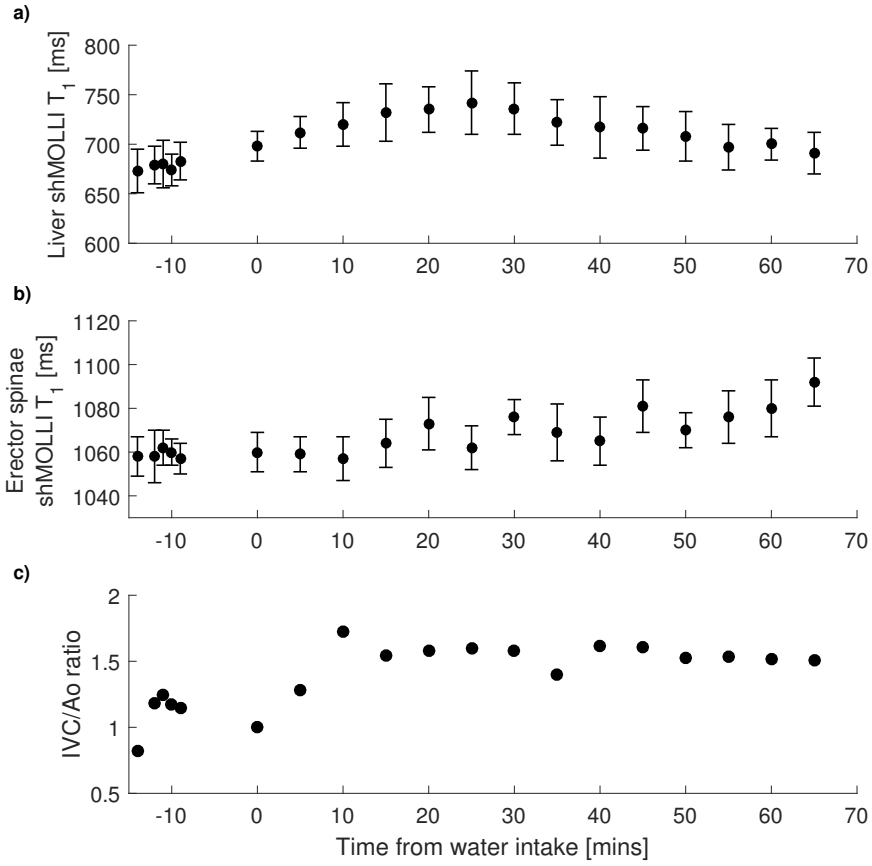

Figure 7.6: Time evolution of liver (a) and erector spinae (b) shMOLLI T_1s, and of IVC/Ao ratio (c) after a 1.5 l isotonic water intake in one of the subjects

7.3.2.2 Multi-participant study

Eight participants were included in the study (3 female) with a mean age of 31±7 years. The participants had mean height, weight and BMI of 176±6 cm, 74.6±10.0 kg and 23.8±2.7 kg/m², respectively. Urine osmolality measurements were found not to correlate significantly with IVC/Ao ratios ($r = -0.045$, $p = 0.806$), however, IVC/Ao ratio correlated with the shMOLLI T_1 of venous blood ($r = 0.503$, $p < 0.001$), as measured in the IVC.

When comparing the high glycogen fed and low glycogen fasted states, both shMOLLI T_1 and liver glycogen concentration values were significantly different in the two states ($p =$

0.004 for shMOLLI T_1 and $p < 0.001$ for glycogen concentration), however, IVC/Ao ratios were not significantly different ($p = 0.337$). While both glycogen concentration and IVC/Ao ratios were significantly different between hypovolaemic and hypervolaemic states ($p = 0.023$ for glycogen concentration and $p = 0.048$ for IVC/Ao ratio), no significant change was observed in shMOLLI T_1 measurements ($p = 0.103$). A graphical representation of the relationships between fed and fasted and hypovolaemic and hypervolaemic states is shown in fig. 7.7.

Two multivariable LMMs were tested against the collected data, as described by equations 7.5a and 7.5b, where β_I, β_G, β_{WI}, and β_{GV} correspond to estimates of predictor variable coefficients for IVC/Ao ratio, glycogen concentration, body weight-IVC/Ao interaction term, and glycogen concentration-liver volume interaction term. b_{oi} are subject-specific intercepts from a normal distribution of zero mean and σ_o^2 variance, while ϵ_i are subject-specific errors from a normal distribution of zero mean and σ_e^2 variance. ShMOLLI R_1 was considered as the observed variable and was denoted by y. Per-subject measurements are denoted by i and within-subject measurements are denoted by j.

$$y_{ij} = \beta_o + \beta_G[Glyco]_{ij} + \beta_I IVC/Ao_{ij} + b_{oi} + \epsilon_i$$
$$b_{oi} \sim \mathcal{N}(0, \sigma_o^2), \epsilon_i \sim \mathcal{N}(0, \sigma_e^2), i = \overline{1,8}, j = \overline{1,5} \tag{7.5a}$$

$$y_{ij} = \beta_o + \beta_G[Glyco]_{ij} + \beta_I IVC/Ao_{ij} + \beta_{WI} Weight_{ij} IVC/Ao_{ij} + \beta_{GV}[Glyco]_{ij} Volume_{ij} + b_{oi} + \epsilon_i,$$
$$b_{oi} \sim \mathcal{N}(0, \sigma_o^2), \epsilon_i \sim \mathcal{N}(0, \sigma_e^2), i = \overline{1,8}, j = \overline{1,5} \tag{7.5b}$$

Model #1 (eq. 7.5a) is the result of a naïve conclusion based on the initial hypothesis that shMOLLI R_1 is affected by both liver glycogen concentration and body hydration level as described by the IVC/Ao ratio. Model #2 (eq. 7.5b) extends both the glycogen and hydration part of model #1 with an interaction term each. The interaction between glycogen

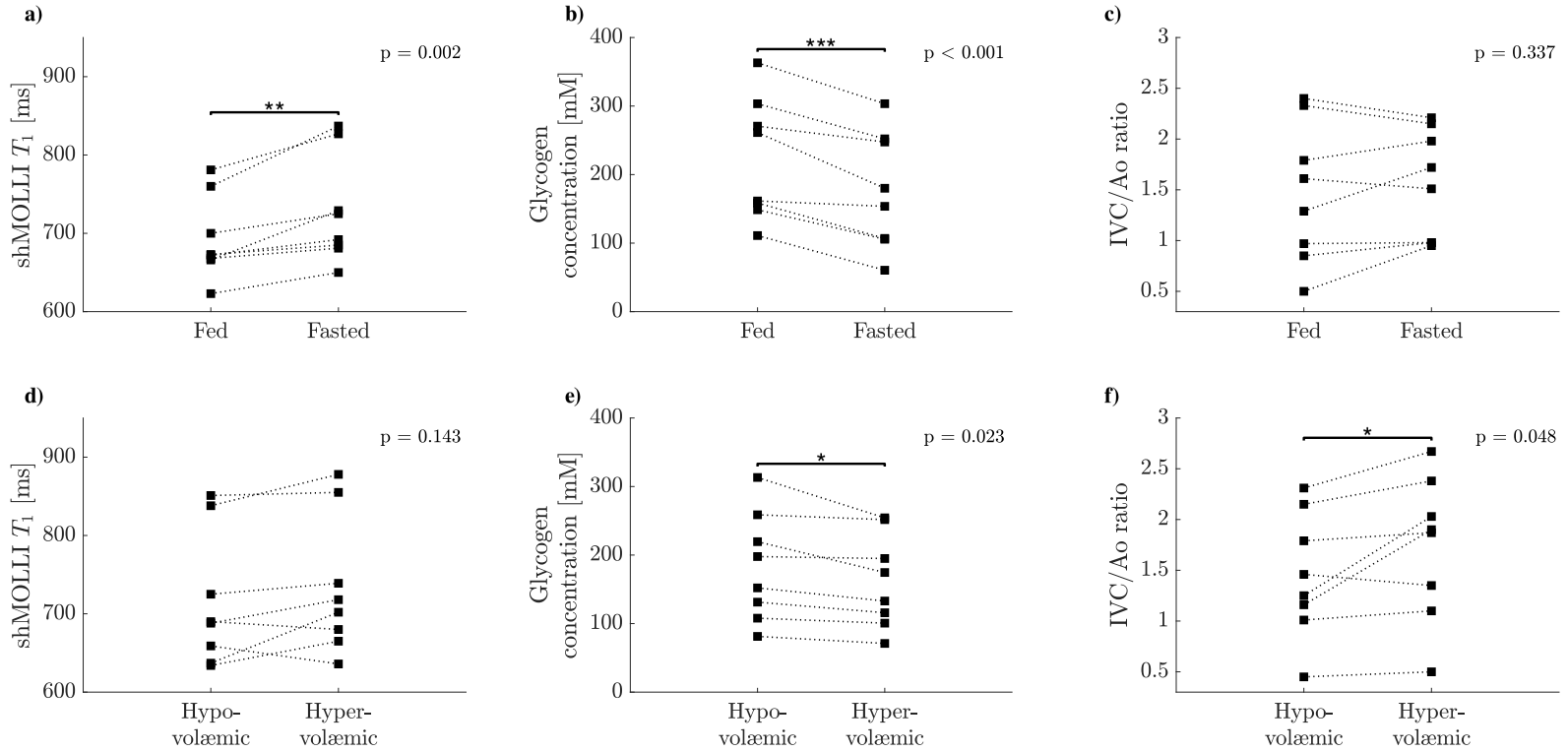

Figure 7.7: Changes in shMOLLI T_1, glycogen concentration and IVC/Ao ratio between the fed and fasted states (a-c, corresponding to states 1 and 2 on fig. 7.2) and between hypovolaemic and hypervolaemic states (d-f, corresponding to states 4 and 5 on fig. 7.2)

concentration and liver volume in this model can be interpreted as a reduction of the effects of glycogen alone due to using the same surface coil over a larger liver volume. Changes in IVC/Ao ratio can be translated into variation of the extracellular vascular water compartment, while changes in body weight carry information about changes in both intracellular and extracellular water. An interaction between the IVC/Ao ratio and body weight would thus reduce the effect size of the IVC/Ao ratio on shMOLLI R_1, since shMOLLI R_1 is especially sensitive to extracellular volume [14]. The outcomes of the two LMMs are summarised in table 7.3 along with the variance of the fitting residuals. The variance of the original shMOLLI R_1 values was $\sigma^2_{R_1} = 0.018\ s^{-2}$. The residuals of the fitted LMMs were evaluated to assess the assumptions of the models. For this, lag plots of the residuals were built, as shown in fig. 7.8. Shapiro-Wilk tests of the residuals did not reject the null-hypothesis that the residuals were belonging to a normal distribution ($p = 0.940$ for both models).

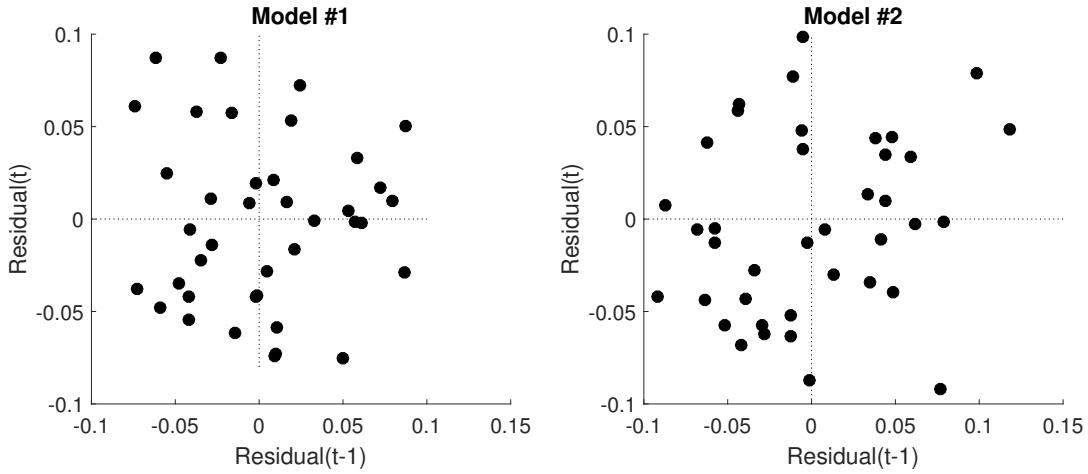

Figure 7.8: Lagged plots of residuals for the two LMMs considered in this study. Both residuals of model #1 (eq. 7.5a) and model #2 (eq. 7.5b) show a random pattern or at least one that does not show a significant correlation.

Table 7.3: Results of the two regression models. Random intercepts are characterised by their standard deviation and represent the intercept determined for each participant, i.e. the baseline for each participant undergoing repeated measurements.

	β	SE	p	Residual variance
Multivariable LMM #1				
Intercept [s^{-1}]	1.433	0.059	< 0.001	
Random intercept [s^{-1}]		σ_0 = 0.096		0.0022
IVC/Ao [s^{-1}]	-0.049	0.030	0.109	
[Glyco] [$M^{-1}s^{-1}$]	0.285	0.174	0.110	
[$\%^{-1}s^{-1}$]	0.005			
Multivariable LMM #2				
Intercept [s^{-1}]	1.411	0.031	$< 10^{-8}$	
Random intercept [s^{-1}]		$\sigma_0 = 5.699 \times 10^{-18}$		
IVC/Ao [s^{-1}]	-0.533	0.048	$< 10^{-8}$	0.0027
[Glyco] [$M^{-1}s^{-1}$]	3.854	0.401	$< 10^{-8}$	
[$\%^{-1}s^{-1}$]	0.064			
IVC/Ao×Weight [$kg^{-1}s^{-1}$]	6.128×10^{-3}	6.791×10^{-4}	$< 10^{-8}$	
[Glyco]×Volume [$M^{-1}l^{-1}s^{-1}$]	-1.828	0.226	$< 10^{-8}$	

7.4 DISCUSSION

This study explored the changes in phantom T_1s with the variation of glycogen concentration and changes in liver shMOLLI T_1 of healthy human volunteers with the variation of liver glycogen concentration and body hydration status with the aim of deriving a mathematical relationship between these measurements. Gore et al. have previously shown that glycogen acted as a relaxation agent as it decreased both T_1 and T_2 of phantoms [159]. Similar phantom measurements to those performed by Gore et al. have been repeated in this study at 1.5 T and 3 T at human body temperature. Results of these experiments also showed a strong

dependence of longitudinal and transverse relaxation times on glycogen concentration.

Being encouraged by phantom results, an initial human study with one volunteer was conducted and revealed that an increased liver glycogen concentration is accompanied by a decreased shMOLLI T_1. A limitation of this pilot study was that glycogen concentration was not quantified, only the self-reported metabolic state of the volunteer was available. The second arm of the pilot study revealed that liver shMOLLI T_1 increased immediately after the ingestion of 1.5 l of isotonic water, peaking at 30 minutes after water intake, an effect explained by an increased blood volume reaching the liver from the gut via the portal vein. This increase in T_1 was then followed by a slow decrease, while the IVC/Ao ratio reached and maintained a steady-state by the end of the hydration experiments. This finding suggests that the IVC/Ao ratio may be a useful indicator of body hydration in prospective studies. The higher-than-baseline liver shMOLLI T_1 even after an hour from water ingestion can be explained by an increase of volume in the systemic circulation, a similar trend in the evolution of shMOLLI T_1 values being also observed in the erector spinae muscles.

The multi-participant study showed a clear dependence of shMOLLI R_1 values on liver glycogen concentration and different indicators of hydration status. A significant mean decrease of 115.9 mM of glycogen concentration from the fed state to the post-exercise state resulted in a mean increase of 27 ms in shMOLLI T_1 values according to model #2. Although a significant increase was observed in IVC/Ao ratio from the hypo- to the hypervolaemic states (average increase of 0.3), this did not correspond to a non-significant increase of 9 ms in shMOLLI T_1 measurements.

Data was fitted to two LMMs, both of which proved to be capable of explaining a large amount of the variance in the measured shMOLLI R_1. The interpretation of these models was carried out based on two assumptions: increasing glycogen concentration leads to higher shMOLLI R_1 measurements, as seen in phantoms, while increased hydration leads

to a lower shMOLLI R_1, as seen in pilot experiments.

The difference between the two models lies in the way they represent hydration status. Although model #1 explained a large portion of the variance of the original shMOLLI R_1 measurements, it did not produce significant estimates of the predictor variable effects. Model #2 did and it also provided a glycogen relaxivity value similar to that found in phantoms.

The study has several limitations. Data modelling was based on a relatively small sample size with only five observations per subject. Liver glycogen concentrations might be confounded by glycogen signal originating from skeletal muscle of the chest wall in some participants. A further bias to liver glycogen concentration measurements can be ascribed to changes in liver volumes, leading to changes in the amount of liver to which the ^{13}C coil was sensitive to. Liver volume and body weight, as indicators of hydration status, were confounded by the presence of glycogen due to 3-4 g of water being bound to each gram of glycogen [173]. A further limitation of the study was the imprecise measure of hydration status, leading to uncertainty when choosing a relevant non-invasive measure. It is also known that the liver responds in different ways to exercise: micro-inflammation can follow acute exercise, however, it has also been shown that regular exercise has anti-inflammatory effects [174] - two processes that have competing effects on liver shMOLLI T_1 measurements, suggesting that perhaps the choice of glycogen depletion by exercise was not ideal due to possible differences in participants' training habits. Instead, a longer, 24 hour fasting period could be used in future studies with controlled fluid intake to minimise cross-effects due to changes in body hydration.

7.5 CONCLUSION

As opposed to other sources of bias of shMOLLI T_1 measurements, discussed in chapters 4 and 5, glycogen acts as an intrinsic relaxation agent; therefore, it affects tissue T_1 irrespective of the measurement technique. Previously reported liver shMOLLI T_1s of healthy volunteers might be biased by variable levels of liver glycogen concentration and hydration status, making it difficult to define a "normal" range of liver shMOLLI T_1s. Healthy volunteers just starting or just finishing a crash diet will also show a biased shMOLLI T_1 compared to their "normal" metabolic state, as will patients suffering from liver disease involving impairment of glycogen storage, such as various types of glycogen storage disease [175] and type 1 diabetes [176, 177]. In all these cases it is necessary to correct shMOLLI T_1 measurements for the effects of glycogen. Based on the findings of the current study, liver MRI study participants should be advised to fast for 6 to 8 hours and to refrain from ingesting liquids 1 hour prior to their scan to increase reliability of and minimise the effect of increased blood volume on T_1 measurements.

8

Summary and outlook

8.1 CONCLUSIONS

The aim of this thesis was to explore and characterise effects that can influence T_1 measurements of the liver, the major motivation for this being the aim to transform T_1 measurements from a simple intrinsic property of the hepatic tissue into a quantitative MRI-based biomarker that can be used in the diagnosis of inflammation or fibrosis. Chapter 4 presented the deleterious effect of fat and frequency offsets on T_1 values measured by (sh)MOLLI sequences explained by the sensitivity of the bSSFP readout to frequency changes. The results of this exploratory work have been summarised in a paper published in the Journal of Magnetic Resonance Imaging [17].

One way of eliminating the problems caused by fat and field inhomogeneities without a change in the sequence was to develop an offline post-processing method which was built as the extension of an existing biophysical model of the liver [14], as presented in chapter 5. This model considered fat as a separate compartment in addition to intracellular and

extracellular fluid compartments and allowed a simulation of various liver shMOLLI T_1s by varying the extracellular volume fraction, as a proxy of fibrosis, until the simulated shMOLLI bSSFP signal matched the measured signal. Then the effect of fat could be removed by only simulating the intra- and extracellular components with increased volumes due to the proportional redistribution of the fat volume fraction. Off-resonance effects were also eliminated during the post-processing step by including them in the initial Bloch simulation and removing them during the final water signal simulation. The water shMOLLI T_1 determination algorithm is now subject to a UK/EU patent application (WO2018083504A1) [178] and a scientific paper summarising the results of the validation study is expected to be published in NMR in Biomedicine.

Although the algorithm was validated using spectroscopic T_1 measurements of the liver as a gold standard that was unaffected by fat and off-resonance effects, the water shMOLLI T_1 determination process was tested on an already existing data set of patients enrolled into a clinical study to evaluate the correlation of water-only shMOLLI T_1 values with Ishak fibrosis stages. While many confounding factors have been identified for liver T_1 values in general, and liver shMOLLI T_1 values in particular, the relatively large standard deviation of liver shMOLLI T_1 values of healthy volunteers had not been addressed. The physiological study presented in chapter 7 aimed to pursue this and describe the effect of liver glycogen concentration and body hydration status on liver shMOLLI T_1 measurements. The outcomes of this study confirmed that there is a strong relationship between liver shMOLLI T_1 and liver glycogen concentration and it suggested that increased body hydration status might also drive an increase in liver shMOLLI T_1s. These results are of three-fold significance: they not only help to explain the variance of healthy liver shMOLLI T_1 measurements, but are also useful in deriving a set of concise instructions for liver MRI scan participants for the future, and they help in understanding shMOLLI T_1 measurements of participants with

glycogen storage-related comorbidities.

So far, the scientific literature described a number of confounding factors and their impact on liver T_1 values:

- Inflammation and fibrosis can both increase liver T_1 [12, 13, 115], but exert their action on the liver tissue over different time frames. Inflammation is a short term effect progressing over weeks as several animal studies have shown [179, 180], but evidence in humans is still unavailable, while the development of fibrosis can take months to years to develop and up to 20 years to progress into cirrhosis [181].

- Iron concentration shortens liver T_1 [15, 16], an effect further enhanced in shMOLLI T_1s by the sequence's dependence on iron-dependent T_2 values [109]. The build-up of iron can be due to hereditary or genetic disease or ageing [182].

- Fat concentration also influences the measurement of liver T_1 values, albeit indirectly, by partial volume effects. The direction of change is, however, dependent on the T_1 mapping sequence used: measured T_1 values are shorter than normal liver T_1 in the presence of fat when using e.g. spin echo-based sequences but will have a complex dependence on off-resonance frequency and sequence parameters when using (sh)MOLLI and can either shorten or elevate measured T_1 values. Variations in hepatic lipid concentration can be measured on the time scale of weeks [183–185], due to the active role of lipids in metabolism and energy production, although rapid changes taking place within a day have been also reported recently [186].

- Glycogen concentration was shown to act as an intrinsic T_1 relaxation agent in phantoms [159] and the study presented in chapter 7 demonstrated that liver T_1 also decreases with increasing concentrations of glycogen. Fast diurnal changes of liver

glycogen concentration [187] translate thus into dynamic variation of liver T_1 values too.

- Body hydration status was suggested to also change liver T_1 in chapter 7 as a result of diurnal variation with fluid and food consumption.

The effects and time frames of confounding factors are summarised in fig. 8.1.

8.2 OUTLOOK

Since the liver is an organ performing multiple dynamic regulatory, metabolic and endocrine functions, there might exist numerous other factors that influence its T_1. A logical next step would be to identify these influencing factors and characterise the magnitude of their impact and the time frame over which they act.

In addition to the confounding factors enumerated in the previous section, a number of other factors have been recognised to influence liver physiology, and, perhaps, liver T_1:

- Age was found to further shorten liver T_1 values in a group of participants with ages ranging between 21 and 60 years [111] at 0.08 T. A recent large population study did not find such a relationship between age and liver T_1, however the range of ages was 40-79 years [188]. Although the Richards study [111] did not find a significant difference between T_1s of male and female participants (who were not oral contraceptive users) younger than 40 years, Pavlides did report a significant dependence of liver T_1 on age in a small cohort of pre-menopausal women [110], suggesting that the female hormonal cycle regulating menstruation may affect liver T_1 measurements by changing the overall body hydration status.

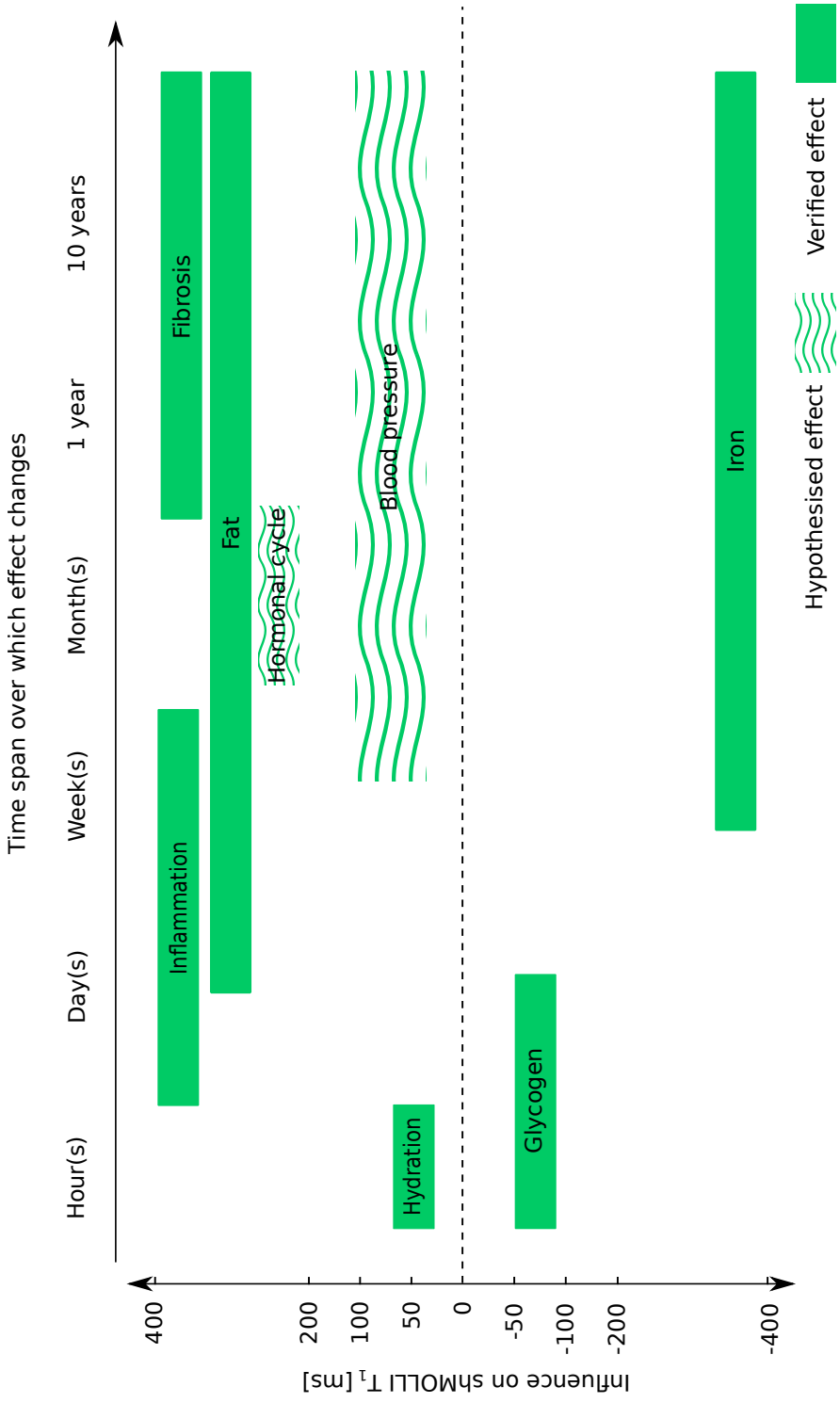

Figure 8.1: Physiological and dietary effects affecting T_1 values and the size of their influence at 3 T

- Oral contraceptive pills have been shown to increase T_1 measurements of the liver in female participants of 40 years of age or younger [111] compared to a matched group who did not use such pharmaceuticals.

- Liver tissue regeneration as a result of either surgical intervention or chemical injury is a relatively fast process, human livers being able to regenerate to the full liver mass in weeks only [189, 190] and, in general, regeneration is proportional on the amount of residual hepatic tissue. Since hepatocytes are replicated during this process, it is likely that the T_1 value of the liver will also undergo changes.

- Arterial hypertension in cirrhotic patients is associated with abnormal renin-angiotensin regulation and also with a decrease of thoracic arterial blood volume [191], while portal hypertension is associated with fluid congestion in the liver, and has been shown to cause liver T_1 elevation [108].

- Elevated levels of manganese concentration in the liver can occur in certain diseases (e.g. cirrhosis) [192]. Since manganese is a known T_1 relaxation agent [193], it is reasonable to hypothesise that increased manganese concentration will lead to shorter liver T_1 values.

Finally, there are some factors that may or may not have a direct effect on liver T_1 values: diurnal variation of bile in the liver, caffeine consumption, alcohol consumption, and pharmaceuticals (other than oral contraceptives). While small studies can be set up to individually explore the potential effects discussed above, their validation should be performed in large population studies, such as the UK Biobank imaging study.

Characterising the effect of the parameters listed in this section on liver T_1 is a crucial step towards transforming T_1 values from an intrinsic tissue parameter to a quantitative

MRI biomarker. Until then, T_1 can be used along with other quantitative MRI biomarkers (e.g. PDFF, HIC) in clinical studies and drug trials, but comparison with histological scores will have to be carried out.

On the technical development side, future work should focus on developing T_1 mapping methods that are reflecting the true T_1 of the water component of the liver parenchyma, without a bias from extrinsic influencing factors, e.g. hepatic lipid concentration or frequency offsets. Efforts in this direction have already been made by other research groups [12, 194], however, the wider acceptance of liver T_1 mapping both in clinical practice and in research settings would benefit from the development of a standardised acquisition.

Bibliography

[1] J. Ludwig, T. R. Viggiano, D. B. McGill, and B. J. Oh, "Nonalcoholic steatohepatitis: Mayo Clinic experiences with a hitherto unnamed disease," *Mayo Clinic proceedings*, vol. 55, pp. 434–8, Jul 1980. Cited on p. 1.

[2] P. Angulo, "Nonalcoholic Fatty Liver Disease," *New England Journal of Medicine*, vol. 346, pp. 1221–1231, 2002. Cited on pp. 1 and 73.

[3] G. C. Farrell and C. Z. Larter, "Nonalcoholic fatty liver disease: From steatosis to cirrhosis," *Hepatology*, vol. 43, pp. S99–S112, Feb 2006. Cited on p. 1.

[4] G. Ramakrishna, A. Rastogi, N. Trehanpati, B. Sen, R. Khosla, and S. K. Sarin, "From cirrhosis to hepatocellular carcinoma: new molecular insights on inflammation and cellular senescence.," *Liver Cancer*, vol. 2, pp. 367–83, Aug 2013. Cited on p. 1.

[5] R. C. Lo and H. Kim, "Histopathological evaluation of liver fibrosis and cirrhosis regression," *Clinical and molecular hepatology*, vol. 23, pp. 302–307, Dec 2017. Cited on p. 1.

[6] E. L. Ellis and D. A. Mann, "Clinical evidence for the regression of liver fibrosis," *Journal of Hepatology*, vol. 56, pp. 1171–1180, May 2012. Cited on p. 1.

[7] J. A. López-Velázquez, K. V. Silva-Vidal, G. Ponciano-Rodríguez, N. C. Chávez-Tapia, M. Arrese, M. Uribe, and N. Méndez-Sánchez, "The prevalence of nonalcoholic fatty liver disease in the Americas.," *Annals of hepatology*, vol. 13, no. 2, pp. 166–78. Cited on pp. 2 and 73.

[8] Z. M. Younossi, A. B. Koenig, D. Abdelatif, Y. Fazel, L. Henry, and M. Wymer, "Global epidemiology of nonalcoholic fatty liver disease—Meta-analytic assessment of prevalence, incidence, and outcomes," *Journal of Hepatology*, vol. 64, no. 1, pp. 73–84, 2016. Cited on pp. 2, 40, and 73.

[9] R. Williams, R. Aspinall, M. Bellis, G. Camps-Walsh, M. Cramp, A. Dhawan, J. Ferguson, D. Forton, G. Foster, I. Gilmore, M. Hickman, M. Hudson, D. Kelly, A. Langford,

M. Lombard, L. Longworth, N. Martin, K. Moriarty, P. Newsome, J. O'Grady, R. Pryke, H. Rutter, S. Ryder, N. Sheron, and T. Smith, "Addressing liver disease in the UK: a blueprint for attaining excellence in health care and reducing premature mortality from lifestyle issues of excess consumption of alcohol, obesity, and viral hepatitis," *The Lancet*, vol. 384, pp. 1953–1997, 2014. Cited on p. 2.

[10] D. R. Messroghli, J. C. Moon, V. M. Ferreira, L. Grosse-Wortmann, T. He, P. Kellman, J. Mascherbauer, R. Nezafat, M. Salerno, E. B. Schelbert, A. J. Taylor, R. Thompson, M. Ugander, R. B. van Heeswijk, and M. G. Friedrich, "Clinical recommendations for cardiovascular magnetic resonance mapping of T1, T2, T2* and extracellular volume: A consensus statement by the Society for Cardiovascular Magnetic Resonance (SCMR) endorsed by the European Association for Cardiovascular Imagi," *Journal of Cardiovascular Magnetic Resonance*, vol. 19, p. 75, Dec 2017. Cited on pp. 2 and 49.

[11] J. C. Moon, D. R. Messroghli, P. Kellman, S. K. Piechnik, M. D. Robson, M. Ugander, P. D. Gatehouse, A. E. Arai, M. G. Friedrich, S. Neubauer, J. Schulz-Menger, and E. B. Schelbert, "Myocardial T1 mapping and extracellular volume quantification: a Society for Cardiovascular Magnetic Resonance (SCMR) and CMR Working Group of the European Society of Cardiology consensus statement," *Journal of Cardiovascular Magnetic Resonance*, vol. 15, p. 92, Oct 2013. Cited on pp. 2, 49, and 52.

[12] C. L. Hoad, N. Palaniyappan, P. Kaye, Y. Chernova, M. W. James, C. Costigan, A. Austin, L. Marciani, P. A. Gowland, I. N. Guha, S. T. Francis, and G. P. Aithal, "A study of T1 relaxation time as a measure of liver fibrosis and the influence of confounding histological factors," *NMR in Biomedicine*, vol. 28, pp. 706–714, Jun 2015. Cited on pp. 2, 3, 49, 98, 133, and 137.

[13] R. Banerjee, M. Pavlides, E. M. Tunnicliffe, S. K. Piechnik, N. Sarania, R. Philips, J. D. Collier, J. C. Booth, J. E. Schneider, L. M. Wang, D. W. Delaney, K. A. Fleming, M. D. Robson, E. Barnes, and S. Neubauer, "Multiparametric magnetic resonance for the non-invasive diagnosis of liver disease," *Journal of Hepatology*, vol. 60, pp. 69–77, Jan 2014. Cited on pp. 2, 3, 49, 52, 53, 56, 59, 62, 63, 68, 69, 82, 101, 102, 111, and 133.

[14] E. M. Tunnicliffe, R. Banerjee, M. Pavlides, S. Neubauer, and M. D. Robson, "A model for hepatic fibrosis: the competing effects of cell loss and iron on shortened modified Look-Locker inversion recovery T1 (shMOLLI-T1) in the liver," *Journal of Magnetic Resonance Imaging*, vol. 45, pp. 450–462, Feb 2017. Cited on pp. 2, 50, 72, 81, 82, 91, 96, 98, 103, 114, 126, and 131.

[15] N. R. Ghugre, T. D. Coates, M. D. Nelson, and J. C. Wood, "Mechanisms of tissue-iron relaxivity: nuclear magnetic resonance studies of human liver biopsy specimens," *Magnetic Resonance in Medicine*, vol. 54, pp. 1185–1193, Nov 2005. Cited on pp. 3, 50, 72, and 133.

[16] J. C. Wood, M. Otto-Duessel, M. Aguilar, H. Nick, M. D. Nelson, T. D. Coates, H. Pollack, and R. Moats, "Cardiac iron determines cardiac T2*, T2, and T1 in the gerbil model of iron cardiomyopathy.," *Circulation*, vol. 112, pp. 535–43, Jul 2005. Cited on pp. 3, 48, 50, 80, and 133.

[17] F. E. Mozes, E. M. Tunnicliffe, M. Pavlides, and M. D. Robson, "Influence of fat on liver T1 measurements using modified Look-Locker inversion recovery (MOLLI) methods at 3T," *Journal of Magnetic Resonance Imaging*, vol. 44, pp. 105–111, Jul 2016. Cited on pp. 4, 72, and 131.

[18] F. Bloch, "Nuclear Induction," *Physical Review*, vol. 70, pp. 460–474, Oct 1946. Cited on pp. 5 and 9.

[19] E. M. Purcell, H. C. Torrey, and R. V. Pound, "Resonance Absorption by Nuclear Magnetic Moments in a Solid," *Physical Review*, vol. 69, pp. 37–38, Jan 1946. Cited on p. 5.

[20] P. J. Hore, *Nuclear Magnetic Resonance*. Oxford University Press, 2001. Cited on p. 5.

[21] D. Hoult, "The origins and present status of the radio wave controversy in NMR," *Concepts in Magnetic Resonance Part A*, vol. 34A, pp. 193–216, Jul 2009. Cited on p. 10.

[22] J. P. Felmlee, R. L. Morin, J. R. Salutz, and G. B. Lund, "Magnetic resonance imaging phase encoding: a pictorial essay.," *RadioGraphics*, vol. 9, pp. 717–722, Jul 1989. Cited on p. 20.

[23] E. L. Hahn, "Spin Echoes," *Physical Review*, vol. 80, pp. 580–594, Nov 1950. Cited on p. 22.

[24] D. Burstein, "Stimulated echoes: Description, applications, practical hints," *Concepts in Magnetic Resonance*, vol. 8, pp. 269–278, Jan 1996. Cited on p. 24.

[25] M. Deimling and O. Heid, "Magnetization prepared true FISP imaging," in *Proceedings 2nd Scientific Meeting, International Society for Magnetic Resonance in Medicine*, p. 495, 1994. Cited on p. 27.

[26] D. G. Nishimura and S. S. Vasanawala, "Analysis and Reduction of the Transient Response in SSFP Imaging," in *Proceedings of the International Society for Magnetic Resonance in Medicine*, p. 301, 2000. Cited on pp. 27, 58, 75, and 115.

[27] V. S. Deshpande, S. M. Shea, G. Laub, O. P. Simonetti, J. P. Finn, and D. Li, "3D magnetization-prepared true-FISP: a new technique for imaging coronary arteries.," *Magnetic Resonance in Medicine*, vol. 46, pp. 494–502, Sep 2001. Cited on pp. 27, 58, 75, and 115.

[28] J. Frahm, K.-D. Merboldt, and W. Hänicke, "Localized proton spectroscopy using stimulated echoes," *Journal of Magnetic Resonance (1969)*, vol. 72, no. 3, pp. 502–508, 1987. Cited on p. 28.

[29] S. B. Reeder, I. Cruite, G. Hamilton, and C. B. Sirlin, "Quantitative Assessment of Liver Fat with Magnetic Resonance Imaging and Spectroscopy," *Journal of Magnetic Resonance Imaging*, vol. 34, pp. 729–749, Oct 2011. Cited on pp. 28, 44, 46, and 114.

[30] D. R. Messroghli, A. Radjenovic, S. Kozerke, D. M. Higgins, M. U. Sivananthan, and J. P. Ridgway, "Modified Look-Locker inversion recovery (MOLLI) for high-resolution T1 mapping of the heart.," *Magnetic Resonance in Medicine*, vol. 52, pp. 141–146, Jul 2004. Cited on pp. 31, 51, 52, 58, and 78.

[31] S. K. Piechnik, V. M. Ferreira, E. Dall'Armellina, L. E. Cochlin, A. Greiser, S. Neubauer, and M. D. Robson, "Shortened Modified Look-Locker Inversion recovery (ShMOLLI) for clinical myocardial T1-mapping at 1.5 and 3 T within a 9 heartbeat breathhold.," *Journal of Cardiovascular Magnetic Resonance*, vol. 12, p. 69, Jan 2010. Cited on pp. 31, 32, 51, 65, 72, 75, 86, and 88.

[32] R. Deichmann and A. Haase, "Quantification of T1 values by SNAPSHOT-FLASH NMR imaging," *Journal of Magnetic Resonance (1969)*, vol. 96, pp. 608–612, Feb 1992. Cited on pp. 32, 58, and 78.

[33] H. Yu, C. A. McKenzie, A. Shimakawa, A. T. Vu, A. C. Brau, P. J. Beatty, A. R. Pineda, J. H. Brittain, and S. B. Reeder, "Multiecho reconstruction for simultaneous water-fat decomposition and $T2^*$ estimation," *Journal of Magnetic Resonance Imaging*, vol. 26, pp. 1153–1161, Oct 2007. Cited on pp. 33 and 54.

[34] S. B. Reeder, A. R. Pineda, Z. Wen, A. Shimakawa, H. Yu, J. H. Brittain, G. E. Gold, C. H. Beaulieu, and N. J. Pelc, "Iterative decomposition of water and fat with echo asymmetry and least-squares estimation (IDEAL): Application with fast spin-echo imaging," *Magnetic Resonance in Medicine*, vol. 54, pp. 636–644, Sep 2005. Cited on p. 33.

[35] A. R. Pineda, S. B. Reeder, Z. Wen, and N. J. Pelc, "Cramér-Rao bounds for three-point decomposition of water and fat," *Magnetic Resonance in Medicine*, vol. 54, pp. 625–635, Sep 2005. Cited on p. 33.

[36] W. T. Dixon, "Simple proton spectroscopic imaging.," *Radiology*, vol. 153, pp. 189–94, Oct 1984. Cited on p. 33.

[37] C. Couinaud, *The Liver. Anatomical and surgical investigations (Le foie. Etudes anatomiques et chirugicales)*. Paris: Masson, 1957. Cited on p. 35.

[38] S. R. Z. Abdel-Misih and M. Bloomston, "Liver anatomy.," *The Surgical clinics of North America*, vol. 90, pp. 643–53, Aug 2010. Cited on pp. 35 and 36.

[39] L. C. Junqueira, J. Carneiro, and R. O. Kelley, *Basic Histology*. McGraw-Hill, 9th ed., 1998. Cited on p. 37.

[40] E. R. Anderson and Y. M. Shah, "Iron homeostasis in the liver.," *Comprehensive Physiology*, vol. 3, pp. 315–30, Jan 2013. Cited on p. 39.

[41] L. Calzadilla Bertot and L. A. Adams, "The Natural Course of Non-Alcoholic Fatty Liver Disease," *International Journal of Molecular Sciences*, vol. 17, May 2016. Cited on pp. 40 and 73.

[42] S. Gowda, P. B. Desai, V. V. Hull, A. A. K. Math, S. N. Vernekar, and S. S. Kulkarni, "A review on laboratory liver function tests.," *The Pan African medical journal*, vol. 3, p. 17, Nov 2009. Cited on p. 41.

[43] R. A. Standish, E. Cholongitas, A. Dhillon, A. K. Burroughs, and A. P. Dhillon, "An appraisal of the histopathological assessment of liver fibrosis.," *Gut*, vol. 55, pp. 569–78, Apr 2006. Cited on p. 41.

[44] A. R. Hall, A. C. Green, T.-V. Luong, A. K. Burroughs, J. Wyatt, and A. P. Dhillon, "The use of guideline images to improve histological estimation of hepatic steatosis," *Liver International*, vol. 34, pp. 1414–1427, Oct 2014. Cited on p. 41.

[45] G. P. Coral, A. D. P. Antunes, A. P. A. Serafini, F. B. Araujo, and A. A. de Mattos, "Liver Biopsy: Importance of Specimen Size in the Diagnosis and Staging of Chronic Viral Hepatitis," *Revista do Instituto de Medicina Tropical de São Paulo*, vol. 58, no. 1, pp. 55–59, 2016. Cited on p. 41.

[46] V. Ratziu, F. Charlotte, A. Heurtier, S. Gombert, P. Giral, E. Bruckert, A. Grimaldi, F. Capron, and T. Poynard, "Sampling Variability of Liver Biopsy in Nonalcoholic Fatty Liver Disease," *Gastroenterology*, vol. 128, pp. 1898–1906, Jun 2005. Cited on p. 41.

[47] D. E. Kleiner, E. M. Brunt, M. Van Natta, C. Behling, M. J. Contos, O. W. Cummings, L. D. Ferrell, Y.-C. Liu, M. S. Torbenson, A. Unalp-Arida, M. Yeh, A. J. McCullough, and A. J. Sanyal, "Design and validation of a histological scoring system for non-alcoholic fatty liver disease," *Hepatology*, vol. 41, pp. 1313–1321, Jun 2005. Cited on p. 41.

[48] K. Ishak, A. Baptista, L. Bianchi, F. Callea, J. De Groote, F. Gudat, H. Denk, V. Desmet, G. Korb, R. N. MacSween, M. Phillips, B. G. Portmann, H. Poulsen, P. J. Scheuer, M. Schmid, and H. Thaler, "Histological grading and staging of chronic hepatitis," *Journal of Hepatology*, vol. 22, pp. 696–699, Jun 1995. Cited on pp. 41 and 68.

[49] P. Thampanitchawong and T. Piratvisuth, "Liver biopsy: complications and risk factors.," *World Journal of Gastroenterology*, vol. 5, pp. 301–304, Aug 1999. Cited on p. 41.

[50] N. Khov, A. Sharma, and T. R. Riley, "Bedside ultrasound in the diagnosis of non-alcoholic fatty liver disease.," *World Journal of Gastroenterology*, vol. 20, pp. 6821–5, Jun 2014. Cited on p. 42.

[51] S. Dasarathy, J. Dasarathy, A. Khiyami, R. Joseph, R. Lopez, and A. J. McCullough, "Validity of real time ultrasound in the diagnosis of hepatic steatosis: A prospective study," *Journal of Hepatology*, vol. 51, pp. 1061–1067, Dec 2009. Cited on p. 42.

[52] T. R. Riley, A. Mendoza, and M. A. Bruno, "Bedside Ultrasound Can Predict Non-alcoholic Fatty Liver Disease in the Hands of Clinicians Using a Prototype Image," *Digestive Diseases and Sciences*, vol. 51, pp. 982–985, May 2006. Cited on p. 42.

[53] C.-C. Choong, S. K. Venkatesh, and E. P. Y. Siew, "Accuracy of routine clinical ultrasound for staging of liver fibrosis.," *Journal of Clinical Imaging Science*, vol. 2, p. 58, 2012. Cited on p. 42.

[54] M. D'Onofrio, E. Martone, S. Brunelli, N. Faccioli, G. Zamboni, I. Zagni, G. Fattovich, and R. Pozzi Mucelli, "Accuracy of ultrasound in the detection of liver fibrosis in chronic viral hepatitis.," *La Radiologia medica*, vol. 110, pp. 341–8, Oct 2005. Cited on p. 42.

[55] T. Nishiura, H. Watanabe, M. Ito, Y. Matsuoka, K. Yano, M. Daikoku, H. Yatsuhashi, K. Dohmen, and H. Ishibashi, "Ultrasound evaluation of the fibrosis stage in chronic liver disease by the simultaneous use of low and high frequency probes," *The British Journal of Radiology*, vol. 78, pp. 189–197, Mar 2005. Cited on p. 42.

[56] S. Mueller and L. Sandrin, "Liver stiffness: a novel parameter for the diagnosis of liver disease," *Hepatic Medicine: Evidence and Research*, vol. 2, pp. 49–67, May 2010. Cited on p. 42.

[57] J. F. Gerstenmaier and R. N. Gibson, "Ultrasound in chronic liver disease," *Insights into Imaging*, vol. 5, pp. 441–455, Aug 2014. Cited on p. 42.

[58] P. Marcellin, M. Ziol, P. Bedossa, C. Douvin, R. Poupon, V. de Lédinghen, and M. Beaugrand, "Non-invasive assessment of liver fibrosis by stiffness measurement in patients with chronic hepatitis B," *Liver International*, vol. 29, pp. 242–247, Feb 2009. Cited on p. 43.

[59] M. Ziol, A. Handra-Luca, A. Kettaneh, C. Christidis, F. Mal, F. Kazemi, V. de Lédinghen, P. Marcellin, D. Dhumeaux, J.-C. Trinchet, and M. Beaugrand, "Noninvasive

assessment of liver fibrosis by measurement of stiffness in patients with chronic hepatitis C," *Hepatology*, vol. 41, pp. 48–54, Jan 2005. Cited on p. 43.

[60] A. Wong, D. a. Clausi, and P. Fieguth, "CPOL: complex phase order likelihood as a similarity measure for MR-CT registration.," *Medical Image Analysis*, vol. 14, pp. 50–7, Feb 2010. Cited on p. 43.

[61] M. Pavlides, R. Banerjee, E. M. Tunnicliffe, C. Kelly, J. Collier, L. M. Wang, K. A. Fleming, J. F. Cobbold, M. D. Robson, S. Neubauer, and E. Barnes, "Multi-parametric magnetic resonance imaging for the assessment of non-alcoholic fatty liver disease severity," *Liver International*, Oct 2016. Cited on p. 43.

[62] L. Castéra, J. Foucher, P.-H. Bernard, F. Carvalho, D. Allaix, W. Merrouche, P. Couzigou, and V. de Lédinghen, "Pitfalls of liver stiffness measurement: A 5-year prospective study of 13,369 examinations," *Hepatology*, vol. 51, pp. NA–NA, Mar 2010. Cited on p. 43.

[63] J. F. L. Cobbold and S. D. Taylor-Robinson, "Transient elastography in acute hepatitis: All that's stiff is not fibrosis," *Hepatology*, vol. 47, pp. 370–372, Jan 2008. Cited on p. 43.

[64] B. Coco, F. Oliveri, A. M. Maina, P. Ciccorossi, R. Sacco, P. Colombatto, F. Bonino, and M. R. Brunetto, "Transient elastography: a new surrogate marker of liver fibrosis influenced by major changes of transaminases," *Journal of Viral Hepatitis*, vol. 14, pp. 360–369, May 2007. Cited on p. 43.

[65] T. Reiberger, A. Ferlitsch, B. A. Payer, M. Pinter, M. Homoncik, M. Peck-Radosavljevic, and V. H. H. Lab, "Non-selective β-blockers improve the correlation of liver stiffness and portal pressure in advanced cirrhosis," *Journal of Gastroenterology*, vol. 47, pp. 561–568, May 2012. Cited on p. 43.

[66] I. Mederacke, K. Wursthorn, J. Kirschner, K. Rifai, M. P. Manns, H. Wedemeyer, and M. J. Bahr, "Food intake increases liver stiffness in patients with chronic or resolved hepatitis C virus infection," *Liver International*, vol. 29, pp. 1500–1506, Nov 2009. Cited on p. 43.

[67] P. J. Pickhardt, S. H. Park, L. Hahn, S.-G. Lee, K. T. Bae, and E. S. Yu, "Specificity of unenhanced CT for non-invasive diagnosis of hepatic steatosis: implications for the investigation of the natural history of incidental steatosis," *European Radiology*, vol. 22, pp. 1075–1082, May 2012. Cited on pp. 43 and 44.

[68] S. H. Park, P. N. Kim, K. W. Kim, S. W. Lee, S. E. Yoon, S. W. Park, H. K. Ha, M.-G. Lee, S. Hwang, S.-G. Lee, E. S. Yu, and E. Y. Cho, "Macrovesicular Hepatic Steatosis

in Living Liver Donors: Use of CT for Quantitative and Qualitative Assessment," *Radiology*, vol. 239, pp. 105–112, Apr 2006. Cited on p. 44.

[69] S. S. Lee and S. H. Park, "Radiologic evaluation of nonalcoholic fatty liver disease," *World Journal of Gastroenterology*, vol. 20, pp. 7392–402, Jun 2014. Cited on p. 44.

[70] D. Patrick, F. E. White, and P. C. Adams, "Long-term amiodarone therapy: a cause of increased hepatic attenuation on CT," *The British Journal of Radiology*, vol. 57, pp. 573–576, Jul 1984. Cited on p. 44.

[71] A. Huber, L. Ebner, J. T. Heverhagen, and A. Christe, "State-of-the-art imaging of liver fibrosis and cirrhosis: A comprehensive review of current applications and future perspectives.," *European Journal of Radiology Open*, vol. 2, pp. 90–100, 2015. Cited on p. 44.

[72] M. Kudo, R. Q. Zheng, S. R. Kim, Y. Okabe, Y. Osaki, H. Iijima, T. Itani, H. Kasugai, M. Kanematsu, K. Ito, N. Usuki, K. Shimamatsu, M. Kage, and M. Kojiro, "Diagnostic Accuracy of Imaging for Liver Cirrhosis Compared to Histologically Proven Liver Cirrhosis," *Intervirology*, vol. 51, no. 1, pp. 17–26, 2008. Cited on p. 44.

[73] A. Huber, L. Ebner, M. Montani, N. Semmo, C. Roy, J. Heverhagen, and A. Christe, "Computed tomography findings in liver fibrosis and cirrhosis," *Swiss Medical Weekly*, Feb 2014. Cited on p. 44.

[74] U. F. Administration and Drug, "What are the Radiation Risks from CT?," 2009. Cited on p. 44.

[75] R. Loomba, "Role of imaging-based biomarkers in NAFLD: Recent advances in clinical application and future research directions," *Journal of Hepatology*, vol. 68, pp. 296–304, Feb 2018. Cited on p. 44.

[76] R. Muthupillai, D. J. Lomas, P. J. Rossman, J. F. Greenleaf, A. Manduca, and R. L. Ehman, "Magnetic resonance elastography by direct visualization of propagating acoustic strain waves.," *Science (New York, N.Y.)*, vol. 269, pp. 1854–7, Sep 1995. Cited on p. 44.

[77] S. Singh, S. K. Venkatesh, Z. Wang, F. H. Miller, U. Motosugi, R. N. Low, T. Hassanein, P. Asbach, E. M. Godfrey, M. Yin, J. Chen, A. P. Keaveny, M. Bridges, A. Bohte, M. H. Murad, D. J. Lomas, J. A. Talwalkar, and R. L. Ehman, "Diagnostic performance of magnetic resonance elastography in staging liver fibrosis: a systematic review and meta-analysis of individual participant data.," *Clinical Gastroenterology and Hepatology*, vol. 13, pp. 440–451.e6, Mar 2015. Cited on p. 45.

[78] L. S. Szczepaniak, P. Nurenberg, D. Leonard, J. D. Browning, J. S. Reingold, S. Grundy, H. H. Hobbs, and R. L. Dobbins, "Magnetic resonance spectroscopy to measure hepatic triglyceride content: prevalence of hepatic steatosis in the general population," *American Journal of Physiology-Endocrinology and Metabolism*, vol. 288, pp. E462–E468, Feb 2005. Cited on p. 45.

[79] H. R. Wilman, M. Kelly, S. Garratt, P. M. Matthews, M. Milanesi, A. Herlihy, M. Gyngell, S. Neubauer, J. D. Bell, R. Banerjee, and E. L. Thomas, "Characterisation of liver fat in the UK Biobank cohort," *PLOS ONE*, vol. 12, p. e0172921, Feb 2017. Cited on pp. 45 and 114.

[80] L. S. Szczepaniak, E. E. Babcock, F. Schick, R. L. Dobbins, A. Garg, D. K. Burns, J. D. McGarry, and D. T. Stein, "Measurement of intracellular triglyceride stores by H spectroscopy: validation in vivo," *The American Journal of Physiology*, vol. 276, pp. E977–89, May 1999. Cited on pp. 45 and 46.

[81] G. Hamilton, T. Yokoo, M. Bydder, I. Cruite, M. E. Schroeder, C. B. Sirlin, and M. S. Middleton, "In vivo characterization of the liver fat 1H MR spectrum," *NMR in Biomedicine*, vol. 24, pp. 784–90, Aug 2011. Cited on pp. 46, 58, 80, 82, and 89.

[82] R. Longo, C. Ricci, F. Masutti, R. Vidimari, L. S. Crocé, L. Bercich, C. Tiribelli, and L. Dalla Palma, "Fatty infiltration of the liver. Quantification by 1H localized magnetic resonance spectroscopy and comparison with computed tomography," *Investigative radiology*, vol. 28, pp. 297–302, Apr 1993. Cited on p. 46.

[83] R. Longo, P. Pollesello, C. Ricci, F. Masutti, B. J. Kvam, L. Bercich, L. S. Croce, P. Grigolato, S. Paoletti, B. De Bernard, C. Tiribelli, and L. Dalla Palma, "Proton MR spectroscopy in quantitative in vivo determination of fat content in human liver steatosis," *Journal of Magnetic Resonance Imaging*, vol. 5, pp. 281–285, May 1995. Cited on p. 46.

[84] I. S. Idilman, H. Aniktar, R. Idilman, G. Kabacam, B. Savas, A. Elhan, A. Celik, K. Bahar, and M. Karcaaltincaba, "Hepatic steatosis: quantification by proton density fat fraction with MR imaging versus liver biopsy.," *Radiology*, vol. 267, pp. 767–75, Jun 2013. Cited on pp. 46, 53, and 99.

[85] C. W. Hong, A. Mamidipalli, J. C. Hooker, G. Hamilton, T. Wolfson, D. H. Chen, S. Fazeli Dehkordy, M. S. Middleton, S. B. Reeder, R. Loomba, and C. B. Sirlin, "MRI proton density fat fraction is robust across the biologically plausible range of triglyceride spectra in adults with nonalcoholic steatohepatitis," *Journal of Magnetic Resonance Imaging*, Aug 2017. Cited on p. 46.

[86] W. M. Haufe, T. Wolfson, C. A. Hooker, J. C. Hooker, Y. Covarrubias, A. N. Schlein, G. Hamilton, M. S. Middleton, J. E. Angeles, D. Hernando, S. B. Reeder, J. B. Schwim-

mer, and C. B. Sirlin, "Accuracy of PDFF estimation by magnitude-based and complex-based MRI in children with MR spectroscopy as a reference," *Journal of Magnetic Resonance Imaging*, vol. 46, pp. 1641–1647, Dec 2017. Cited on p. 46.

[87] N. S. Artz, W. M. Haufe, C. A. Hooker, G. Hamilton, T. Wolfson, G. M. Campos, A. C. Gamst, J. B. Schwimmer, C. B. Sirlin, and S. B. Reeder, "Reproducibility of MR-based liver fat quantification across field strength: Same-day comparison between 1.5T and 3T in obese subjects.," *Journal of magnetic resonance imaging : JMRI*, vol. 42, pp. 811–7, Sep 2015. Cited on p. 46.

[88] M. Bydder, G. Hamilton, L. de Rochefort, A. Desai, E. R. Heba, R. Loomba, J. B. Schwimmer, N. M. Szeverenyi, and C. B. Sirlin, "Sources of systematic error in proton density fat fraction (PDFF) quantification in the liver evaluated from magnitude images with different numbers of echoes," *NMR in Biomedicine*, p. e3843, Nov 2017. Cited on pp. 47 and 97.

[89] D. E. Horng, D. Hernando, and S. B. Reeder, "Quantification of liver fat in the presence of iron overload," *Journal of Magnetic Resonance Imaging*, vol. 45, pp. 428–439, Jul 2016. Cited on pp. 47 and 96.

[90] T. G. S. Pierre, P. R. Clark, W. Chua-anusorn, A. J. Fleming, G. P. Jeffrey, J. K. Olynyk, P. Pootrakul, E. Robins, and R. Lindeman, "Noninvasive measurement and imaging of liver iron concentrations using proton magnetic resonance," *Blood*, vol. 105, no. 2, pp. 855–861, 2005. Cited on pp. 47 and 48.

[91] P. R. Clark, W. Chua-anusorn, and T. G. St Pierre, "Bi-exponential proton transverse relaxation rate (R2) image analysis using RF field intensity-weighted spin density projection: potential for R2 measurement of iron-loaded liver.," *Magnetic Resonance Imaging*, vol. 21, pp. 519–30, Jun 2003. Cited on p. 47.

[92] N. R. Ghugre, P. Storey, C. K. Rigsby, A. A. Thompson, C. L. Carqueville, T. D. Coates, and J. C. Wood, "Multi-field behaviour of relaxivity in an iron-rich environment," in *Proceedings of the International Society for Magnetic Resonance in Medicine*, p. 644, 2008. Cited on pp. 47, 48, and 80.

[93] N. R. Ghugre, E. K. Doyle, P. Storey, and J. C. Wood, "Relaxivity-iron calibration in hepatic iron overload: Predictions of a Monte Carlo model," *Magnetic Resonance in Medicine*, vol. 74, pp. 879–883, Sep 2015. Cited on p. 47.

[94] D. Hernando, Y. S. Levin, C. B. Sirlin, and S. B. Reeder, "Quantification of liver iron with MRI: State of the art and remaining challenges," *Journal of Magnetic Resonance Imaging*, vol. 40, pp. 1003–1021, Nov 2014. Cited on p. 48.

[95] J. S. Hankins, M. B. McCarville, R. B. Loeffler, M. P. Smeltzer, M. Onciu, F. A. Hoffer, C.-S. Li, W. C. Wang, R. E. Ware, and C. M. Hillenbrand, "R2* magnetic resonance imaging of the liver in patients with iron overload.," *Blood*, vol. 113, pp. 4853–5, May 2009. Cited on p. 48.

[96] Y. Feng, T. He, P. D. Gatehouse, X. Li, M. Harith Alam, D. J. Pennell, W. Chen, D. N. Firmin, A. Taher, R. Galanello, G. Matta, M. Fogel, A. Cohen, R. Tan, K. Chen, I. Ng, A. Lai, S. Fucharoen, J. Laothamata, S. Chuncharunee, S. Jongjirasiri, D. Firmin, G. Smith, D. Pennell, H. Opitz, C. Ressayre-Djaffer, P. Marks, D. Alberti, D. Alberti, and C. Rose, "Improved MRI R2* relaxometry of iron-loaded liver with noise correction," *Magnetic Resonance in Medicine*, vol. 70, pp. 1765–1774, Dec 2013. Cited on p. 48.

[97] J. C. Wood, C. Enriquez, N. Ghugre, J. M. Tyzka, S. Carson, M. D. Nelson, and T. D. Coates, "MRI R2 and R2* mapping accurately estimates hepatic iron concentration in transfusion-dependent thalassemia and sickle cell disease patients," *Blood*, vol. 106, pp. 1460–1465, Aug 2005. Cited on p. 48.

[98] M. H. Alam, T. He, D. Auger, G. C. Smith, P. Drivas, R. Wage, C. Izgi, K. Symmonds, A. Greiser, B. S. Spottiswoode, L. Anderson, D. Firmin, and D. J. Pennell, "Validation of T2* in-line analysis for tissue iron quantification at 1.5 T.," *Journal of Cardiovascular Magnetic Resonance*, vol. 18, no. 1, p. 23, 2016. Cited on p. 48.

[99] P. Storey, A. A. Thompson, C. L. Carqueville, J. C. Wood, R. A. de Freitas, and C. K. Rigsby, "R2* imaging of transfusional iron burden at 3T and comparison with 1.5T.," *Journal of Magnetic Resonance Imaging*, vol. 25, pp. 540–7, Mar 2007. Cited on pp. 48, 68, and 80.

[100] J. C. Wood, S. Pressel, Z. R. Rogers, I. Odame, J. L. Kwiatkowski, M. T. Lee, W. C. Owen, A. R. Cohen, T. St Pierre, M. M. Heeney, W. H. Schultz, B. R. Davis, R. E. Ware, and f. t. T. TWiTCH Investigators, "Liver iron concentration measurements by MRI in chronically transfused children with sickle cell anemia: baseline results from the TWiTCH trial.," *American Journal of Hematology*, vol. 90, pp. 806–10, Sep 2015. Cited on p. 48.

[101] R. A. Assis, F. U. Kay, F. M. Conti, P. V. Campregher, G. Szarf, M. S. Diniz, M. Rodrigues, R. Helman, M. B. Funari, J. Wood, and N. Hamerschlak, "The role of magnetic resonance imaging-T2* in the evaluation of iron overload early in hereditary hemochromatosis. A cross-sectional study with 159 patients," *American Journal of Hematology*, vol. 90, pp. E220–E221, Dec 2015. Cited on p. 48.

[102] T. G. St Pierre, A. El-Beshlawy, M. Elalfy, A. Al Jefri, K. Al Zir, S. Daar, D. Habr, U. Kriemler-Krahn, and A. Taher, "Multicenter validation of spin-density projection-

assisted R2-MRI for the noninvasive measurement of liver iron concentration.," *Magnetic Resonance in Medicine*, vol. 71, pp. 2215–23, Jun 2014. Cited on p. 48.

[103] M. Westwood, L. J. Anderson, D. N. Firmin, P. D. Gatehouse, C. C. Charrier, B. Wonke, and D. J. Pennell, "A single breath-hold multiecho T2* cardiovascular magnetic resonance technique for diagnosis of myocardial iron overload.," *Journal of Magnetic Resonance Imaging*, vol. 18, pp. 33–9, Jul 2003. Cited on p. 48.

[104] M. A. Tanner, T. He, M. A. Westwood, D. N. Firmin, D. J. Pennell, and Thalassemia International Federation Heart T2* Investigators, "Multi-center validation of the transferability of the magnetic resonance T2* technique for the quantification of tissue iron.," *Haematologica*, vol. 91, pp. 1388–91, Oct 2006. Cited on p. 48.

[105] A. Meloni, H. Y. Rienhoff, A. Jones, A. Pepe, M. Lombardi, J. C. Wood, and J. C. Wood, "The use of appropriate calibration curves corrects for systematic differences in liver R2* values measured using different software packages.," *British Journal of Haematology*, vol. 161, pp. 888–91, Jun 2013. Cited on p. 48.

[106] M. Pavlides, R. Banerjee, E. M. Tunnicliffe, C. Kelly, J. Collier, L. M. Wang, K. A. Fleming, J. F. Cobbold, M. D. Robson, S. Neubauer, and E. Barnes, "Multiparametric magnetic resonance imaging for the assessment of non-alcoholic fatty liver disease severity," *Liver International*, May 2017. Cited on p. 49.

[107] P. Bedossa, C. Poitou, N. Veyrie, J.-L. Bouillot, A. Basdevant, V. Paradis, J. Tordjman, and K. Clement, "Histopathological algorithm and scoring system for evaluation of liver lesions in morbidly obese patients," *Hepatology*, vol. 56, pp. 1751–1759, Nov 2012. Cited on p. 49.

[108] N. Palaniyappan, E. Cox, C. Bradley, R. Scott, A. Austin, R. O'Neill, G. Ramjas, S. Travis, H. White, R. Singh, P. Thurley, I. N. Guha, S. Francis, and G. P. Aithal, "Non-invasive assessment of portal hypertension using quantitative magnetic resonance imaging," *Journal of Hepatology*, vol. 65, pp. 1131–1139, Dec 2016. Cited on pp. 49 and 136.

[109] M. D. Robson, S. K. Piechnik, E. M. Tunnicliffe, and S. Neubauer, "T1 measurements in the human myocardium: The effects of magnetization transfer on the SASHA and MOLLI sequences," *Magnetic Resonance in Medicine*, vol. 670, pp. 664–670, Jul 2013. Cited on pp. 50, 56, 58, 72, 88, and 133.

[110] M. Pavlides, *Multi-parametric MRI techniques for the non-invasive assessment of patients with liver disease*. PhD thesis, University of Oxford, 2016. Cited on pp. 50 and 134.

[111] M. A. Richards, J. A. W. Webb, S. E. Jewell, W. M. Gregory, and R. H. Reznek, "In vivo measurement of spin lattice relaxation time (T1) of liver in healthy volunteers: the effects of age, sex and oral contraceptive usage," *The British Journal of Radiology*, vol. 61, pp. 34–37, Jan 1988. Cited on pp. 50, 111, 112, 134, and 136.

[112] K. Chow, J. A. Flewitt, J. D. Green, J. J. Pagano, M. G. Friedrich, and R. B. Thompson, "Saturation recovery single-shot acquisition (SASHA) for myocardial T1 mapping," *Magnetic Resonance in Medicine*, vol. 71, no. 6, pp. 2082–2095, 2014. Cited on pp. 50 and 98.

[113] P. Kellman, D. a. Herzka, A. E. Arai, and M. S. Hansen, "Influence of Off-resonance in myocardial T1-mapping using SSFP based MOLLI method," *Journal of Cardiovascular Magnetic Resonance*, vol. 15, p. 63, Jan 2013. Cited on p. 51.

[114] V. M. Ferreira, S. K. Piechnik, M. D. Robson, S. Neubauer, and T. D. Karamitsos, "Myocardial tissue characterization by magnetic resonance imaging: novel applications of T1 and T2 mapping.," *Journal of thoracic imaging*, vol. 29, pp. 147–54, May 2014. Cited on p. 52.

[115] M. Pavlides, R. Banerjee, J. Sellwood, C. Kelly, M. D. Robson, J. C. Booth, J. Collier, S. Neubauer, and E. Barnes, "Multiparametric magnetic resonance imaging predicts clinical outcomes in patients with chronic liver disease," *Journal of Hepatology2*, vol. 64, no. 2, pp. 308–315, 2016. Cited on pp. 52, 101, and 133.

[116] V. M. Ferreira, C. J. Holloway, S. K. Piechnik, T. D. Karamitsos, and S. Neubauer, "Is it really fat? Ask a T1-map," *European Heart Journal Cardiovascular Imaging*, vol. 14, p. 1060, Nov 2013. Cited on p. 52.

[117] V. Vassiliou, E. L. Heng, P. Sharma, E. Nyktari, C. Raphael, C. Chin, P. Drivas, G. Smith, K. Symmonds, G. Mathew, R. Wage, A. Ali, A. Greiser, F. Alpendurada, M. Dweck, D. Pennell, P. Gatehouse, and S. Prasad, "Reproducibility of T1 mapping 11-heart beat MOLLI Sequence," *Journal of Cardiovascular Magnetic Resonance*, vol. 17, no. Suppl 1, p. W26, 2015. Cited on p. 52.

[118] P. Bannas, H. Kramer, D. Hernando, R. Agni, A. M. Cunningham, R. Mandal, U. Motosugi, S. D. Sharma, A. Munoz del Rio, L. Fernandez, and S. B. Reeder, "Quantitative magnetic resonance imaging of hepatic steatosis: Validation in ex vivo human livers," *Hepatology*, vol. 62, pp. 1444–1455, Nov 2015. Cited on p. 53.

[119] A. Tang, J. Tan, M. Sun, G. Hamilton, M. Bydder, T. Wolfson, A. C. Gamst, M. Middleton, E. M. Brunt, R. Loomba, J. E. Lavine, J. B. Schwimmer, and C. B. Sirlin, "Nonalcoholic fatty liver disease: MR imaging of liver proton density fat fraction to assess hepatic steatosis," *Radiology*, vol. 267, pp. 422–31, May 2013. Cited on pp. 53 and 99.

[120] R. Rakow-Penner, B. Daniel, H. Yu, A. Sawyer-Glover, and G. H. Glover, "Relaxation times of breast tissue at 1.5T and 3T measured using IDEAL.," *Journal of Magnetic Resonance Imaging*, vol. 23, pp. 87–91, Jan 2006. Cited on p. 53.

[121] S. Thiesson, R. Thompson, and K. Chow, "Characterization of T1 bias from lipids in MOLLI and SASHA pulse sequences," *Journal of Cardiovascular Magnetic Resonance*, vol. 17, no. Suppl 1, p. W10, 2015. Cited on pp. 53, 67, 69, and 72.

[122] P. Kellman, W. P. Bandettini, C. Mancini, S. Hammer-Hansen, M. S. Hansen, and A. E. Arai, "Characterization of myocardial T1-mapping bias caused by intramyocardial fat in inversion recovery and saturation recovery techniques.," *Journal of Cardiovascular Magnetic Resonance*, vol. 17, p. 33, Jan 2015. Cited on pp. 53, 70, 72, and 108.

[123] C. de Meester de Ravenstein, C. Bouzin, S. Lazam, J. Boulif, M. Amzulescu, J. Melchior, A. Pasquet, D. Vancraeynest, A.-C. Pouleur, J.-L. J. Vanoverschelde, and B. L. Gerber, "Histological Validation of measurement of diffuse interstitial myocardial fibrosis by myocardial extravascular volume fraction from Modified Look-Locker imaging (MOLLI) T1 mapping at 3 T," *Journal of Cardiovascular Magnetic Resonance*, vol. 17, p. 48, Jan 2015. Cited on pp. 53, 59, and 63.

[124] B. Leporq, H. Ratiney, F. Pilleul, and O. Beuf, "Liver fat volume fraction quantification with fat and water T1 and T2* estimation and accounting for NMR multiple components in patients with chronic liver disease at 1.5 and 3.0 T," *European Radiology*, vol. 23, pp. 2175–86, Aug 2013. Cited on p. 53.

[125] G. Hamilton, M. S. Middleton, J. C. Hooker, W. M. Haufe, N. I. Forbang, M. A. Allison, R. Loomba, and C. B. Sirlin, "In vivo breath-hold 1H MRS simultaneous estimation of liver proton density fat fraction, and T1 and T2 of water and fat, with a multi-TR, multi-TE sequence," *Journal of Magnetic Resonance Imaging*, vol. 42, pp. 1538–1543, Jun 2015. Cited on pp. 53, 76, and 98.

[126] O. Bieri and K. Scheffler, "Fundamentals of balanced steady state free precession MRI.," *Journal of Magnetic Resonance Imaging*, vol. 38, pp. 2–11, Jul 2013. Cited on pp. 53 and 72.

[127] K. Scheffler and S. Lehnhardt, "Principles and applications of balanced SSFP techniques," *European Radiology*, vol. 13, pp. 2409–18, Nov 2003. Cited on p. 54.

[128] P. Kellman, J. R. Wilson, H. Xue, W. P. Bandettini, S. M. Shanbhag, K. M. Druey, M. Ugander, and A. E. Arai, "Extracellular volume fraction mapping in the myocardium, part 2: initial clinical experience.," *Journal of Cardiovascular Magnetic Resonance*, vol. 14, p. 64, Jan 2012. Cited on p. 56.

[129] "Magnetization, Relaxation, and the Bloch Equation," in *Magnetic Resonance Imaging: Physical Principles and Sequence Design* (R. W. Brown, Y.-C. N. Cheng, E. M. Haacke, M. R. Thompson, and R. Venkatesan, eds.), ch. 4, pp. 53–66, John Wiley & Sons, Ltd, 2nd ed., 2014. Cited on p. 56.

[130] C. M. J. de Bazelaire, G. D. Duhamel, N. M. Rofsky, and D. C. Alsop, "MR imaging relaxation times of abdominal and pelvic tissues measured in vivo at 3.0 T: preliminary results.," *Radiology*, vol. 230, pp. 652–9, Mar 2004. Cited on p. 58.

[131] G. J. Stanisz, E. E. Odrobina, J. Pun, M. Escaravage, S. J. Graham, M. J. Bronskill, and R. M. Henkelman, "T1, T2 relaxation and magnetization transfer in tissue at 3T," *Magnetic Resonance in Medicine*, vol. 54, pp. 507–512, Sep 2005. Cited on p. 58.

[132] B. Rial, M. D. Robson, S. Neubauer, and J. E. Schneider, "Rapid quantification of myocardial lipid content in humans using single breath-hold 1H MRS at 3 Tesla," *Magnetic Resonance in Medicine*, vol. 66, pp. 619–24, Sep 2011. Cited on pp. 62, 70, 80, and 103.

[133] A. Naressi, C. Couturier, J. M. Devos, M. Janssen, C. Mangeat, R. de Beer, and D. Graveron-Demilly, "Java-based graphical user interface for the MRUI quantitation package," *Magma: Magnetic Resonance Materials in Physics, Biology, and Medicine*, vol. 12, pp. 141–152, Jun 2001. Cited on p. 62.

[134] C.-Y. Liu, D. A. Bluemke, G. Gerstenblith, S. L. Zimmerman, J. Li, H. Zhu, S. Lai, and H. Lai, "Myocardial steatosis and its association with obesity and regional ventricular dysfunction: evaluated by magnetic resonance tagging and 1H spectroscopy in healthy African Americans.," *International Journal of Cardiology*, vol. 172, pp. 381–7, Mar 2014. Cited on p. 70.

[135] Y. Feng, T. He, J.-P. P. Carpenter, A. Jabbour, M. H. Alam, P. D. Gatehouse, A. Greiser, D. Messroghli, D. N. Firmin, and D. J. Pennell, "In vivo comparison of myocardial T1 with T2 and T2* in thalassaemia major," *Journal of Magnetic Resonance Imaging*, vol. 38, pp. 588–93, Sep 2013. Cited on p. 72.

[136] G. C. Farrell, "Non-alcoholic steatohepatitis: What is it, and why is it important in the Asia-Pacific region?," *Journal of Gastroenterology and Hepatology*, vol. 18, pp. 124–138, Feb 2003. Cited on p. 73.

[137] C. Hines, H. Yu, A. Shimakawa, C. McKenzie, V. Chebrolu, J. Brittain, and S. Reeder, "Validation of Fat Quantification with T2* Correction and Accurate Spectral Modeling in a Novel Fat-Water-Iron Phantom," *Proceedings 17th Scientific Meeting, International Society for Magnetic Resonance in Medicine*, vol. Honolulu, no. 2, p. 2707, 2009. Cited on p. 74.

[138] H. Yu, A. Shimakawa, C. A. McKenzie, E. Brodsky, J. H. Brittain, and S. B. Reeder, "Multiecho water-fat separation and simultaneous R2* estimation with multifrequency fat spectrum modeling," *Magnetic resonance in medicine*, vol. 60, pp. 1122–34, Nov 2008. Cited on p. 74.

[139] D. Hernando, P. Kellman, J. P. Haldar, and Z.-P. Liang, "Robust water/fat separation in the presence of large field inhomogeneities using a graph cut algorithm," *Magnetic Resonance in Medicine*, vol. 63, pp. NA–NA, Jan 2009. Cited on pp. 75 and 118.

[140] D. Hernando, J.-P. Kühn, B. Mensel, H. Völzke, R. Puls, N. Hosten, and S. B. Reeder, "R2* estimation using "in-phase" echoes in the presence of fat: The effects of complex spectrum of fat," *Journal of Magnetic Resonance Imaging*, vol. 37, pp. 717–726, Mar 2013. Cited on pp. 75, 79, and 118.

[141] M. A. Griswold, P. M. Jakob, R. M. Heidemann, M. Nittka, V. Jellus, J. Wang, B. Kiefer, and A. Haase, "Generalized Autocalibrating Partially Parallel Acquisitions (GRAPPA)," *Magnetic Resonance in Medicine*, vol. 47, pp. 1202–1210, Jun 2002. Cited on p. 75.

[142] L. Vanhamme, A. van den Boogaart, and S. Van Huffel, "Improved Method for Accurate and Efficient Quantification of MRS Data with Use of Prior Knowledge," *Journal of Magnetic Resonance*, vol. 129, no. 1, pp. 35–43, 1997. Cited on pp. 76 and 103.

[143] L. A. B. Purvis, W. T. Clarke, L. Biasiolli, L. Valkovič, M. D. Robson, and C. T. Rodgers, "OXSA: An open-source magnetic resonance spectroscopy analysis toolbox in MATLAB," *PLOS ONE*, vol. 12, p. e0185356, Sep 2017. Cited on pp. 76 and 103.

[144] T. G. St Pierre, P. R. Clark, W. Chua-anusorn, A. J. Fleming, G. P. Jeffrey, J. K. Olynyk, P. Pootrakul, E. Robins, and R. Lindeman, "Noninvasive measurement and imaging of liver iron concentrations using proton magnetic resonance.," *Blood*, vol. 105, pp. 855–61, Jan 2005. Cited on p. 80.

[145] G. Hamilton, M. S. Middleton, M. Bydder, T. Yokoo, J. B. Schwimmer, Y. Kono, H. M. Patton, J. E. Lavine, and C. B. Sirlin, "Effect of PRESS and STEAM sequences on magnetic resonance spectroscopic liver fat quantification," *Journal of Magnetic Resonance Imaging*, vol. 30, pp. 145–152, Jul 2009. Cited on p. 83.

[146] D. G. Altman and J. M. Bland, "Measurement in Medicine: The Analysis of Method Comparison Studies," *The Statistician*, vol. 32, p. 307, Sep 1983. Cited on p. 87.

[147] J. K. Reddy, M. S. Rao, and M. Sambasiva Rao, "Lipid metabolism and liver inflammation. II. Fatty liver disease and fatty acid oxidation," *American Journal of Physiology. Gastrointestinal and Liver Physiology*, vol. 290, pp. G852–8, May 2006. Cited on p. 96.

[148] M. Komu and A. Alanen, "Magnetization transfer in fatty and low-fat livers.," *Physiological Measurement*, vol. 15, pp. 243–50, Aug 1994. Cited on p. 97.

[149] S. Yu and K. Chou, "Integration of independent component analysis and neural networks for ECG beat classification," *Expert Systems with Applications*, vol. 34, pp. 2841–2846, May 2008. Cited on p. 98.

[150] G. Hamilton, A. N. Schlein, M. S. Middleton, C. A. Hooker, T. Wolfson, A. C. Gamst, R. Loomba, and C. B. Sirlin, "In vivo triglyceride composition of abdominal adipose tissue measured by 1H MRS at 3T," *Journal of Magnetic Resonance Imaging*, Aug 2016. Cited on p. 98.

[151] J. Lundbom, A. Hakkarainen, S. Söderlund, J. Westerbacka, N. Lundbom, and M.-R. Taskinen, "Long-TE 1H MRS suggests that liver fat is more saturated than subcutaneous and visceral fat," *NMR in Biomedicine*, vol. 24, pp. 238–245, Apr 2011. Cited on p. 98.

[152] J. J. Pagano, K. Chow, R. Yang, R. B. Thompson, null Reeder, null Chow, null Higgins, and null Wacker, "Fat-water separated myocardial T1 mapping with IDEAL-T1 saturation recovery gradient echo imaging," *Journal of Cardiovascular Magnetic Resonance*, vol. 16, no. Suppl 1, p. P65, 2014. Cited on p. 98.

[153] M. Nezafat, S. Roujol, J. Jang, T. Basha, and R. Botnar, "Eliminating the Impact of Myocardial Lipid Content on Myocardial T1 Mapping Using a Spectrally-Selective Inversion Pulse," in *Proc Intl Soc Mag Reson Med*, (Toronto), p. 2638, 2015. Cited on p. 98.

[154] S. Weingärtner, S. S. Roujol, M. Akçakaya, T. A. Basha, R. Nezafat, S. Weingartner, S. S. Roujol, M. Akcakaya, T. A. Basha, and R. Nezafat, "Free-breathing multislice native myocardial T1 mapping using the slice-interleaved T1 (STONE) sequence," *Magnetic Resonance in Medicine*, vol. 74, pp. 115–124, Jul 2014. Cited on p. 98.

[155] L. D. Garrison, C. Levick, M. Pavlides, T. Marjot, F. Mozes, L. Hodson, S. Neubauer, M. Robson, and C. T. Rodgers, "Water-Only Look-Locker Inversion recovery (WOLLI) T1 mapping," in *Proc. Intl. Soc. Mag. Reson. Med. 25*, p. 0435, 2017. Cited on p. 99.

[156] S. Larmour, K. Chow, P. Kellman, and R. B. Thompson, "Characterization of T1 bias in skeletal muscle from fat in MOLLI and SASHA pulse sequences: Quantitative fat-fraction imaging with T1 mapping," *Magnetic Resonance in Medicine*, vol. 77, no. 1, pp. 237–249, 2017. Cited on p. 108.

[157] A. Hall, C. Covelli, R. Manuguerra, T. V. Luong, E. Buzzetti, E. Tsochatzis, M. Pinzani, and A. P. Dhillon, "Transaminase abnormalities and adaptations of the liver lobule

manifest at specific cut-offs of steatosis," *Scientific Reports*, vol. 7, p. 40977, Jan 2017. Cited on p. 109.

[158] S. K. Piechnik, V. M. Ferreira, A. J. Lewandowski, N. A. B. Ntusi, R. Banerjee, C. Holloway, M. B. M. Hofman, D. M. Sado, V. Maestrini, S. K. White, M. Lazdam, T. Karamitsos, J. C. Moon, S. Neubauer, P. Leeson, and M. D. Robson, "Normal variation of magnetic resonance T1 relaxation times in the human population at 1.5 T using ShMOLLI," *Journal of Cardiovascular Magnetic Resonance*, vol. 15, p. 13, Jan 2013. Cited on pp. 111 and 119.

[159] J. C. Gore, M. S. Brown, C. T. Mizumoto, and I. M. Armitage, "Influence of glycogen on water proton relaxation times," *Magnetic Resonance in Medicine*, vol. 3, pp. 463–466, Jun 1986. Cited on pp. 112, 127, and 133.

[160] S. M. Meyers, R. Tam, J. S. Lee, S. H. Kolind, I. M. Vavasour, E. Mackie, Y. Zhao, C. Laule, B. Mädler, D. K. Li, A. L. MacKay, and A. L. Traboulsee, "Does hydration status affect MRI measures of brain volume or water content?," *Journal of Magnetic Resonance Imaging*, vol. 44, no. 2, pp. 296–304, 2016. Cited on p. 112.

[161] E. A. Newsholme and C. Start, "Regulation of Glycogen Metabolism," in *Regulation in Metabolism*, pp. 146–148, John Wiley & Sons, 1981. Cited on p. 112.

[162] E. M. Petäjä and H. Yki-Järvinen, "Definitions of Normal Liver Fat and the Association of Insulin Sensitivity with Acquired and Genetic NAFLD-A Systematic Review," *International journal of molecular sciences*, vol. 17, Apr 2016. Cited on p. 114.

[163] K. Scheffler, O. Heid, and J. Hennig, "Magnetization preparation during the steady state: Fat-saturated 3D TrueFISP," *Magnetic Resonance in Medicine*, vol. 45, pp. 1075–1080, Jun 2001. Cited on p. 115.

[164] D. Rothman, I. Magnusson, L. Katz, R. Shulman, and G. Shulman, "Quantitation of hepatic glycogenolysis and gluconeogenesis in fasting humans with 13C NMR," *Science*, vol. 254, pp. 573–576, Oct 1991. Cited on p. 116.

[165] G. A. Borg, "Psychophysical bases of perceived exertion.," *Medicine and science in sports and exercise*, vol. 14, no. 5, pp. 377–81, 1982. Cited on p. 116.

[166] H. Lei, F. Morgenthaler, T. Yue, and R. Gruetter, "Direct validation of in vivo localized 13C MRS measurements of brain glycogen," *Magnetic Resonance in Medicine*, vol. 57, pp. 243–248, Feb 2007. Cited on p. 117.

[167] S. M. Shirreffs and R. J. Maughan, "Urine osmolality and conductivity as indices of hydration status in athletes in the heat," *Medicine & Science in Sports & Exercise*, vol. 30, no. 11, pp. 1598–1602, 1998. Cited on p. 118.

[168] H. Kwon, J. Lee, K. Kim, Y. Kwak, and D. Kim, "Measurement of inferior vena cava and aorta with bedside ultrasound to assess degree of dehydration in children," *Critical Ultrasound Journal*, vol. 7, no. Suppl 1, p. A23, 2015. Cited on p. 118.

[169] K. Durajska, E. Januszkiewicz, Ł. Szmygel, and W. Kosiak, "Inferior vena cava/aorta diameter index in the assessment of the body fluid status - a comparative study of measurements performed by experienced and inexperienced examiners in a group of young adults," *Journal of ultrasonography*, vol. 14, pp. 273–9, Sep 2014. Cited on p. 118.

[170] H. Lu, C. Clingman, X. Golay, and P. C. van Zijl, "Determining the longitudinal relaxation time (T1) of blood at 3.0 Tesla," *Magnetic Resonance in Medicine*, vol. 52, pp. 679–682, Sep 2004. Cited on p. 119.

[171] D. L. Costill, L. Branam, D. Eddy, and W. Fink, "Alterations in red cell volume following exercise and dehydration," *Journal of applied physiology*, vol. 37, pp. 912–6, Dec 1974. Cited on p. 119.

[172] D. Muggli, M. Müller, C. Karlo, J. Fornaro, B. Marincek, and T. Frauenfelder, "A simple method to approximate liver size on cross-sectional images using living liver models," *Clinical Radiology*, vol. 64, pp. 682–689, Jul 2009. Cited on p. 119.

[173] E. M. MacKay and H. C. Bergman, "The Relation Between Glycogen and Water Storage in the Liver," *Journal of Biological Chemistry*, vol. 96, pp. 373–380, May 1932. Cited on p. 129.

[174] R. Pillon Barcelos, L. F. Freire Royes, J. Gonzalez-Gallego, and G. Bresciani, "Oxidative stress and inflammation: liver responses and adaptations to acute and regular exercise," *Free Radical Research*, vol. 51, pp. 222–236, Feb 2017. Cited on p. 129.

[175] J. Hicks, E. Wartchow, and G. Mierau, "Glycogen Storage Diseases: A Brief Review and Update on Clinical Features, Genetic Abnormalities, Pathologic Features, and Treatment," *Ultrastructural Pathology*, vol. 35, pp. 183–196, Oct 2011. Cited on p. 130.

[176] M. G. Bischof, M. Krssak, M. Krebs, E. Bernroider, H. Stingl, W. Waldhäusl, and M. Roden, "Effects of short-term improvement of insulin treatment and glycemia on hepatic glycogen metabolism in type 1 diabetes," *Diabetes*, vol. 50, pp. 392–8, Feb 2001. Cited on p. 130.

[177] K. F. Petersen, T. B. Price, and R. Bergeron, "Regulation of Net Hepatic Glycogenolysis and Gluconeogenesis during Exercise: Impact of Type 1 Diabetes," *The Journal of Clinical Endocrinology & Metabolism*, vol. 89, pp. 4656–4664, Sep 2004. Cited on p. 130.

[178] M. D. Robson and F. E. Mózes, "Correction method for magnetic resonance T1-mapping of visceral organs in the presence of elevated iron and elevated fat levels, and in the presence of off-resonance frequencies; Number: WO2018083504A1," 2018. Cited on p. 132.

[179] A. Asgharpour, S. C. Cazanave, T. Pacana, M. Seneshaw, R. Vincent, B. A. Banini, D. P. Kumar, K. Daita, H.-K. Min, F. Mirshahi, P. Bedossa, X. Sun, Y. Hoshida, S. V. Koduru, D. Contaifer, U. O. Warncke, D. S. Wijesinghe, and A. J. Sanyal, "A diet-induced animal model of non-alcoholic fatty liver disease and hepatocellular cancer," *Journal of Hepatology*, vol. 65, pp. 579–588, Sep 2016. Cited on p. 133.

[180] P. Mulder, W. Liang, P. Wielinga, L. Verschuren, K. Toet, L. M. Havekes, A. M. van den Hoek, and R. Kleemann, "Macrovesicular steatosis is associated with development of lobular inflammation and fibrosis in diet-induced non-alcoholic steatohepatitis (NASH)," *Inflammation and Cell Signaling*, vol. 2, Oct 2015. Cited on p. 133.

[181] R. Bataller and D. A. Brenner, "Liver fibrosis," *The Journal of Clinical Investigation*, vol. 115, pp. 209–18, Feb 2005. Cited on p. 133.

[182] J. Xu, M. D. Knutson, C. S. Carter, and C. Leeuwenburgh, "Iron Accumulation with Age, Oxidative Stress and Functional Decline," *PloS One*, vol. 3, p. e2865, Aug 2008. Cited on p. 133.

[183] A. Umpleby, F. Shojaee-Moradie, B. Fielding, X. Li, A. Marino, N. Alsini, C. Isherwood, N. Jackson, A. Ahmad, M. Stolinski, J. Lovegrove, S. Johnsen, A. Jeewaka R. Mendis, J. Wright, M. Wilinska, R. Hovorka, J. Bell, E. Thomas, G. Frost, and B. Griffin, "Impact of liver fat on the differential partitioning of hepatic triacylglycerol into VLDL subclasses on high and low sugar diets," *Clinical Science*, vol. 131, pp. 2561–2573, Nov 2017. Cited on p. 133.

[184] G. Della Pepa, C. Vetrani, G. Lombardi, L. Bozzetto, G. Annuzzi, and A. A. Rivellese, "Isocaloric Dietary Changes and Non-Alcoholic Fatty Liver Disease in High Cardiometabolic Risk Individuals.," *Nutrients*, vol. 9, Sep 2017. Cited on p. 133.

[185] C. J. Green and L. Hodson, "The influence of dietary fat on liver fat accumulation.," *Nutrients*, vol. 6, pp. 5018–33, Nov 2014. Cited on p. 133.

[186] M. Dezortova, T. Blahova, M. Drobny, P. Sedivy, J. Kovar, and M. Hajek, "Dietary intervention can induce changes in hepatic fat content during the day detectable by MR spectroscopy," in *Proc. Intl. Soc. Magn. Res. Med 26*, (Paris), p. 608, 2018. Cited on p. 133.

[187] M. Macauley, F. E. Smith, P. E. Thelwall, K. G. Hollingsworth, and R. Taylor, "Diurnal variation in skeletal muscle and liver glycogen in humans with normal health and Type 2 diabetes," *Clinical Science*, vol. 128, pp. 707–713, May 2015. Cited on p. 134.

[188] A. Mojtahed, C. J. Kelly, A. H. Herlihy, S. Kin, H. R. Wilman, A. McKay, M. Kelly, M. Milanesi, S. Neubauer, E. L. Thomas, J. D. Bell, R. Banerjee, and M. Harisinghani, "Reference range of liver corrected T1 values in a population at low risk for fatty liver disease—a UK Biobank sub-study, with an appendix of interesting cases," *Abdominal Radiology*, pp. 1–13, Jul 2018. Cited on p. 134.

[189] G. K. Michalopoulos and M. C. DeFrances, "Liver regeneration," *Science (New York, N.Y.)*, vol. 276, pp. 60–6, Apr 1997. Cited on p. 136.

[190] N. Fausto, J. S. Campbell, and K. J. Riehle, "Liver regeneration," *Hepatology*, vol. 43, pp. S45–S53, Feb 2006. Cited on p. 136.

[191] J. H. Henriksen and S. Moller, "Liver cirrhosis and arterial hypertension," *World Journal of Gastroenterology*, vol. 12, pp. 678–85, Feb 2006. Cited on p. 136.

[192] F. Rodriguez-Moreno, E. Gonzalez-Reimers, F. Santolaria-Fernandez, L. Galindo-Martin, O. Hernandez-Torres, N. Batista-Lopez, and M. Molina-Perez, "Zinc, Copper, Manganese, and Iron in Chronic Alcoholic Liver Disease," *Alcohol*, vol. 14, no. 1, pp. 394–398, 1997. Cited on p. 136.

[193] N. Karabulut and N. Elmas, "Contrast agents used in MR imaging of the liver," *Abdominal Imaging*, vol. 12, pp. 22–30, 2006. Cited on p. 136.

[194] R. B. Thompson, K. Chow, and J. Grenier, "Simultaneous Proton Density Fat Fraction Imaging and Water T1-Mapping with Low B1+ Sensitivity (PDFF-T1)," in *Proc. Intl. Soc. Mag. Reson. Med. 26*, (Paris), p. 35, 2018. Cited on p. 137.